The TEA - CO_2 Laser as a means of Generating Ultrasound in Solids

being a thesis submitted for the degree of Doctor of Philosophy at the University of Warwick

by

Gregory Stuart Taylor B.Sc. (Manchester)

Department of Physics
University of Warwick
December 1990

Contents

Figure Captions

Acknowledgement

None of this work would have been possible without the combined funding of the Science and Engineering Research Council and the United Kingdom Atomic Energy Authority (Risley). As such I am particularly grateful to them for allowing me to conduct this research.

I am very grateful to my supervisor Professor Stuart Palmer for his enthusiasm, guidance and friendship over the past three years. Together with Stuart, Chris Edwards and David Hutchins have always been more than willing to advise, help and give the occasional howl of laughter.

One of the most enjoyable aspects of my time at Warwick has been the friendly and relaxed atmosphere within the department. As such I would like to thank, in no particular order, Stephen, Roger, Don, Andrew, Adrian and John for their friendship, help and ability to bring one down to earth with a bump.

At this the end of my time in university I would like to thank my family for their support, not just over the period of this work, but over the last sixteen years of my full time education. Without their love and guidance I would not have been able to write this acknowledgement.

Lastly, but by no means least, I would like to thank Kay for her continued love, support and ability to put up with so much "thesis talk" over the past five months.

Declaration

The work contained in this thesis is my own except where otherwise stated, being based in the Physics Department at the University of Warwick between October 1987 and December 1990. No part of this thesis has been previously submitted to this or any other academic institution for admission to a higher degree. Some of this work has already appeared in publications which are listed at the end of the thesis.

Abstract

The aim of this thesis is to characterise the interaction between pulsed , high power , 10.6 μm radiation and solids . The work is considered both in the general context of laser generation of ultrasound and specifically to gain a deeper understanding of the interaction between a laser supported plasma and a solid.

The predominant experimental tools used are the homodyne Michelson interferometer and a range of electromagnetic acoustic transducers . To complement the ultrasonic data , various plasma inspection techniques , such as high speed , streak camera photography and reflection photometry , have been used to correlate the plasma properties with those of the ultrasonic transients.

The work involving the characterisation of a laser supported plasma with a solid , which is based on previous experimental and theoretical analysis , gives an increased understanding of the plasma's ultrasonic generation mechanism. The ability to record the entire plasma - sample interaction , time history yields information of the internal dynamics of the plasma growth and shock wave generation.

The interaction of the radiation with a solid is characterised in both the plasma breakdown and non-breakdown regimes by a wide ultrasonic source . The variation in source diameter enables the transition from a point to a near planar ultrasonic source to be studied . The resultant ultrasonic modifications are examined in terms of the wave structure and the directivity pattern . The wave structure is analysed in terms of existing wide source , bulk wave theories and extended to consider the effects on surface and Lamb waves . The directivity patterns of the longitudinal and shear waves are analysed in terms of top-hat and non-uniform source profiles , giving additional information into the radiation - solid interaction . The wide , one dimensional source analysis is continued to a two dimensional , extended ultrasonic source , generated on non-metals by the optical penetration of radiation within the target .

The generation of ultrasound in both metals and non-metals , using the CO_2 laser , is shown to be an efficient process and may be employed almost totally non-destructively . Such a laser may therefore be used effectively on a greatly enhanced range of materials than those tested to-date via laser generation , resulting in the increased suitability of the laser technique within the field of Non Destructive Testing.

Chapter 1

Introduction

Laser generation of ultrasound as an addition to existing means of ultrasonic generation , is now well over decade old . During this time a number of lasers , in the wavelength range ~ 0.3 - 1 μm , have been used to generate ultrasound in an increasingly large range of solids , usually metals . The interaction process , as described in detail in chapter 3 , has been keenly studied in two main areas . Firstly the laser's ultrasonic source may be considered as close to an ideal Heaviside time dependent source function , either normally or tangentially applied to the sample surface . As such the laser source has been used to verify fundamental ultrasonic generation processes and has become one of the leading experimental tools in the extension of acoustic models to non-ideal source functions .

Secondly laser generated ultrasound has been used in Non-destructive testing (NDT) to examine materials for defects [1] and to assess a range of inherent properties , such as anisotropy [2], residual stress [3] and internal structural changes [4] . The broadband , high frequency nature of the transients enables highly accurate timing measurements to be made yielding precise determination of Young's modulus or Lame constants [5]. The short pulses associated with the longitudinal , shear and Rayleigh waves give high resolution when inspecting layered composite materials [6] or in resolving internal material structure , such as defects . They also form a sound basis for the application of imaging techniques such as Synthetic Aperture Focusing [7] or other tomographic methods .

In both areas of study the main advantage offered by the laser is that it is a non-contacting means of ultrasonic generation and thus the sample under inspection is unperturbed by the presence of a generating transducer which will load the sample surface . This remote nature gives the additional benefit

that the sample under inspection may be moving , in the case of on-line monitoring , hot , as for the inspection of newly rolled steel , radioactive or have a highly complex geometry .

Despite the many advantages offered by lasers as ultrasonic sources there are drawbacks to the technique . The generation process is relatively inefficient , down by at least an order of magnitude compared to piezoelectric transducers. The creation of a surface damage pit due to the evaporation of the irradiated material when working at high power densities renders the technique not truly non-destructive . Increasing the absorbed laser energy to enhance the generation efficiency is also responsible for increasing the surface damage and as such the simultaneous solution of these problems may not be achieved using this type of absorption process .

It is the requirements for both enhanced laser generation and reduced surface damage which are the motivating factors for this study . The CO_2 laser , operating at 10.6 μm , has a very differing interaction with metals to those radiation wavelengths traditionally used for ultrasonic generation . The transmission coefficient is such that less than two percent of the incident radiation is absorbed at the material surface , an amount which as shown later produces only a weak surface heating and generates no surface damage . At first sight this laser type seems a less than obvious choice for the production of an intense source of ultrasound , however the generation of a gas plasma above the sample giving rise to an intense shock wave is the means by which ultrasonic generation occurs .

The aim of this work is therefore to study plasma formation as an ultrasonic source in terms of its efficiency , flexibility and source function . This characterisation is extended to include the interaction of 10.6μm radiation with non-metals to enhance the potential of lasers within the field of NDT by greatly increasing the range of testable materials . The work presented in this thesis is meant to complement the fundamental work carried out on traditional

laser sources such that the two forms of generation may be directly compared and contrasted .

Chapter 2 gives a basic review and introduction to laser generation of ultrasound in terms of the radiation - metal interaction and the regimes into which this interaction falls . The essential requirement of having suitable detectors to complement the broadband , non-contacting nature of the laser source is described in terms of the optical and electromagnetic methods of detection used predominantly in this work .

Chapter 3 describes the interaction of 10.6μm radiation with metals in terms of the physical processes required to generate a plasma within the surrounding gas and the formation and subsequent motion of the resulting shock wave . Chapter 4 provides an understanding of the plasma as an ultrasonic source examined by using both epicentral and surface waves . Variation in the plasma source as a function of incident energy , source size and laser pulse profile are analysed to characterise the source and determine the laser's ultrasonic generation efficiency . As with the early work concerning Nd:YAG laser generation , the characteristics of the target are explored to ascertain how they effect the resultant acoustic waveform . Indications that the plasma produces a non-point-like source are examined in chapter 5 . This chapter discusses the effect of a wide ultrasonic source in terms of the form of the ultrasonic transients and more informatively the directivity patterns produced by the plasma . This work includes the analysis of a non-point-like source in terms of a simple top-hat function and a more complex but physically acceptable non-uniform source distribution which approximates closely to the spatial profile of the breakdown source .

Chapter 6 extends the wide source analysis to the non-breakdown source types generated by 10.6μm radiation :- the thermoelastic and surface modified , evaporative interactions which are traditionally used in laser generation . The evaporation source is , to a close approximation , an extension of the wide

plasma source while the thermoelastic interaction leads to the presence of acoustically dead source regions , which have a significant effect on the form of the ultrasound generated .

An extension of the one-dimensional sources discussed in the previous chapters is presented in chapter 7 , which involves the modelling of an optically penetrating , extended thermoelastic source . The study centres on the generation of ultrasound in non-metals as described by the interaction with Perspex and glass , two materials with differing optical and acoustic properties . The form of the source as a function of incident power density is considered within the regimes of the thermoelastic , evaporative and breakdown interactions . This work is compared with previous attempts to inspect non-metals using laser techniques .

Chapter 8 extends the work initiated in chapter 7 in applying the CO_2 laser to the inspection of thin polymer films . The bulk of the chapter is dedicated to the development and characterisation of two types of laser probe detector designed in an attempt to enhance the resolution and sensitivity of the traditional knife edge optical sensor . The combination of CO_2 generation and optical probe detection is subsequently employed to examine thin , transparent , polymer films via the analysis of Lamb waves .

To conclude , chapter 9 , presents a summary of the work undertaken in the thesis , in terms of the main characteristics of the CO_2 laser source , the use of ultrasonics as a technique in observing the plasma - solid interaction and the differences between CO_2 and Nd:YAG ultrasonic generation . Finally a discussion of future work that could be conducted in the area of CO_2 laser generation of ultrasound and other topics raised in this thesis is presented .

References Chapter 1

[1]J.A. Cooper , R.A. Crasbie , R.J. Dewhurst & S.B. Palmer , pp207-212 Proc. Ult. Int. , Butterworths , London (1985)
[2]P.P. Delsanto , R.B. Mignogna & A.V. clark , J.A.S.A. vol 87 no 1 pp215-224 (1990)
[3]D.R. Allen & C.M. Sayers , Ultrasonics , vol 22 pp179-187 (1984)
[4]R.D. Greenough , R.J. Dewhurst & C. Edwards , J. Appl. Phys. , vol 62 pp4728-4731 (1987)
[5]L. Bresse chapter 4 M.Sc Thesis , Queen's University , Canada (1988)
[6]W.T. Thompson , J. Appl. Phys. , vol21 pp1215-1222 (1950)
[7]R.S.Sharpe , "Research Techniques in Non-destructive Evaluation " , vol6 chapter 2 (Ed. R.S. Sharpe , Academic Press , 1982)

Chapter 2

Non-Contacting Generation and Detection

2.1 Introduction

It is not the purpose or aim of this introduction to examine fully the details of laser generated ultrasound . Firstly this task has been carried out else-where [1,2] in far greater depth and rigour than is possible within the scope of this thesis . Secondly the usage and characteristics of the TEA- CO_2 laser ultrasonic source will be compared with the corresponding features of Nd:YAG generation throughout this thesis . The Nd:YAG will be cited as the typical laser ultrasonic source since it has been the most widely used and reported in the literature . This review of laser generation hopefully gives a brief insight into the characteristics of generation via the absorption of radiation at a metal surface , in terms of the generation efficiency , mechanism and form of the generated transients . The essential point to note is that the laser offers a means of producing ultrasound with near ideal source functions for the study of elastic transients which may be used to verify theoretical predictions of surface generated normal and tangential forces with either Heaviside or impulsive time dependencies .

2.2 Characteristics of Laser Generation

Typically three laser types have been employed to generate ultrasound , Nd:YAG at 1.06μm , Ruby at 694nm [3] and Nitrogen at 337nm [4] while excimer lasers are being increasingly used . All four laser types produce ultrasound via the underlying mechanism of radiation absorption at the target surface followed by phonon heating producing expansion or evaporation which generates a stress in the irradiated material giving rise to the generation of ultrasonic transients .

Laser radiation incident on a metal surface will be partly absorbed into the material the remainder being reflected . The transmission coefficient , T , for metals , for incident radiation within the infrared spectral range is given as

$$T = 2\sqrt{\frac{2\omega\varepsilon_o}{\sigma}} \qquad 2.1$$

where σ is the electrical conductivity ,ε_o the permitivity of free space and ω the photon frequency .This gives a transmission coefficient for a clean , pure aluminium surface of ~7% , a value which is increased to a figure of up to ~ 20% if the material has impurities , such as oxides on the surface . Typical laser energies used range from 10mJ up to 300mJ , thus giving absorbed energies lower by an order of magnitude . To a first approximation the energy is absorbed in the electromagnetic skin depth of the material , however subsequent diffusion of the generated heat will result in the time evolution of the ultrasonic source over timescales of the laser pulse duration . The temperature rise within the material due to the absorption of radiation may be determined by solution of the differential heat flow equation , being stated as

$$\nabla^2\theta(x,y,z,t) - \frac{1}{\kappa}\frac{\partial\theta(x,y,z,t)}{\partial t} = -\frac{A(x,y,z,t)}{K} \qquad 2.2$$

where A(x,y,z,t) is the heat production per unit volume per unit time , within the material , θ(x,y,z,t) the temperature rise , K the thermal conductivity and κ the thermal diffusivity . The solution of eq 2.2 has the boundary conditions of $\theta(x,y,z,0) = 0$ and $\theta(x,y,z,t) \rightarrow 0$ as $z \rightarrow \infty$ [5] . As the width of the laser source is several orders of magnitude larger than the thermal skin depth the heat flow problem may be treated as being one dimensional over timescales of the laser pulse . Consideration of eq.2.2 for a Gaussian beam profile of radius 0.3mm and pulse energy of 10mJ shows a rapid surface temperature rise leading initially to a temperature distribution which is highly peaked at the material surface . The maximum temperature of the order 300 C , decays to it's half its

value within 1μm . Over timescales of ~100ns the temperature distribution becomes almost uniform to depths of ~5μm . Dependant on the laser power density the ultrasonic generation falls into two distinct limiting cases . At low power densities , < $5 \cdot 10^7$ Wcm^{-2} , where no change of phase is produced a thermoelastic interaction results , while for power densities above this value evaporation of the material results in a force being generated normally into the sample surface .

2.2.1 The Thermoelastic Regime

The rapid heating of the irradiated region produces expansion of this volume against the cold surrounding metal . As the sample surface is free to move the stress directed normally into the sample is effectively relieved by an outward expansion of the material , this is not however the case for the symmetric radial expansion produced in the plane of the sample surface . The resultant ultrasonic waveform has been determined by Cooper [6] , Sinclair [7] and Rose [8] , all of whom obtained the same basic on-epicentre displacement waveform which could be adequately described by a point source . This displacement is characterised by an initial inwardly displacing step , longitudinal arrival after which the surface continues to displace inwards until the shear arrival seen as a positive displacing step . Experimental observation of this waveform [2] , which is produced with an efficiency of 0.028 nm/mJ , shows the longitudinal wave to have a small positive displacing precursor . Doyle [9] and later Thompson [10] modelled this arrival as originating from heat diffusion within the sample . Such heat diffusion generates a time evolving ultrasonic source resulting in buried source components which arrival slightly before the surface generated wave components .

The ultrasonic directivity pattern produced under the action of the thermoelastic source [11] sees both the longitudinal and shear waves peaked in magnitude off-epicentre between 30°-60° . The longitudinal wave has a broad lobe of energy centred within the above range , while the shear wave is sharply peaked at 30° , with a second lower energy lobe peaked at ~70° , both directivities having zero on-epicentre amplitude . The characteristic displacement wave discussed above is not included in the longitudinal directivity as it has an associated square law decay as opposed to the simple inverse decay term included in the directivity pattern .

2.2.2 The Ablative Regime

An increase in the power density beyond $\sim 10^8$ Wcm^{-2} increases the surface temperature sufficiently to produce a change of phase , the rapid evaporation of surface material associated with the creation of a vapour , generates a force directed normally into the sample . The source which may again be treated as a point , produces an epicentral displacement which has been characterised by Knopoff [12] , to be discussed in detail in chapter 3 . This displacement , which has opposite polarity to that produced by the thermoelastic source is characterised by an initial positive displacing step after which the surface continues to displace outward ,the shear arrival being marked simply by a change in gradient . The normal force results in the ultrasonic longitudinal directivity being centred about the normal to the surface , being a maximum on-epicentre and falling steadily to zero at 90° , while the shear directivity is sharply peaked at ~40° off-epicentre [11]

As the ablative process relies initially on heating , a component of thermoelastic stress is always present in the ablative source . This modifies the resultant ultrasonic displacement obtained which may be treated as a linear

superposition , with the correct weighting function , of the ablative and thermoelastic waveforms [13]

2.2.2 Surface Modified Sources

The application of a thin liquid layer , such as water or grease , on the target surface provides an easily evaporated medium which produces a recoil force into the target in a similar fashion to the ablation of material using high radiation power densities . [14] . As the relative transition temperatures of such overlying liquids are considerably lower than those for metals , the resultant vapour is highly energetic producing a large force at the sample surface . The low transition temperature results in an extremely rapid temporal source profile for the interaction which , to a first approximation , may be treated as being a delta function . The ease of evaporation is also reflected in the large surface displacements achieved using such layers , being in the range of ~10 - 30 nm depending on the incident power density . The normal force produces a directivity similar to that generated by the ablative source .

In all cases the ultrasound produced is broadband , with the frequency spectrum being the fourier transform of the temporal profile of the laser pulses . This gives , for a typical 10ns risetime laser pulse , a maximum frequency component of ~25MHz . The frequency content of laser generated transients has recently been shown to be laser pulse limited and not material limited up to frequencies of ~1 THz , as measured using a 0.3 ps F.W.H.M. laser pulse [15]

To complement this generation technique and to observe directly the motion of the free sample surface , non-contacting , broadband ultrasonic transdusers are required . The coupling of PZT type transducers to the sample damps its motion and gives rise to distortions . To obtain the actual surface

motion , deconvolution of the PZT output with the detector response and the surface damping function is required , a task which is prone to large errors . Therefore a non-contacting , broadband , high resolution transducer is the ideal means by which direct measurement of the ultrasonic transients may be made . There are at present several non-contacting transducers which rely mainly on electromagnetic and optical techniques . The work in this study relies on three main transducer types . The homodyne Michelson interferometer and the electromagnetic acoustic transducer , both being discussed in the next section , and thirdly the "laser probe" optical sensor is discussed fully in chapter 8 .

2.3 Electromagnetic Acoustic Transducers

Electromagnetic acoustic transducers (EMATs) are devices which generate and detect ultrasound via a Lorentz interaction on non-magnetic materials or magnetostrictively on magnetic materials [16] and which may be made to be sensitive to both in or out-of-plane motion . As generators of ultrasound they are to-date relatively inefficient and have previously required large electric power supplies as the generation process relies upon the creation of lattice vibrations via its interaction with oscillating electrons . In this work EMATs are employed simply as detectors of ultrasound .

Kawashima [17] gives an excellent basis for the description of the process by which EMATs detect ultrasound on non-magnetic materials . Consider a sinusoidally time varying acoustic wave travelling towards the surface of a metal , as shown in Fig 2.1 , expressed as

$$S(z) = So \exp -jk_e z \cdot \exp j\omega t \qquad 2.3$$

where z is the distance into the sample , k_e the ultrasonic wavenumber and So the peak amplitude . This wave combines with that reflected off the sample

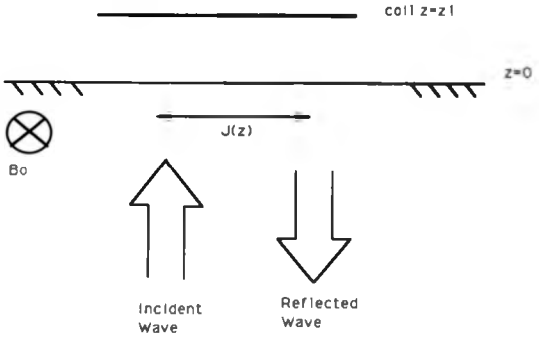

Fig 2.1 The relative positions of the ultrasonic waves, static field and coil, for out-of-plane motion sensing. [after Kawashima]

surface and therefore the lattice is forced into oscillation due to the sum of the two wave components as

$$\xi(z) = So\,(\exp -jk_c z + \exp +jk_c z)\exp j\omega t \qquad 2.4$$

If a static magnetic field , Bo , is present within the metal with its field orientated perpendicular to the lattice motion , then an eddy current , J(z) , is induced through the interaction of Bo and $\xi(z)$. This is expressed by Kawashima as

$$J(z) = \sigma \frac{\partial \xi(z)}{\partial t} Bo \qquad 2.5$$

where σ is the metal conductivity , which on substitution of eq. 2.4 gives the eddy current in terms of the acoustic wave and the magnetic potential only . The presence of an oscillating eddy current produces a quasi-static vector potential A' within the metal which is related to J(z) by the differential form of Faraday's Law [18]

$$\frac{1}{\mu}\nabla^2 A' - \sigma \frac{\partial A'}{\partial t} = -J(z) \qquad 2.6$$

where μ is the relative permeability of the metal . Solution of eq. 2.6 and application of the appropriate boundary conditions gives the vector potential in air in the direction perpendicular to the metal surface at a height z_1 above the sample , $A_x(z_1)$ as

$$A_x(z_1) = 2SoBo \frac{1}{1 - \frac{1}{2}jk_c^2\delta^2} \qquad 2.7$$

where δ is the electromagnetic skin depth . The vector potential is a sum of contributions from all components of J(z) within the metal . However as the amplitude of an eddy current falls by e^{-1} within a distance δ of its origin then the potential will be strongly weighted by contributions from the surface of the conductor . A further point of consideration is that eq.2.7 has no z dependence

on the vector potential , which originates from the assumption of a one dimensional ultrasonic wave . The induced field strength , E , is related to the vector potential by

$$E = \int_s j\omega A ds \qquad 2.8$$

and induces a voltage , V , in a detection coil of area W and N turns per metre placed above the sample . Eqs. 2.8 and 2.7 enable V to be determined for the sinusoidally time varying case . An approximation may be made from the continuous case to the pulsed case , to give the induced pulsed voltage , Vp(t) , as

$$Vp(t) = - NWBo \frac{\partial}{\partial t} (2\, S_p(t,0)) \qquad 2.9$$

where Sp(t,0) is the amplitude of the ultrasonic wave at the sample surface . As there will be a finite frequency content within the ultrasonic pulse the EMAT will detect to a finite depth , however this is small compared to the wavelength of the ultrasonic pulse . The form of eq.2.9 gives the voltage to be proportional to the time derivative of the surface motion , making it a velocity sensor .

The detection mechaniam on magnetic materials is different to the Lorentz force interaction described above . The motion of a continuously varying or pulsed strain field within a magnetic material produces a rotation of the magnetostatic direction within the individual domains of the material [19] . This rotation changes the external magnetic field which is sensed by the EMAT coil . The magnetic field varies linearly with the strain variations of the ultrasonic field and thus the output of the EMAT is proportional to the surface displacement . The Lorentz force interaction is still present in magnetic materials and thus the EMAT senses both the sources of vector potential fluctuations , although particularly for low field strengths the magnetostrictive component is dominant . If the external magnetic field is sufficiently high it is possible to rotate the magnetic domains such that they are held static and are

unable to rotate under the action of a strain field and therefore the EMAT will only detect the Lorentz force interaction [20].

In both the Lorentz and magnetostrictive interactions the EMAT has the ability to sense either in or out-of-plane motion dependent on the relative orientations of the sensing coil, magnetic field and lattice motion . Fig 2.2 a,b shows the two most common designs of EMAT used in this work . The top diagram shows the longitudinal motion sensitive device , which has a magnetic field parallel to the surface of the sample , thus the relative orientations of field , coil and particle motion obey the Maxwell right hand rule . The magnetic field is brought to the sample via mild steel flux guides . The bottom diagram shows the typical in-plane motion sensitive EMAT , which has the relative orientations of the field and lattice motion reversed . In both designs the static field is provided by permanent NdFeB magnets , which have a Hall probe measured flux of 0.36T , while the coil is wound from 46 gauge insulated copper wire to ensure a large number of coil turns . Multiple coil layers will enhance the sensitivity of the device providad the coil thickness does not result in a significant stand-off of the magnetic field .

2.3.1 Stand Off

The EMAT , by the nature of its interaction , is a non-contacting detector .The stand-off from the surface is however limited by the field strength variation for increasing magnet - sample separation and the geometric source effects of the vector potential not accounted for by Kawashima's model . The magnetic field variations for both EMAT types may be calculated using standard electromagnetic theory . In the case of the shear sensitive device the field variation , Bz(z) , at a distance z from the magnet may be expressed as

$$Bz = Bo\left(1 - \frac{z/a}{(1 + z^2/a^2)^{1/2}}\right) \qquad 2.10$$

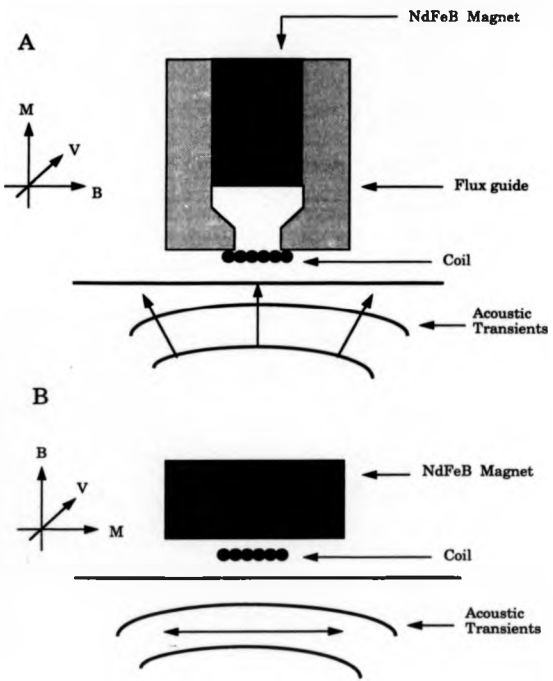

Fig 2.2 a& b Out-of-plane and in-plane sensitive EMAT designs respectively .

which is obtained [21] by considering the source strength of an annular field element and integrating across the magnet radius , a . The decrease in $B_z(z)$ as a function of increasing stand off , shown in Fig 2.3a , shows the field to decay almost linearly with increasing stand-off , falling to half amplitude at a separation of z~2.7mm . The measured stand off for an in-plane EMAT , shown in Fig 2.3b measured using a standard Nd:YAG laser source , shows the amplitude variations to be initially constant for low stand-off indicating an interesting geometrical effect of the vector potential originating from the none one dimensional ultrasonic source . The stand off half height occurs at 0.85mm a value well below that predicted from the magnetic field variations alone .

The variation of magnetic field , $B_z(z)$, in the case of the out-of-plane EMAT has a more complicated geometrical dependance [22] expressed as

$$Bx = \frac{Bg}{\pi}\left(\tan^{-1}\frac{(z+b)\,c}{a(a^2+(z+b)^2+c^2)^{1/2}} - \tan^{-1}\frac{z\,c}{a(a^2+z^2+c^2)^{1/2}}\right) \quad 2.11$$

where a is the half pole piece separation , c the half pole length , b the pole height and Bx is the magnetic field in the x-direction for increasing pole face stand-off , shown in Fig 2.4a . The field decreases rapidly for small stand-off , falling to half amplitude level at a distance of 0.7mm away from the pole face , the measured stand off , shown in Fig 2.4b , falls to the equivalent level in a distance of 0.6mm . The comparative agreement between the longitudinal sensitivity variations compared to the inconsistencies between theory and experiment for the shear device's may have its origins in the geometric nature of the vector potential produced by the ultrasonic wave and thus the theoretical predictions of Kawashima must be treated cautiously . Fig 2.4b shows the pole centre field ,Bg , to be ~0.9T a value larger than the to magnet's pole value of 0.36T , due to the presence of the flux guides . Calculation of the magnetic field in the gap may be made if one firstly assumes conservation of magnetic flux

$$BmAm = BgAg \quad 2.12$$

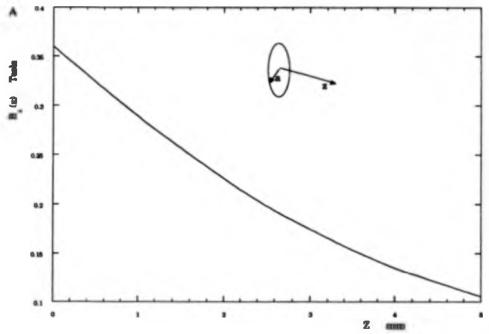

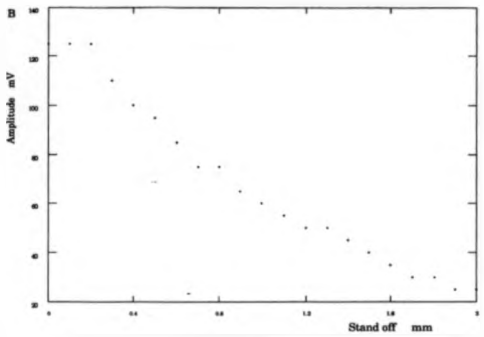

Fig 2.3 a : Calculated magnetic field strength and
b : Measured Shear EMAT sensitivity variation
as a function of stand off .

where subscript m = magnet and g = gap and A is the respective area . Bm is the recoiled value of the magnetic field due to the presence of the flux guides being expressed as

$$Bm = Bp + \mu_0\mu_r Hm \qquad 2.13$$

where Bp is the total recoiled pole strength =1.2T and μ_r is the recoil permeability for NdFeB magnets = 1.1 resulting in almost complete recoil of the magnet . A second condition for the field calculation is that the magnetomotive force in the circuit is zero , expressed as

$$HmLm + H_{fg}L_{fg} + HgLg = 0 \qquad 2.15$$

where L is the circuit element length and subscript fg corresponds to the flux guide part of the circuit , which may be neglected as being small . Eqs 2.13 , 2.14 & 2.15 enable the field in the gap , Bg , to be calculated in terms of of the magnet and gap dimensions by the relationship

$$Bg = \frac{1.2\,k\,Lm}{\left(1.2\frac{LmAg}{Am} + 1.1Lg\right)} \qquad 2.16$$

where k has been introduced as a loss term characteristic of the design and depends upon the relative magnet , flux guide and pole gap positioning [21] . Pole dimensions of Lg=2a=1mm , b=1mm and c=12mm give a pole strength of 1.6T assuming no losses , however a figure of ~1T is more realistic . For both designs of EMAT the magnetic field may be increased when detecting on magnetic materials due to enhanced recoil effects and the presence of magnetic images induced in the sample surface . The strength of the images are given by $(1-\mu)/(1+\mu)$, where μ is the relative permeability of the ferromagnet , large μ resulting in the near doubling of the magnet pole strength . A second effect which is inherent in both detector designs is the presence of fringing fields which leads to the EMAT detecting both in and out-of-plane motion

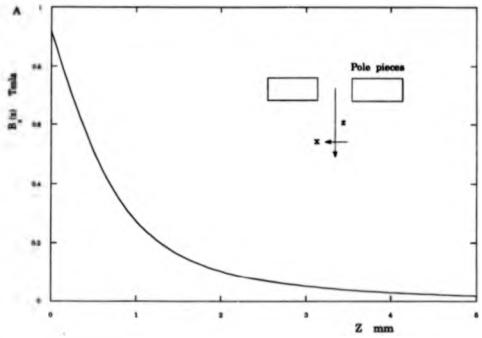

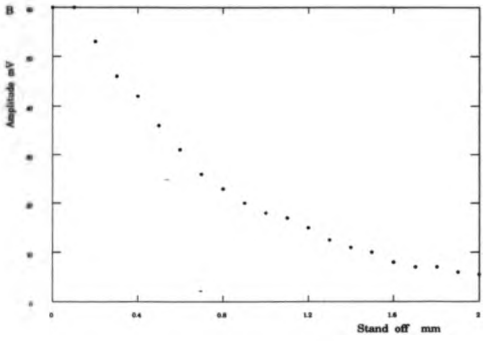

Fig 2.4 a : Calculated magnetic field strength and
b : Measured longitudinal EMAT sensitivity variation
as a function of stand off .

simultaneously [23] , leading to waveform complications and even to resolvable secondary signals being observed .

2.3.2 Bandwidth Considerations

The bandwidth of EMAT sensors is limited by two main contributions . Firstly the area of the sensing coil and secondly the bandwidth of the pre-amplifiers used as part of the detection system . The ultimate bandwidth of the EMAT is limited by the time duration of the ultrasonic arrivals across the coil , an effect which is most noticeable in the detection of Rayleigh waves . For a coil width of 1mm the upper Rayleigh frequency content is limited by this constraint to ~3MHz . Further consideration of this problem for bulk waves is made in chapter 4 . The amplifiers used here are based on Plessey SL560C and Frerranti ZN459 high speed chips and are specially designed to work with the low impedances of the EMAT coil , which have a resistance of between 5-15 Ω . The non-standard impedance often requires the amplifiers to be tailored to specific EMATs to ensure stability . Fig 2.5 shows a series of gain-frequency amplifier profiles for four typical pre-amplifiers used in this work . The curves clearly show the broadband nature of the devices , the frequency content extending well in excess of the upper ultrasonic frequency limit used here .

2.4 The Modified Michelson Interferometer

A conventional Michelson interferometer is an optical device for sensing relative changes in optical path length between two objects . In such a device the radiation from a light source is split into two perpendicular rays or "arms", which are reflected off a reference mirror and a "sample" respectively . The two rays are brought back together and constructive and destructive

Fig 2.5 a

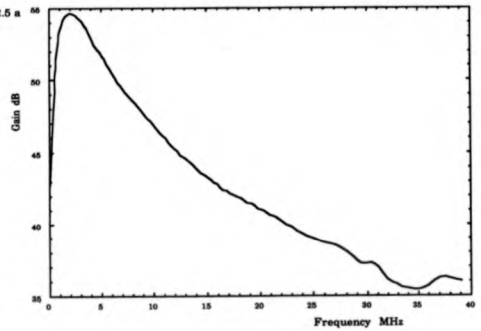

Fig 2.5 b

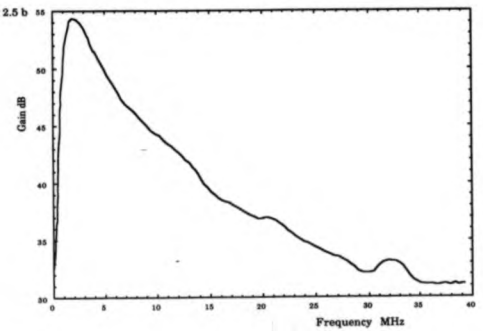

Fig 2.5 c

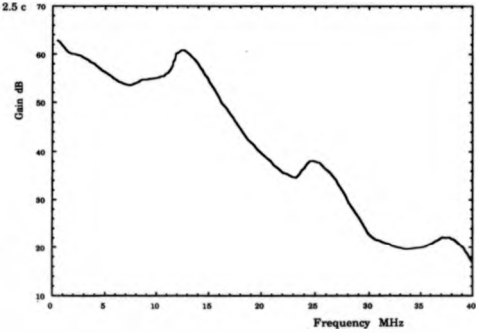

Fig 2.5 d

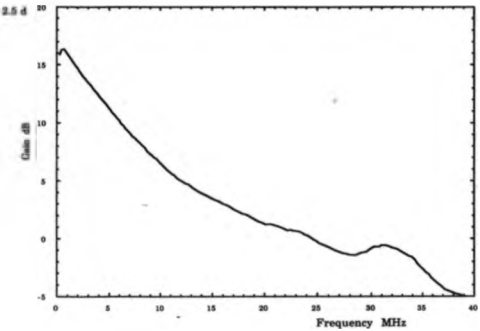

Fig 2.5 Typical pre-amplifier gain- frequency curves used in conjunction with the EMAT detectors .

interference yields either a circular or planar pattern of light and dark fringes. The optical path lengths , at the wavelength of interest , should be equal for both these optical routes to obtain maximum interference contrast upon recombination . Motion of the sample and hence variation in the optical path length in one arm gives rise to a variation in the interference pattern . By counting such "fringe" shifts the displacement of the sample may be determined . The resolution of such a device is of the order of a tenth of a fringe shift when viewed visually , however much greater accuracy is obtained when measured with a photodetector , giving resolvable intensity variations corresponding to displacements of a few Angstroms [24]

The basic Michelson interferometer design was modified by McKie [25] and is shown in Fig 2.6 , the device being capable of resolving displacements of a few tens of picometers . The interferometer light source is derived from a 5mW HeNe (Hughes Corparation 3225H-PC) laser operating at 632.8nm . To ensure laser stability the interferometer optics ensure that no radiation is coupled back into the laser , as would be the case in a traditional Michelson interferometer design . This optical arrangement also ensures that all the available radiation is redirected onto the photodetectors resulting in enhanced signal to noise .The optical detection system is arranged to detect intensity variations in two photodiodes , giving resolvable light level variations of a fraction of a fringe shift , the output of which are fed into a wideband differential amplifier with a gain of 40 .

The omnipresence of low frequency , large amplitude background vibrations , up to ~700Hz producing displacement variations of the order microns in the sample arm of the device , would if not removed swamp the ultrasonic detection . By means of an electro-mechanical vibrator (Ling Dynamics model No. V101) controlled by the low frequency components of the photocurrent , continuous compensation of the reference arm keeps the path

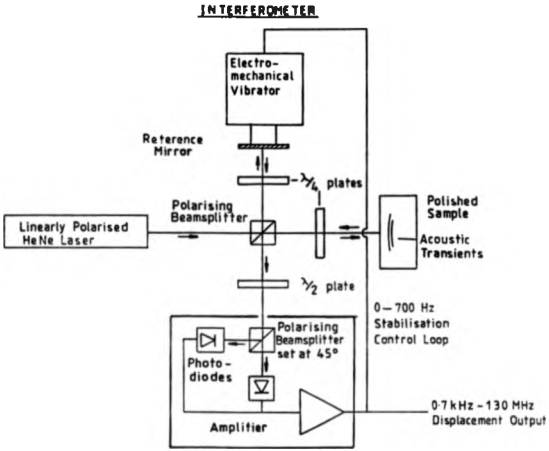

Fig 2.6 Schematic arrangement of the modified Michelson interferometer [after McKie] .

photocurrent , continuous compensation of the reference arm keeps the path difference constant , a technique which removes the requirement to have a air-bed optical table to damp such vibrations .

The interferometer has the great advantage of being an absolute sensor . From the standard derivation for interferometer optics [26] the light intensity obtained from the two interfering beams may be obtained . The use of the differential amplifier removes any D.C. terms in the photodetector output giving a signal output voltage , V , of

$$V = Vo \sin\left(\frac{4\pi x}{\lambda}\right) \qquad 2.17$$

where λ is the radiation wavelength , Vo the peak to peak photodetector output and x the sample surface displacement . For small displacements the small angle approximation may be used and its accuracy may be determined from the series expansion of the sine function , which is to the first two terms

$$\sin(y) = y - \frac{y^3}{3!} \qquad 2.18$$

Thus to give an accuracy of 98% in the displacement y=0.34 rads while for 95% accuracy y=0.55 rads , these values indicate the useful range over which the linear approximation may be employed . To ensure maximum linearity the dynamic range of the device must be maximized , requiring Vo to be as large as possible . To achieve this the reflectivity of the sample under inspection must be large , typically requiring surfaces of near mirror quality .

References Chapter 2

[1]G. Birnbaum & G.S. White "Research Techniques in NDT" (Ed. R.S. Sharp , Academic Press , London) vol 7 (1984)
[2]D.A. Hutchins , "Physical Acoustics" (Ed. W.P. Mason & R.N. Thurston , Academic Press , London) vol 18 (1988)
[3]D.A. Hutchins , D.E. Wilkins & G. Luke , Appl. Phys. Lett. vol 46 (1985)
[4]A.C. Tam & W.P. Leung , Appl. Phys. Lett. vol 45 (1984)
[5]J.F. Ready , Jn. Appl. Phys. vol36 no2 pp462-468 (1965)
[6]J. Cooper Ph.D Thesis chapter 4 Hull University (1985)
[7]J.E. Sinclair , J . Phys. D. vol12 p1309 (1979)
[8]L.R.F. Rose , J.A.S.A. vol75 no3 p723 (1984)
[9]P.A. Doyle , J . Phys. D. vol19 pp1613-1624 (1986)
[10]F.A. McDonald , Appl. Phys. Lett. vol54 no16 pp1504-1506 (1989)
[11]D.A. Hutchins , R. Dewhurst & S.B. Palmer J.A.S.A. vol70 no5 p1362 (1981)
[12]L. Knopoff , J . Appl. Phys. vol29 no4 , (1958)
[13]R.J. Dewhurst , D.A. Hutchins , D.A. Palmer & C.B. Scruby , J . Appl. Phys. vol53 pp4064-4071 (1982)
[14]D.A. Hutchins , R.J. Dewhurst & S.B. Palmer , Ultrasonics , pp103-108 May (1981)
[15]S.J. Davies , Private Communications
[16]H.M. Frost , "Physical Acoustics" chapter 3 vol14 pp 179-275 (Ed. W.P. Mason & R.N. Thurston , Academic Press 1979)
[17]K. Kawashima , IEEE Trans vol SU-31 no2 pp83-94 (1984)
[18]I.S. Grant & W.R. Philips , "Electromagnetism" (Manchester Physics Series , John Wiley & Son , 1984)
[19]M.J.P Musgrove , "Crystal Acoustics" (Holden-Day , San Fransisco , 1970)
[20]E.R. Dobbs , "Physical Acoustics" chapter 3 vol10 pp 127-191 (Ed. W.P. Mason & R.N. Thurston , Academic Press 1973)
[21]M. McCaig , "Permanent Magnets in Theory and Practice" (Pentech Press , London , 1977)
[22]C. Edwards , Ph.D Thesis chapter 5 Hull University (1987)
[23]C. Edwards & S.B. Palmer , Nondestr. Test. Eval. vol5 pp203-212 (1990)
[24]D.A. Hutchins , J. Hu & K. Lundgren , Mat. Eval. vol44 pp1244-1253 (1986)
[25]A.D.W. McKie , Ph.D Thesis chapter 3 Hull University (1987)
[26]E. Hect & A. Zajac , " Optics" (Addison Wesley Publishing , Amsterdam , sixth edition 1980)

Chapter 3

CO_2 Radiation - Metal Interaction

3.1 The TEA-CO_2 Laser Characteristics

The transversely excited ,atmospheric (TEA) CO_2 laser is a high power molecular laser who's lasing mechanism originates from transitions between vibrational energy states of the CO_2 molecule The main lasing transition originates from an antisymmetric to symmetric vibrational mode producing photons with a wavelength of 10.6μm . Associated with this basic transition are accompanying lower energy transitions between rotational states of the CO_2 molecule , which broaden the emitted spectrum to a linewidth of approximately 1GHz . This wavelength is at least one order of magnitude longer than those typically used to generate ultrasound which , as is described later in the chapter , radically changes the laser - matter interaction . A second aspect of this wavelength is that visible optics , such as quartz or crown glass , may not be use to manipulate the radiation as they are opaque at 10.6μm . Focusing must be carried out with either zinc selenide or germanium lenses , preferably anti-reflection coated to reduce the high reflection losses .

The temporal profile of the laser is in some degree governed by the gas mixture used in the lasing process . With a standard gas mix of carbon dioxide , molecular nitrogen and helium , in the ratio 1:1:10 , the temporal profile is characterized by an initial , high power spike , lasting up to approximately 100ns , followed by a lower power tail of duration up to 3μs . If the nitrogen in the gas mix is removed , either completely or partially , the "nitrogen tail" is suppressed leaving only the initial spike . Fig. 3.1 a&b show the temporal profile of the laser pulse with and without the nitrogen content respectively . The profiles were recorded using a "Monolight 7415 " photon drag detector [1] which has a linear output at the power densities used in this work and with a response time of approximately 1ns , has sufficient bandwidth to accurately characterize the lasers temporal spectrum . Fig 3.2

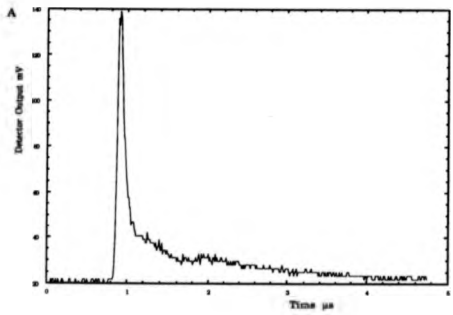

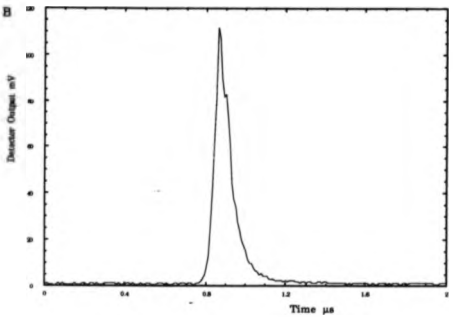

Fig 3.1a & b CO_2 laser pulse temporal profiles measured with and without the nitrogen gas content respectively . Photon drag detector recorded

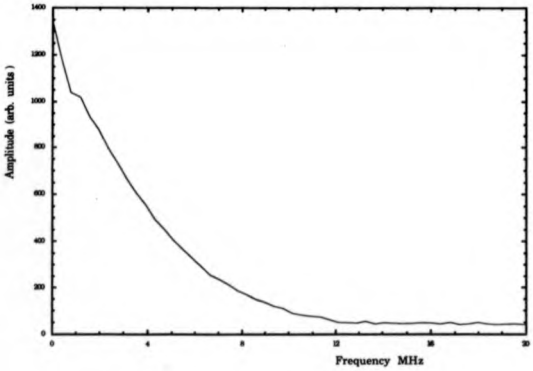

Fig 3.2 The Fourier transform of the reduced nitrogen gas mixture , temporal laser pulse .

shows the Fourier transform of Fig 3.1b , the reduced nitrogen pulse , to determine the frequency spectrum of the initial laser pulse , as it is this region of the pulse which is responsible for the generation of the ultrasound ,and as such indicates the maximum frequency content of the ultrasonic transients . The spectrum shows the frequency content to extend up to a maximum of 10MHz . This value is between one half to a third of that produced by the typical Q-switched Nd:YAG laser pulse discussed in the previous chapter .

The spatial distribution of the laser pulse may be determined by scanning the photon drag detector across the unfocussed beam . To obtain a high spatial resolution the detector was apertured to a width of ~1mm , sufficient to give good spatial resolution while still producing a measurable signal to noise level . Fig 3.3a&b show the results of scans in the x and y directions of the beam perpendicular to the direction of motion . The profiles show a marked difference from the multimode , near Gaussian profile produced by a solid state laser . The width of the square profile CO_2 laser pulse is ~30mm which to a first approximation may be modelled as a top-hat function , a convenient profile to consider when developing wide ultrasonic sources due to its mathematical simplicity . A more accurate means of representing the spatial profile is with a Tukey function which represents a top-hat function modified by smoothly varying edges and is given by :-

$$F(x) = \begin{cases} =1.0 & 0<|n|<\alpha N/2 \\ =0.5\left[1.0+\cos\left[\pi\dfrac{(|n|-\alpha N/2)}{(1-\alpha)N/2}\right]\right] & \alpha N/2<|n|<N/2 \\ =0 & \text{elsewhere} \end{cases} \quad 3.1$$

where N is the half width , n is any point within N and (1-α) is the degree of slope of the sides of the Tukey function . Fig 3.4 shows this function calculated for values of a of 0.5 ,0.7 and 0.9 to demonstrate the suitability of the function in modelling the CO_2 spatial profiles shown in Fig 3.3 .

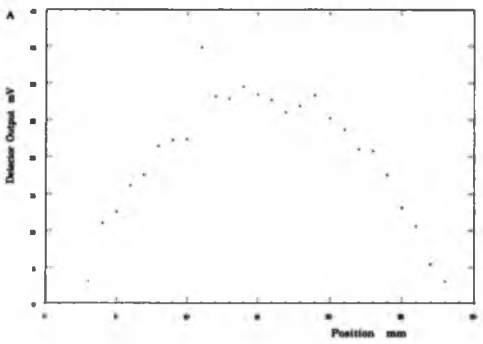

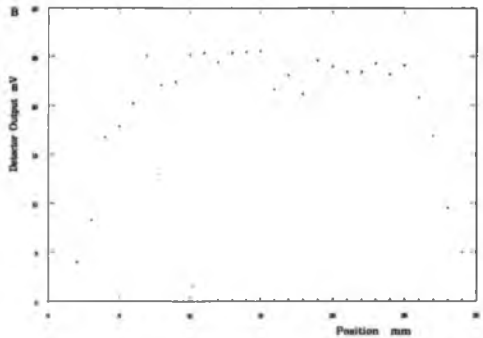

Fig 3.3 a & b Photon drag detector scans across the CO_2 beam profile in the x and y directions respectively

The spatial extent and structure of the CO_2 beam differs in both respects to those described in the previous chapter , in that the spatial width of the beam is almost an order of magnitude larger than that of Nd:YAG lasers and the Gaussian profile is replaced by a near top-hat function which provides an excellent opportunity to investigate wide source , laser - matter , ultrasonic generation .

Knowledge of the laser pulse extent , both spatially and temporally , coupled with the responsivity of the photon drag detector enables the laser pulse energy to be determined . The initial spike which stays fixed in energy to within ~10% with or without the nitrogen gas mix , has an energy of 1.1 ± 0.1 J . The low power tail contains an energy of 2.3 ± 0.2 J , but as will be described in the course of this work does not contribute significantly to any ultrasonic generation . Direct measurement of the entire beam by focusing all the energy onto the detector would produce a more accurate value for the beam energy but this would have exceeded the power limit of the device .

3.2 Interaction of CO_2 laser radiation with an atmosphere

" A short duration flash of laser light can set the air on fire " [2] . This is in fact the phenomena of multiphoton ionization , (MPI) , leading to plasma breakdown of the air or any gas into which the radiation is focused . Short duration laser pulses , of the order of a few nanoseconds in duration , provide an extremely high photon flux and power densities in the range 10^6 - 10^{13} Wcm^{-2} . If a photon of energy 1.17 eV , as derived from a Nd:YAG laser is incident onto a gas atom or molecule , excitation of the electron state of the molecule may occur although to a level well below the ionization energy of the irradiated molecule , which is a factor of approximately eleven times greater than the photon energy . The excited molecule will stay in the excited state for

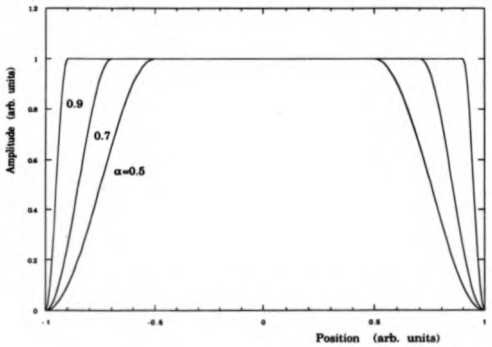

Fig 3.4 Tukey functions calculated for a range of α , the uniformity parameter .

a characteristic time , Δt ,governed by Heisenburg's uncertainty principle which states that

$$\Delta t \, \Delta E > \frac{h}{4\pi} \qquad 3.2$$

where E is the energy of the excited state and h is Planck's constant . If a second photon strikes the atom in a time less than Δt the electronic state will be further increased in energy , provided a suitable energy level is available for the electron to occupy . Thus if a number of photons strike the atom or molecule in a time characteristic of the decay time of an electron close to ionization , then ionization of the molecule will occur . If the ionization energy of the irradiated molecule is say E_i and the energy of the flux quanta is ε then the number of photons required to produce ionization is simply :-

$$n > \frac{E_i}{\varepsilon} \qquad 3.3$$

Substitution of E_i into eq 3.2 gives the time interval over which the n photons are required to strike the molecule and hence the flux , F , defined as the number of photons per second per cm^2 , required for MPI which is therefore given by :-

$$F = \frac{2 \cdot E_i^2}{h \varepsilon A} \qquad 3.4$$

where A is the area or cross section of the irradiated atom or molecule . With $E_i \sim 13.5eV$ a typical value for oxygen and nitrogen ionization energies , a flux of the order 10^{31} photons/sec/cm^2 , is required for MPI assuming a photon-molecule collision cross-section of 10^{-16} cm^2 . Such levels of flux are easily obtainable from lasers such as Nd:YAG . The result of such MPI in the irradiated volume is to change the gas into a highly ionized plasma , over the time duration of the laser pulse . This phenomena is characterized by high temperatures and pressures with the plasma leading to a high optical

emission and a shock wave generated in the air , the dynamics of which are discussed later in the chapter .

CO_2 lasers operating at 10.6μm deliver photons which have an energy down by an order of magnitude on those produced by Nd:YAG lasers . Therefore an even greater flux is required if MPI is to occur . The laser used in this research delivers a flux of $\sim 10^{28}$ photons/s/cm^2 which is several orders of magnitude too low to produce such an interaction .

Gas breakdown may however occur with radiation at this wavelength under certain conditions . The requirement of producing electrons by MPI of the air molecules to produce a plasma may be lifted if the radiation is focused into a region containing a high electron concentration or molecules such as hydrocarbons which , in comparison to oxygen or nitrogen , have a greatly reduced ionization energy . If such molecules are present ionization of these species may occur to produce an electron rich environment . These electrons subsequently absorb the incoming radiation via a process of inverse Bremstrahlung absorption [3] to become excited and create further electrons by collisional ionization of surrounding gas atoms and molecules . Such a process leads to a cascade of high energy electrons and ions resulting in plasma breakdown of the gas . It is this "seeding" of the irradiated focal region with a high electron concentration which is the mechanism by which plasmas are generated above metal surfaces . The presence of a rapidly expanding , energetic plasma just above the irradiated solid is the source of the pressures and stresses required for the generation of ultrasound .

3.3 10.6μm radiation interaction with a metal

As described in chapter 2 the lasers traditionally employed to generate ultrasound in metals rely on an absorption mechanism and as stated have a percentage absorption of the incident radiation between 7% to 20% .

Inspection of eq 2.1 , which is a valid approximation for infrared wavelengths as the interaction dose not involve any electron-photon coupling , shows the absorption is proportional to the square root of the frequency of the radiation signifying that the 10.6 μm radiation is absorbed by a factor three times less than 1.06 μm radiation . Quoted figures for 10.6 μm radiation absorption on clean metal surfaces give for aluminium a value of ~0.01 and a value of ~0.02 on iron [4] .This reduction in the absorption of the incident laser radiation at longer wavelengths implies that the ability of CO_2 lasers to generate ultrasound by an absorption mechanism is negligible and thus any interaction observed in the form of a transient strain field , may be considered as originating from the action of the plasma above the surface of the metal .

The presence of a metal target /sample in the focal region of a CO_2 laser beam reduces the power density required for breakdown of the surrounding gas by two to three orders of magnitude , on that required for multiphoton ionization of clean air . The target , be it metal or non-metal , acts as the source of the initial electron concentration , as was the case for hydrocarbons in air . Having provided sufficient electrons , in time scales less than the laser pulse duration , cascade ionization occurs resulting in the development of a plasma .

The metal may provide this initial high electron concentration upon irradiation by one of two processes . Firstly metals , unless thoroughly cleaned always contain some degree of surface contamination , such as metal oxides and absorbed air impurities such as hydrocarbons or even dust particles . These may provide a potential reservoir of easily created electrons as their ionization energy , or in the case of bulk material their work function , is greatly reduced in comparison with most metals , the effect of such impurities is considered more closely in chapter 4 . The second method of primary electron generation originates from small surface defects and thermally uncoupled "flakes" of target material .

The calculations of Ready [5] of the surface temperature rise introduced in chapter 2 , show that irradiation of a pure target with a focused 1J , 10.6 μm pulse would only induce a surface temperature rise of ~100 C . This relatively low temperature increase is insufficient for vapourisation or thermionic emission of electrons to occur , hence the required electron density may not be achieved from a perfect surface . The low temperature increase is due both to the very high reflectance of metals to the wavelength radiation and also their high thermal conductivity , thus any localised temperature increase is rapidly dissipated into the cold bulk of the material . C.T. Walters [6] considered the presence of small , in the range 0.5 μm - 2μm , thermally uncoupled flakes of material on the surface of the sample under irradiation . Fig 3.5 shows the two types of defect considered . These defects are either surface delaminations , or a sub-surface void or low conductivity impurity existing just below the surface . Both types of defect give rise to a greatly reduced thermal coupling to the bulk of the sample therefore greatly reducing the heat flow away from this region . Scanning electron microscope (S.E.M.) pictures , taken by the authors [6] , of samples studied showed these two defect types to be most common .

The rise in temperature , Δt , for such a defect upon irradiation by a linearly rising incident power density , a valid expression for the leading edge of a laser pulse , may be calculated using a one dimensional , uniform heat equation given as

$$H = mc\Delta t \qquad 3.5$$

where H is the heat input , m is the mass of irradiated material and c its specific heat . Where the energy input is determined by

$$H = \int_0^t \alpha' G' \, dt \qquad 3.6$$

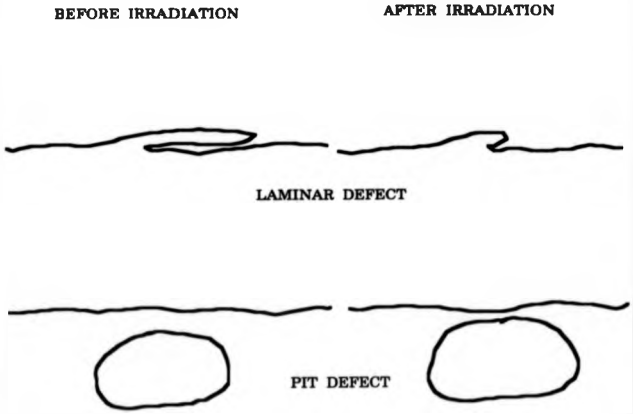

Fig 3.5 Surface defect types considered to be the origin of thermionic electron emission in the initiation of gas plasmas . [after Walters]

where α' is the material absorbance and G' the rate of increase of laser energy . Rearranging eq 3.5 and substituting the known expressions for the mass and heat input gives the temperature rise to be

$$\Delta t = \frac{\alpha' G' t^2}{2\rho c d} \qquad 3.7$$

where ρ is the material density and t is the time after the start of the laser pulse .The absorbance , α' , is however strongly temperature dependent and has a discontinuity at the melting point . Fig 3.6 shows the dependence of the absorbance with increasing temperature on aluminium as calculated by Weyl et. al. [7] , which gives a post melting point absorbance of ~ 6% . This value is however much lower than the value of 48%, based on the experimental work of Bergel'son [8] , a figure used in the work of Walters [6] to determine flake temperature rise . The temperature rise calculations from Walters [6] , suggest that for an incident power density of 10^8 Wcm^{-2} , the defects reach thermionic and vapourisation temperatures , of the order 600 C - 1200 C within approximately 30 ns .

The electrons emitted from such a source into a standard pressure atmosphere , build up close to the sample surface with a characteristic distance of the Debye length , λ_d , expressed as

$$\lambda_d = \left(\frac{k_B T_e}{4\pi n_e e^2} \right) \qquad 3.8$$

where k_B is Boltzmann's constant , T_e the electron temperature , n_e the electron density in cm^{-3} and e the electronic charge . This is a common phenomena of plasmas and relates to the screening distance of a central charge by electrons or ions of which the plasma is comprised [9] . The electrons are attracted back towards the positively charged sample surface but are not absorbed by the sample due to it's elevated temperature and the high electron energy . Typically the Debye length is of the order 10^{-6} m for an

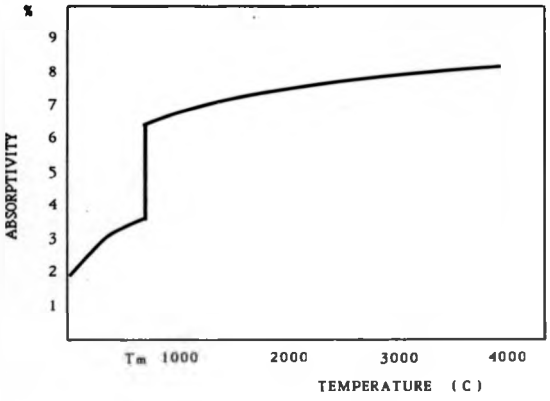

Fig 3.6 Variation in the absorptivity of aluminium as a function of temperature for an incident radiation wavelength of 10.6μm . [after Weyl et. al.]

electron concentration in the range 10^{13} - 10^{15} cm^{-3} . Without an atmosphere present the thermally emitted electrons have enough energy to escape the electrostatic potential of the sample and no such charge layer builds up close to the sample . Thus the ambient gas assists the electron buildup by resisting such an electron drift .

3.3.1 Air breakdown and Breakdown threshold Intensities

The action of the incident laser beam on the sample surface creating the localized region of high electron density is the first stage of plasma breakdown of the surrounding air . The electrons absorb the incident and reflected radiation , which comprises approximately one third of the total power density. The absorption of the incident photons occur via a process of inverse Bremstrahlung absorption increasing the electron kinetic energy . These energetic electrons undergo many collisions with vapour and gas molecules and atoms either producing excitation and subsequent ionization or undergoing elastic collisions to the gas atoms creating heating .

Several authors have considered this problem with varying degrees of complexity , including elastic and inelastic collisions , de-excitation of electrons ,electron - electron interactions and diffusion losses . Walters [6] considered the case where all the absorbed energy goes into ionization of the surrounding gas atoms and molecules . The heating of the gas , via elastic collisions was considered minimal and thus neglected in the analysis . The rate of electron density increase was shown to be linearly proportional to the laser power density , G , and inversely proportional to the ionization energy E_i as given below

$$\frac{dn_e}{dt} = \frac{\chi G}{E_i} \qquad 3.9$$

where χ is the electron - radiation absorption coefficient . Integration of equation 3.9 with the boundary condition that before irradiation the electron

density is n_o , which may be determined by the Saha equation [10] , gives the time for breakdown as

$$t = \frac{(n_e - n_o)E_i}{\chi G} \qquad 3.10$$

which for an incident power density of $5 \cdot 10^8$ Wcm^{-2} gives a time for full ionization and hence breakdown of ~ 2 ns .

Weyl et. al. [7] considered a much more rigorous model of electron - atom interactions where individual excitation energies of aluminium were analysed and the population growth of these states was monitored throughout the course of the laser pulse until breakdown was initiated .The problem may be stated by two rate equations , which determine the population of the two main pre - ionization electron excitation levels , given by

$$\frac{dn_1}{dt} = \alpha_1 n_e n \qquad a$$

$$\qquad 3.11$$

$$\frac{dn_e}{dt} = \alpha_i n_e n_1 \qquad b$$

where $\alpha 1$ is the rate coefficient of excitation , αi the rate coefficient of ionization ,n the atom number density ,ne the electron density and n1 the first excited state density . These equations are coupled by the energy conservation equation given by

$$(1+R)\chi I_{inc} = \varepsilon_1 \frac{dn_1}{dt} + (\varepsilon_i + E_i)\frac{dn_e}{dt} \qquad 3.12$$

where $\varepsilon 1$ is the electron excitation energy , R is an average reflection coefficient over temperature and Iinc is the incident radiation energy .

Dividing eq 3.11b by eq 3.11a and integrating gives n_1 in terms of ne which upon substitution into eq 3.12 gives the time history of the excited electronic state . Further manipulation then yields the time history of the ionized electrons . The results of these calculations shows that initially the

number of excited atoms increases steadily while the electron concentration stays constant at the Saha value for a cold gas .This continues until the population of excited atoms reaches a critical value after which the electron density rises rapidly by several orders of magnitude , to a figure of $\sim 10^{18}$ cm^{-3} over timescales of a few nanoseconds , a result which is in good agreement with the more simplistic approach of Walters [6] . Weyl [7] calculated that only 5% of the incident energy is used in heating the gas , the remaining 95% being involved in the excitation and ionization process . This explains the strong agreement between the two approaches and the success of Walters simplistic model . Both models require the incident power density for plasma breakdown to be achieved to be approximately $5*10^7$ Wcm^{-2} a value two orders of magnitude lower than required for clean air breakdown .

A slightly different approach , but one which again produces a valid result , was proposed by Barckukov et. al. [11] , who stated that the requirement for avalanche development to be satisfied was that the rate of growth of electron energy should exceed the rate of electron energy losses , due to elastic collisions with atoms . The resulting expression for the power density threshold S , in Wcm^{-2} was given in the form

$$S = 5.7*10^9 \frac{g}{A^*} \frac{\Delta^*(eV)}{\lambda^2(\mu m)} \qquad 3.13$$

where A^* is the mean atomic mass of vapour particles , Δ^* is the mean ionization energy and g is a loss coefficient due to elastic losses . The attraction of this result is that one may simply plug in known values for the irradiated species and the wavelength of the incident radiation to determine a direct value for the breakdown threshold . This model is particularly suited to the case of oxide layers and absorbed impurities present on the target surface , where analysis of the rate of excitation and growth of individual species would be a highly complex task . This result predicts a clean metal breakdown

threshold of the order $\sim 10^7$ Wcm^{-2} being reduced to $\sim 10^6$ Wcm^{-2} if surface oxides are present . Chapter 4 describes an experimental test of this approach .

3.3.2 Spectral Emission Studies

As verification of the proposed breakdown mechanism spectral emission studies have previously been undertaken to yield information about the atomic species present in the plasmas . These studies were undertaken to determine whether breakdown of air at such low power densities is possible or whether a simple , high luminosity ,vapour plasma of the irradiated sample material is achieved .

Wei [12] used a long pulse , 5-15 μs , 18 J , CO_2 laser to irradiate a variety of target materials . The spectrographs obtained contain predominantly N^+ and O^+ with a lower N^{++} and O^{++} content . The spectrographs revealed that no atomic or diatomic species were present and any presence of target material in the plasma was extremely low . By considering the transition temperatures for N^+ to N^{++} and for O^+ to O^{++} the plasma temperature was estimated to be in the region of $\sim 25 \cdot 10^3$ K . A second and possibly more physically pleasing temperature estimation was carried out on the background continuum of the spectrographs . Using Planck's black body theory a temperature estimate of $\sim(15\pm5) \cdot 10^3$ K was achieved . These measurements were supported by those taken by Bakeev [13] who used photometric analysis of the spectrographs , to compare the brightness of N^+ and O^+ lines and gave estimates for the plasma temperature to vary between $(10 - 15) \cdot 10^3$ K as the incident power density was increased from 1 - 4 MWcm^{-2} . These results show therefore the plasma to be comprised of the surrounding gas atoms and is not a vapour plasma .

Therefore the previous analysis of low threshold air breakdown is valid and one may conclude that the sample under irradiation serves only to create a sufficiently high localised electron density after which time it plays little part

in the breakdown process . This contrasts strongly with the absorption mechanism used traditionally for laser generation of ultrasound .

3.4 Plasma Development & Dynamics

Once the cascade ionization has produced an electron density of the order 10^{18} cm^{-3} , breakdown of the surrounding gas in well established . The subsequent development of the plasma is determined by the incident energy , pulse duration and the area of the irradiated region as well as the initial electron concentration produced during the cascade . The strong radiation - plasma coupling is responsible for the subsequent plasma development . To demonstrate the basic photon -plasma interaction consider a flux of photons , of frequency ω , incident on a plasma of electron density n_e in zero magnetic field . The expression for Amperes law in a vacuum , which contains no current density term must now be changed to include currents originating from plasmas electron motion . The effect of this term upon the electromagnetic field is to change the dispersion relation of the waves , which in vacuum is simply $\omega=kc$ where k the wavenumber and c the speed of light .This relation for light in a plasma becomes :-

$$\omega^2 = \omega_p^2 + c^2k^2 \qquad 3.14$$

where ω_p is termed the plasma frequency . The plasma frequency is related to the electron density via the expression

$$\omega_p = \left(\frac{n_e e^2}{m\varepsilon_o}\right)^{1/2} \qquad 3.15$$

where e and m are the electronic charge and mass respectively and ε_o is the permativity of free space . The consequence of eq 3.14 is to prevent electromagnetic waves from existing in the plasma if their frequency is below

the plasma frequency . If this is the case the waves become damped and decay exponentially within the plasma , to a characteristic skin depth δ given by

$$\delta = \frac{c}{(\omega_p^2 - \omega^2)^{1/2}} \qquad 3.16$$

The variation in plasma skin depth as a function of electron concentration , which is related to ω_p via eq. 3.15 , for 10.6 μm radiation is shown in Fig 3.7 , which shows the absorption depth to pass through a sharp transition for electron densities of $\sim 10^{19}$ cm^{-3} . Below this concentration the plasma has effectively infinite penetration depth , thus radiation passes through the plasma and over time scales of the laser pulse continues to produce electrons within the bulk of the plasma . The plasma consequently expands hemispherically and stays in contact with the target throughout its time history . This type of plasma growth or motion is termed a "laser plasmotron " [11] , or a 3-D plasma expansion .

For very high incident power densities the initial electron concentration of the gas plasma exceeds 10^{19} cm^{-3} . The incident radiation is rapidly shielded from the target and penetrates the surface of the plasma by only a few microns . The expansion of this leading edge is , to a first approximation , one dimensional as the area of the focused radiation is approximately two orders of magnitude larger than the absorption depth . Therefore as the laser pulse continues the plasma travels back towards the direction of the laser . The front edge of the plasma fills the caustic of the focused radiation , which increases in area closer to the lens and hence the power density decreases as the plasmas electron density is also decreasing . This leads to the plasma becoming transparent to the radiation where upon it is transformed into a spherically expanding plasma similar to the laser plasmotron . It is important to note that this type of plasma behavior couples only briefly to the target surface before it becomes detached , a feature which contrasts strongly

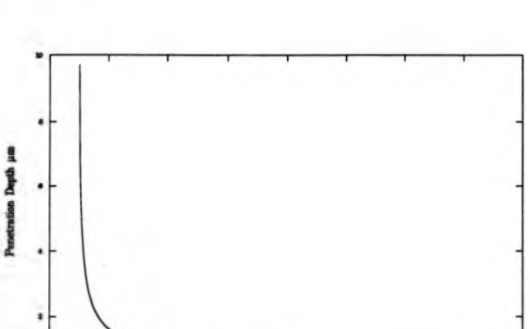

Fig 3.7 The variation in absorption depth of CO_2 radiation within a plasma .

to the laser plasmotron motion . This type of plasma motion is termed a " laser detonated wave "[14] .

These two types of laser supported plasma motion are the limiting cases of the plasma behavior for low and high power densities respectively and are shown in the time integrated photographs in Fig 3.8 generated above an aluminium sample . The top photograph shows the typical form of a 3-D plasma which can be seen to be in close contact with the target surface , whereas the bottom photograph of a laser detonated wave , shows how the plasma moves away from the target and at a later time expands radially as it becomes transparent to the incident radiation . The increase of incident power density results in a gradual transition from one source type to the other .

A more detailed method by which the plasma growth may be observed is with a streak camera [15] . This type of camera , which can scan on timescales of the order nanoseconds , gives the time history of the plasma position away from the sample surface . The experimental arrangement used to record the plasma motion is shown in Fig 3.9 , with the camera positioned parallel to the target surface thus recording the plasma motion in this direction . Fig 3.10 a,b,c shows a series of streak camera measurements with the CO_2 laser working with a reduced gas mixture . The photographs show , from top to bottom , the transition from a laser plasmotron (L P) to a laser detonated wave (L D W) . Timing measurements show the plasma to stay in contact with the target surface for 360 ns , with the L P source shown in Fig a , while Figs b & c which are increasingly more L D W in nature persist at the target surface for 20ns and 10ns respectively . The corresponding streak camera photographs recorded with the nitrogen present in the laser gas mixture are shown in Fig 3.11 a,b,c,d , again showing the transition from L P to L D W plasma motions . The presence of the increased tail energy enhances the definition and duration of the plasma motion as is dramatically shown in Fig 3.11 d showing the extremely rapid motion of the plasma away from the target surface . Timing

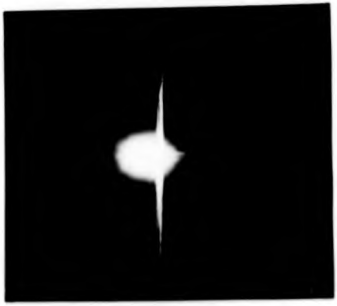

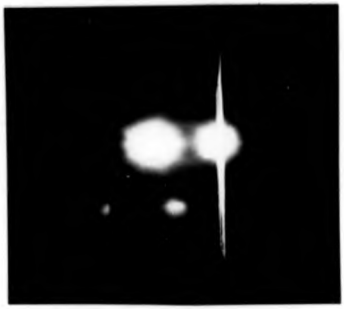

Fig 3.8 a & b Time integrated photographs showing the characteristic motion of the L.P. and L.D.W. plasma motions .

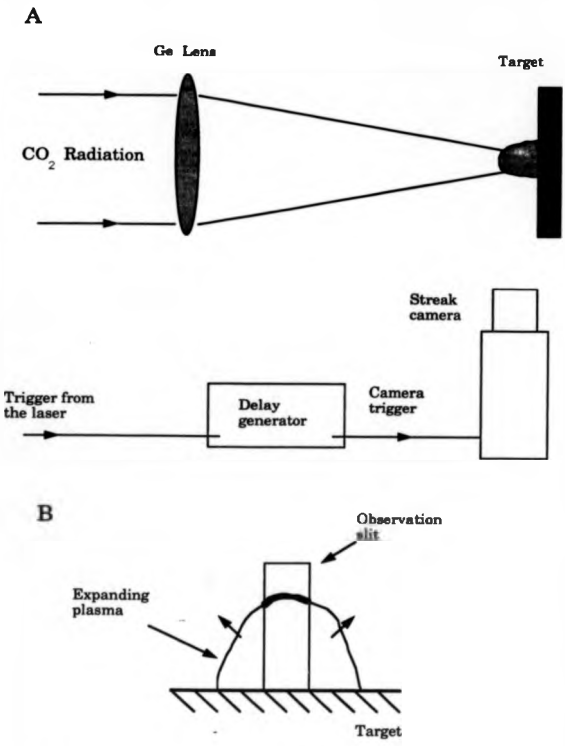

Fig 3.9
a:Experimental arrangement to record the plasma growth with the streak camera .
b: Allignment of the camera's observation slit with respect to the expanding plasma and the target surface .

measurements on the persistence of the plasma at the sample surface give values of 800ns , 500ns , 50ns and 300ns respectively . The final value of 300ns describes the presence of only a weak plasma which is shielded from further growth by the detached plasma above the target .

3.4.1 Reflection Photometry

To verify the timescales proposed for heating and breakdown to occur a study of the radiation - plasma interaction was undertaken . Bessarab [16] and Zyung [17] used a method of transmission photometry , where the sample under inspection had a small hole drilled through it . The hole diameter was chosen to be large enough to allow the maximum possible radiation to pass giving sufficiently high sensitivity photon drag detector measurements , placed behind the sample , while being small enough so as not to perturb the breakdown mechanism , threshold or plasma dynamics . The geometry of this experiment was changed so as to work in reflection , as shown in Fig 3.12 . This arrangement has two advantages . Firstly the surface off which breakdown is initiated is unchanged and hence these measurements are easier to correlate to other measurements in this work . Secondly the photon drag detector potentially samples a much greater portion of the radiation , due to the high sample reflectivity , giving an increased sensitivity . The sample under inspection was cleaned prior to the experiment to remove any surface impurities which may lead to spurious results . The power density variations were made by varying the focusing lens - sample separation . This leads to a change in solid angle of the reflected radiation and thus the fraction of the reflected energy sampled by the detector , which must be accounted for in the data analysis .

Two measurements can be made from this experiment , the risetime of the reflected pulse Δt_1 , as an indication of the time taken to accomplish

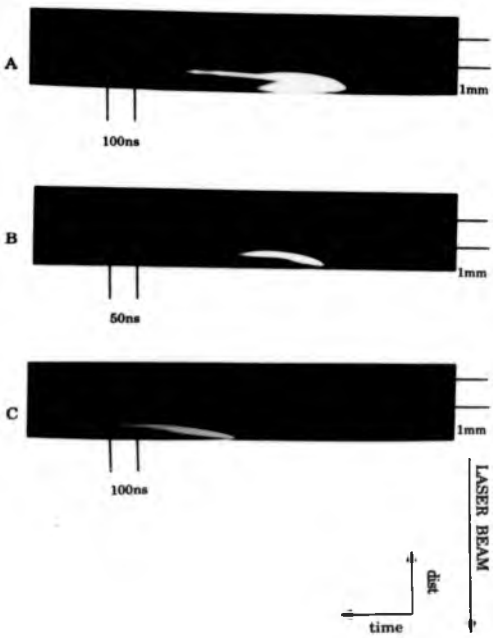

Fig 3.10 a , b & c Streak camera measurements for increasing laser power density showing the transition from L.P. to L.D.W. plasma motion . Recorded with the reduced nitrogen gas mixture .

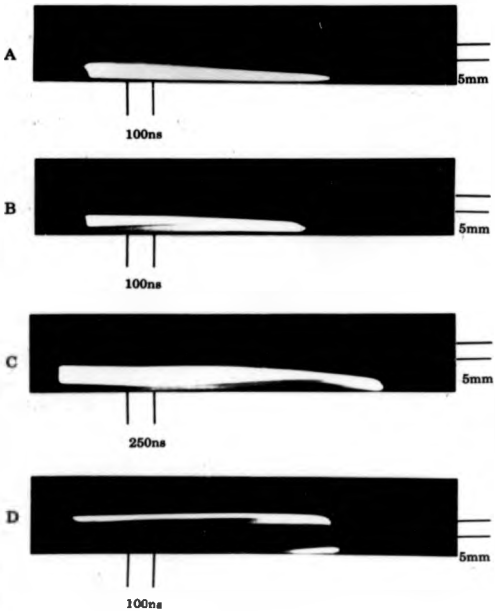

Fig 3.11 a , b , c & d Streak camera measurements for increasing power density showing the plasma motion transition from L.P to L.D.W. Recorded with the nitrogen tail present in the gas mixture , leading to enhansed plasma duration .

breakdown and secondly the width of the pulse , Δt_2 , recorded above a threshold as a measure of the time to which the incident pulse was able to penetrate the plasma . Fig 3.13 a,b,c show pulse shapes recorded , demonstrating the effects of increased plasma absorption of radiation in the transition between L P and L D W .

Fig 3.13 c shows that when the laser power density is sufficiently high such that the plasma almost instantly shields the target then the measurement Δt_1 corresponds to the time taken for thermionic emission and subsequent gas breakdown to occur . This value was gradually decreased from the laser pulse risetime observed under the action of a weakly absorbing L P to a value of 30ns when the radiation passed through a L D W . These results support the calculations of Walters [6] , who predicted that heating times of approximately 30 ns for power densities in the range 10^8 Wcm^{-2} were sufficient to create a high enough electron density from which breakdown may be induced , thus supporting the claim that surface defects are a necessary feature in low threshold gas breakdown .

Fig. 3.14 shows the variation of the pulse width , Δt_2 , above a threshold level , as a function of power density . Qualitatively this data shows the variation in laser penetration depth into the plasma with varying electron concentration . The general form of the curve agrees well with the theoretical calculations presented in Fig 3.7 . The results show no absorption of the beam at low power densities , corresponding to the L P source , while as the incident power density is increased a rapid increase in absorption occurs due to the high electron concentration associated with the L D W plasmas . Quantitative measurements are not readily obtained from the experiment as the measured widths contain the pre - breakdown heating times as well as the penetration time of the radiation . A further complicating factor is that the radiation interacts with the plasma who's electron density is time varying as well as its physical dimensions . However the sharp increase in beam

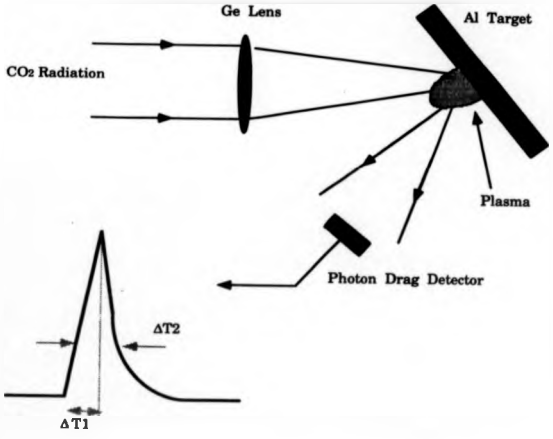

Fig 3.12 Experimental arrangement used to study the absorption of CO_2 radiation within a laser induced plasma .

absorption may be associated with an electron concentration of the order 10^{19} cm^{-3}.

3.5 Surface Pressures and Impulses delivered to the Target due to the Plasma

The measurement of pressures and impulses induced in targets due to the action of a laser supported plasma has been undertaken by many authors . A distinction must be made between high energy , long pulse CO_2 laser sources and the millisecond and below laser pulse sources which produce very differing total impulses .

Lowder [18] reported on a series of experimental measurements recorded with a CO_2 laser capable of producing 500 J delivered with an initial 200ns spike followed by a lower power 15 - 20 μs tail . The power densities delivered , being ~ 10^8 Wcm^{-2} , were such that a L P source was mainly produced above the target , the power density being insufficient to generate a fully defined L D W . The impulse delivered was measured using a ballistic pendulum , while buried piezoresistive carbon pressure gauges measured the peak pressures exerted on the sample surface . The measured impulses for a range of input energies showed a linear behavior , having a gradient of 5 dyne-sec/J , up to an input energy of ~75 J , whereafter the gradient fell representing lower coupling of the radiation to the target . This is a result of increased absorption of the radiation away from the surface and more significantly due to the dimensions of the plasma exceeding the sample dimensions , as the impulses obtained were found to increase for increasing sample size . The peak pressure as a function of peak power density measurements showed a 3/2 power law increase in pressure for peak power densities in the range 10^7 - 10^9 Wcm^{-2} , the region of interest in this work . Enlarging the focal spot diameter increased the coupling between the plasma

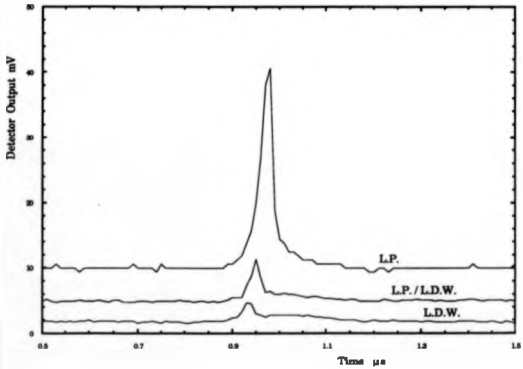

Fig 3.13 Photon darg detector outputs for the reflection photometry experiment showing the beam absorption for increasing plasma electron density .

and the target as indicated by increased peak pressures being observed . Two factors for the increase in peak pressure as a result of increasing source size were proposed . Firstly enlarging the spot size makes the impulsive source tend from a spherical blast wave to a more planar wave and secondly lower shielding results from a lower electron density .

These observations were complemented by the work carried out by Ready [19] who used a TEA - CO_2 laser, similar in energy and pulse duration to that used in this work , in an attempt to correlate long and short pulse measurements of delivered impulse . Impulse measurements showed only a very weak dependence on sample material and the results obtained were in close agreement with Lowder [18] , obtaining an impulse in the range 5 - 6 dyne - sec/J , over a range of incident energies from 0.3 - 1 J . Ready proposed that the plasma source may be modelled using spherical blast wave theory , with the origin of the blast originating from a height just above the sample surface Using this analysis the shock wave radius , R_f ,is given by :-

$$R_f(t) = S(\gamma)\, t^{2/5}\, Er^{1/5}\, \rho^{-1/5} \qquad 3.17$$

where $S(\gamma)$ is a known function of the ratio of specific heats , Er the energy release and ρ the density of the gas . An instantaneous input of energy is considered in this model as the shock wave and plasma exist for timescales several orders of magnitude longer than the 100ns pulse duration . Fig 3.15 shows the expected pressure distribution behind the shock front . Pirri [20] gives the form of the pressure , p , directly behind the blast front as a function of time as

$$p = \rho V^2 \sim E R_f^{-3} \sim E(E/\rho)^{-3/5}\, t^{-6/5} \qquad 3.18$$

where V is the blast velocity and E is the input energy . Fig 3.15 shows the pressure to be sharply peaked at the outer radius of the blast wave with an average pressure of approximately one half that in the bulk of the expanding

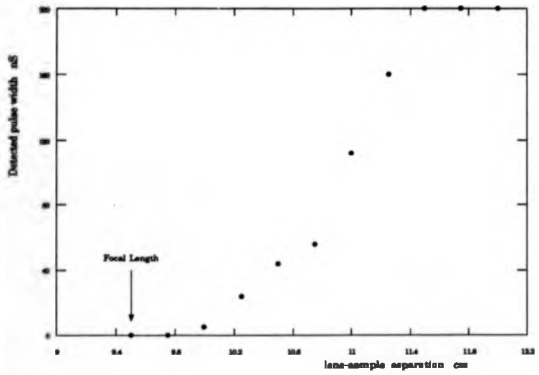

Fig 8.14 Variation in laser pulse width as a function of increased plasma density produced by increased focusing .

shock wave , being a good approximation for $0.1R_f < r < 0.9R_f$. Calculation of the impulse delivered by such a spherical blast wave requires integration of the pressure over the surface of the target at a given instant in time and then integrating over a time duration from when the blast wave first strikes the target and ends when the shock wave pressure equals one atmosphere . The result of the impulse calculation showed that as the surface - blast wave separation increases the impulse decreases , where a L D W was modelled as having a larger separation than a L P . The results gave an impulse per energy delivered in the range 4 - 6 dyne-sec/J , corresponding closely with the experimental data .

The complexity of this model was extended by Ageev [21] , amongst others [22,23] , in response to their own experimental data which yielded a greater variation in impulse per joule values dependent on the plasma motion . Ready's paper indicates that only a weak L D W was developed and hence the impulse delivered was derived mainly from a L P source type . The spherical shock wave theory , which defines accurately the L P source is replaced by a cylindrical shock wave theory to model the L D W motion . This approach considers a shock derived from a column with a defined energy release per unit length .

The calculation of the impulse delivered to the sample using the two separate models of shock wave motion were repeated . The results , obtained were for the case of large target radii where the plasma pressure reaches atmospheric prior to the shock front traversing the edge of the target . They show a large variation in the delivered impulse for the two cases . The upper limit of impulse per joule for the spherical problem was determined as 32 dyne-sec/J while for the cylindrical case the upper limit was 7.5 dyne-sec/J . These values are larger than the above figures quoted due to the large sample radius limit used . The results obtained were in excess of the experimentally measured values , however the calculated variation between the two limiting

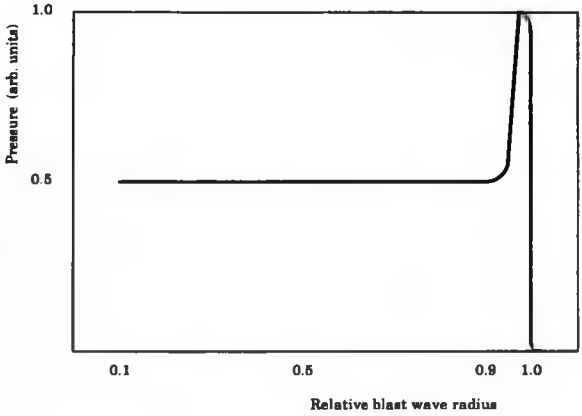

Fig 3.15 Blast wave pressure profile as predicted from shock wave theory . [after Pirri]

cases were in close agreement with experiment . Beverly [24] commented on the results obtained from the spherical and cylindrical blast wave theories which over-predict the impulse delivered to the target . The blast wave models used assume an ideal square wave laser pulse ,having a constant intensity over its duration , uniform intensity over the focal spot and surface initiation . None of these conditions are met in practical experimental cases , especially the assumption of uniform surface initiation . As described in the theory of Walters [6] ,the plasma is initiated at several defect sites on the target surface , which join together after a short time . Therefore the initial radiation energy to shock wave coupling is reduced due to the fact that a large proportion of the energy is not involved in initiating the plasma , but simply in heating of bulk material . The degree to which this reduces the impulse is not discussed by Beverly [24] and is difficult to quantify as only the initial impulse is effected by this problem . Once the individual plasma components have joined the problem becomes essentially the same as theory for the remainder of the pulse .

3.6 Surface Damage

Scanning electron micrographs of the sample after irradiation have been taken to show the extent of the surface damage produced by the breakdown process . Fig 3.16a shows an SEM picture of an aluminium sample irradiated once using a 200 mJ , Nd:YAG laser having an average power density of $\sim 10^9$ Wcm^{-2} . The strong absorption associated with 1.06 μm radiation in metals to produce an ablative interaction leaves significant damage to the depth of a few microns . By contrast Fig 3.16b shows a similar sample irradiated twenty times by a CO_2 laser pulse producing well developed plasma . The degree of surface damage is significantly less than that produced by the Nd:YAG laser . The damage produced by the CO_2 laser is

characterized by a series a series of concentric circles emanating from the centre of the laser source . Such damage patterns are typical of those produced by 10.6 μm radiation on materials as reported by Emmony [25] . Scattering of incident radiation by small surface defects , such as scratches , produces a wavefield which interferes with the incident electric field . The result is to produce a typical interference pattern consisting of circular fringes . Enhanced surface damage occurs at the points of constructive interference hence leaving a visible trace of the phenomena . The picture in Fig 3.16b however has a fringe spacing well in excess of the 10.6 μm separation one would expect from such an interaction mechanism , a fact which is not understood .

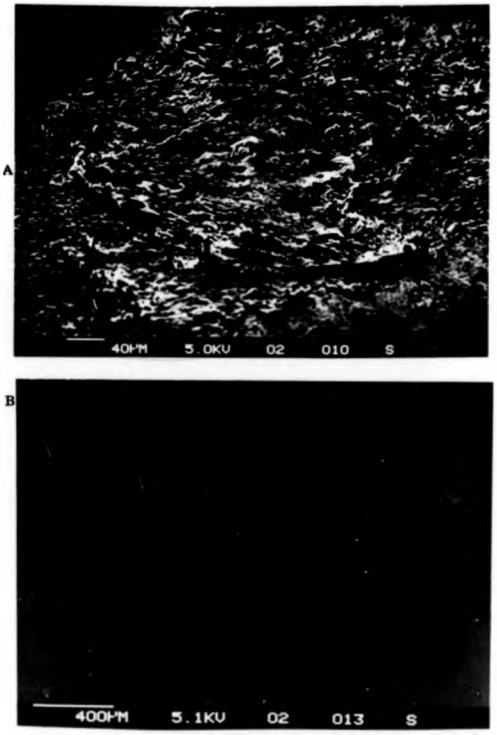

Fig 3.16 S.E.M. photographs of surface damage resulting from Nd:YAG and CO_2 irradiation of aluminium , respectively .

[————————————]

References Chapter 3

[1] A.F. Gibson , M.F. Kimmitt & A.C. Walker , Appl. Phys Letts vol17 no.2 pp75-77 (1970)

[2] C. Grey Morgan , Sci. Prog Oxf vol 65 pp31-50 (1978)

[3] R.A. Grandey , "Strongly Coupled Plasmas" (Ed. Gabor Kalman , Plenum Press 1978)

[4] G.W.C. Kaye& T.H. Laby "Tables of Physical and Chemical Constants" (Longman sixth edition 1973)

[5] J. F. Ready , J. Appl. Phys. vol36 no2 pp462-468 (1965)

[6] C.T. Walters , r.H. Barnes & R.E. Beverly III , J. Appl Phys vol45 no5 (1978)

[7] G. Weyl , A. Pirri & R. Root , AIAA Journal vol19 no4 p460 (1980)

[8] V.J. Bergel'son , A.P. Golub' , I.B. Nemchinov & S.P. Popov , Sov. J. Quant. Electron. vol3 p288 (1974)

[9] F.F. Chen "Introduction to Plasma Physics " Plenum Press N.York (1977)

[10] V. F. Bunkin & A.M. Prokhorov , Usp. Fiz. Nauk , vol119 425 (1976)

[11] A.I. Barchukov , F.V.Bunkin , V.I.Konov & A.A. Lyubin , Sov. Phys. JEPT vol39 no3 pp469-477 (1974)

[12] P.S.P. Wei & R.B.Hall , J. Appl. Phys vol44 no5 (1973)

[13] A.A. Bakeev et. al. , Sov. J. Quant. Electron vol5 no6 (1975)

[14] S.A. Ramsden & P. Savic , Nature vol 203 pp1217-1219 (1964)

[15] Streak camera loaned from the Applied Physics Dept. Hull University .

[16] A.V. Bessarab , V.M. Romanov , V.A. Samylin & A.I. Funtikov , Sov. Phys Tech. Phys. vol23 no8 pp995-996 (1978)

[17] T. Zyung , H. Kim , J.C.Postlewaite & D.D. Dlott J. Appl. Phys vol65 no12 pp4548-4563 (1989)

[18] J.E. Lowder & L.C. Pettingill Appl. Phys. Lett. vol24 no4 pp204-207 (1974)

[19] J.F. Ready , Appl. Phys. Lett. vol25 no 10 pp558-560 (1974)

[20] A.N. Pirri , R.Schlier & D. Northham , Appl. Phys. Lett. vol21 no3 pp79-81 (1972)

[21] V.P. Ageev et al Izvestiya Vysshykh Uchebnykh Zavedenii , Fizika no11 pp34-60 (1977)

[22] A.N. Pirri , J. Fluids vol 16 p1435 (1973)

[23]Edwards , Lawrence Livermore Laboratory , Report No UCRL 51489
[24]R.E. Beverly III & C.T. Walters , J. Appl. Phys. vol47 no8 (1976)
[25]D.C.Emmony R.P.Howson & L.J. Willis , Appl. Phys. Lett vol23 no11 pp598-600 (1973)

Chapter 4

Properties of the Plasma Ultrasonic Source

4.1 Introduction

The CO_2 laser has previously been used to generate ultrasound in liquids such as water [1] , due to its strong infrared absorption generating both thermoelastic and ablative , ultrasonic waves . However information specifically regarding acoustic generation in solids , especially metals , is very scarce despite the knowledge of the impulses delivered to a target from a laser supported plasma .

A.A. Karabutov et. al. [2] used the thermoelastic interaction between 10.6 μm radiation and various metals to monitor the reflectivity of metallic mirrors . The authors developed a one dimensional model of the interaction which stated that the ultrasound amplitude varied linearly as a function of both incident energy and mirror reflectivity . The validity of the one dimensional approach , which was based on an unfocused radiation source of cross section 4 cm^2 , was born out by results for the reflectivities of a range of metals being within ~±3 % of more traditionally favoured techniques for measuring the same quantity . As will be shown in chapter 6 , source dimensions below this size will generate shear waves and a purely one dimensional approach is no longer strictly valid . The ultrasound will still vary linearly as a function of surface reflectivity but unless an exact description of the ultrasonic wave equation in known this will only give relative and not absolute measurements .

N.E. Aver'yanov [3] used a CO_2 laser to investigate the surface quality of metal reflectors . Using the work of Walters [2.6] , who stated that low threshold breakdown may be initiated by thermally uncoupled surface defects , the authors irradiated targets with 10.6 μm radiation at power densities of the order 10^7 Wcm^{-2} . The presence or not of a low threshold plasma above the sample was thus an indication of surface defects . The presence of a plasma

was found to give rise to an ultrasonic signal with opposite polarity to that produced by a thermoelastic interaction . Aver'yanov et. al. however made no characterization of the ultrasonic signals obtained and simply relied on the on-off nature of the plasma to give direct information on the surface quality .

A more detailed study of CO_2 radiation interacting with metals was undertaken by Wang et. al. [4] , who used a generating laser pulse that was similar to the one used in the work reported here . The authors studied the frequency spectra of the longitudinal and shear transients and also the amplitude variation as a function of incident laser energy . However despite acknowledgement that large ultrasonic signals may be obtained from plasma sources the authors restricted their investigation to the thermoelastic generation mechanism . As previously measured by Aver'yanov [3] , Wang [4] measured the linear increase in acoustic displacement as a function of increasing input energy . To measure the acoustic frequency spectrum a series of cross calibrated PZT transducers , of varying centre frequency from 1 -10 MHz , were used to record the ultrasonic amplitude . The spectrum obtained showed a frequency envelope typical of the fourier transform of a finite duration delta pulse , but with a small amplitude peak at ~5MHz with a large peak occuring at ~8.5 MHz , before the envelope tailed off rapidly to zero at ~10MHz . This result does not agree with previous frequency spectra studies of laser generated transients or the work presented here and appears to be a calibration error .

The purpose of this chapter is to examine the properties of the laser supported plasma as an ultrasonic source . The interaction is studied by observing the shape and amplitude of on-epicentre and surface ultrasonic transients as a function of power density , surface quality and laser pulse shape . These measurements , are where possible , compared to theory describing broadband ultrasonic transients in elastic media , and the experimental findings reported in chapter 3 . Unless otherwise stated this

work and that in subsequent chapters employs a reduced nitrogen laser gas mixture . As breakdown may only be initiated on the leading edge of the laser pulse [5] the presence of the low power nitrogen tail plays no part in the initial ultrasonic generation process . Thus the reduced laser gas mix produces a pulse similar in form to that of a conventional Q-switched laser pulse .

4.2 Epicentral & Surface Waveforms

If as a first approximation , we consider the plasma to exert a point , normal force onto the sample surface as described by the stress profile

$$\tau_{zz} = Z\,\delta(x)\,\delta(y)\,H(t-t_o)$$
$$\tau_{zr} = 0 \qquad 4.1$$

where δ is the Dirac delta function, Z the source strength and H a Heaviside time function then the resultant epicentral and surface displacement waveforms may be described by Knopoff's [6] and Pekeris's [7] solutions respectively .

This approximation assumes that the plasma interacts with the sample surface for times longer than the ultrasonic generation time , ~ 500ns . This is obviously not the case , as seen from the streak camera measurements shown in Fig 3.11 for the laser detonated wave , but is a good approximation for the laser plasmotron source. Fig 4.1a shows the epicentral displacement, W(T), produced by a source described by eq 4.1 . The form of the solution is given below

$$W(T) = \frac{Z}{\pi\mu z}\left(\frac{T^2\,(2T^2-2R^2+1)^2\;H(T-R)}{((2T^2-2R^2+1)^2 - 4T(T^2-R^2)\,(T^2-R^2+1)^{1/2})^2}\right)$$

$$- \frac{Z}{\pi\mu z}\left(\frac{4T^2(T^2-1)\,(2T^2-2R^2-1)^2\;H(T-1)}{((2T^2-1)^2 - 4T(T^2-1)\,(T^2-R^2+1)^{1/2})^2}\right) \qquad 4.2$$

Where $T=v_s t/R$ and $R=v_s/v_p$ and t the time and μ is a Lame constant. The form of the solution shows the wave to comprise of a longitudinal arrival , shown in Fig 4.1a as (P) , characterized by an initial outward displacing step which then continues to increase gradually with time until the arrival of the shear wave , shown as (S) .The shear arrival is marked simply by a change in the gradient of the continued outward displacement . The shear wave is observed by its longitudinally displacing polarized component which is of much lower intensity than the in-plane wave component . Fig4.1b shows Knopoff's solution convolved with a Heaviside stress function having a risetime of 50 ns . The result of this convolution is to give a finite gradient to the initial longitudinal arrival and to slightly decrease the gradient marking the shear arrival .

Fig 4.2 a shows the surface outward displacement for such a source distribution , which may be described mathematically as

$$W(T) = 0 \qquad t < 1/\sqrt{3}$$

$$+\frac{Z}{32\pi\mu r}\left(6 - \frac{\sqrt{3}}{(\tau^2 - 1/4)^{1/2}} - \frac{(3\sqrt{3}+5)^{1/2}}{(3/4+\sqrt{3}/4-\tau)^{1/2}} + \frac{(3\sqrt{3}-5)^{1/2}}{(\tau^2+\sqrt{3}/4-3/4)^{1/2}}\right) \qquad 1/\sqrt{3} < \tau < 1$$

$$+\frac{Z}{16\pi\mu r}\left(6 - \frac{(3\sqrt{3}+5)^{1/2}}{(3/4+\sqrt{3}/4-\tau)^{1/2}}\right) \qquad 1 < \tau < \frac{(3+\sqrt{3})^{1/2}}{2}$$

$$-\frac{3Z}{8\pi\mu r} \qquad \tau > \frac{(3+\sqrt{3})^{1/2}}{2} \qquad 4.3$$

Where $T=v_s t/r$, r being the source to receiver separation . The first arrival originates from a surface skimming longitudinal wave . The shear wave arrival is marked by an outward displacing motion which tends to infinity at

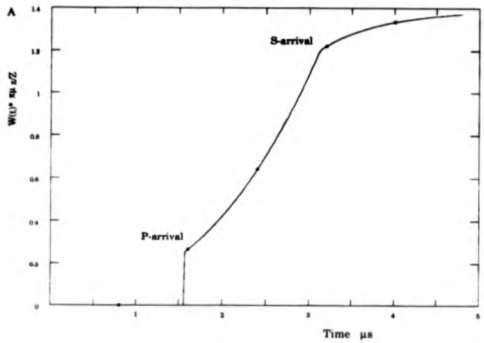

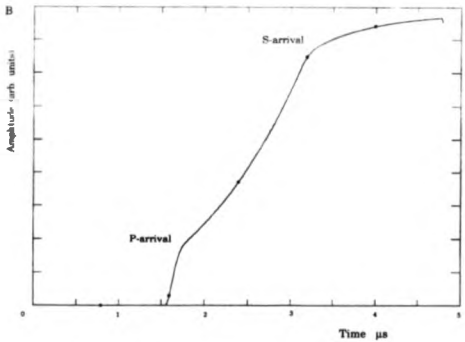

Fig 4.1a: Knopoff's displacement solution for a point , normal force .
b: Point source solution convolved with a 50ns temporal source function .

the Rayleigh wave arrival , after which the surface is displaced inwards by a constant value . The solution is calculated for simplicity by setting the Lame constants , λ and μ , to be equal thus fixing the ratio of the shear and longitudinal velocities as $V_p^2=3V_s^2$. Therefore the relative longitudinal to shear wave positions are different to those observed on most metals , however the basic structure of the displacement is the same as that observed experimentally . Fig 4.2b shows Pekeris's solution convolved with the same 50 ns risetime stress profile used to produce Fig 4.1b . The infinity at the Rayleigh arrival is lost and the ratio of the longitudinal to Rayleigh arrival amplitudes is increased as well as the duration of the Rayleigh arrival .

As the streak camera measurements reveal , the L D W source rapidly becomes detached from the surface of the irradiated target . This suggests that the surface stress profile may be approximated to a delta function duration relating to the time the plasma stays in contact with the sample surface . The effect of such a change in the source distribution would be to differentiate the displacement waveforms predicted by Knopoff and Pekeris with respect to time , the results of which are shown in Fig 4.3a&b respectively

The epicentral displacement waveform is now characterized by a monopolar longitudinal arrival followed by a shear arrival which charges the polarity of the displacement direction from positive to negative . The surface Rayleigh wave becomes bipolar in nature upon differentiation .

This change in the characteristic waveforms predicted under the action of a L D W source may be seen as the limiting case for the two plasma ultrasonic sources . The detachment of the plasma shown in the streak camera measurements shows only the motion of the luminous plasma and not the time history of the shock wave produced by the plasma . The L D W will generate pressure waves continually as it moves towards the laser , thus the target will be continually subjected to shock waves , but due to the motion of their origin away from the target surface their intensity will decrease rapidly .

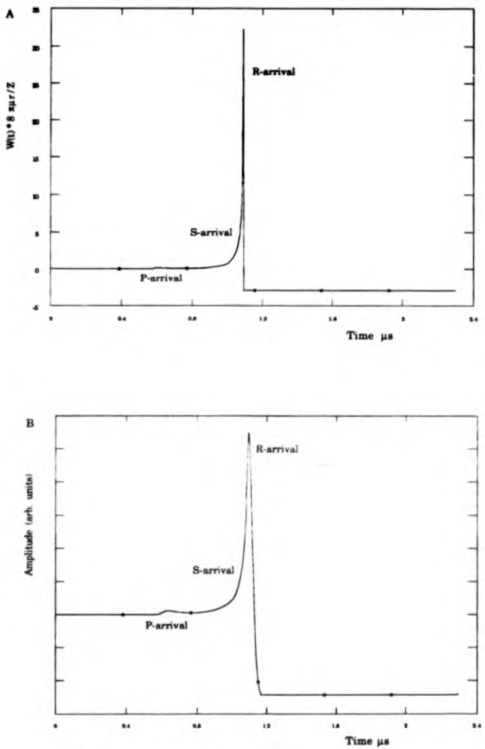

Fig 4.2 a: Pekeris' point source solution for the surface displacement derived from a normal force .
b: Point source soultion convolved with a 50ns risetime temporal source function

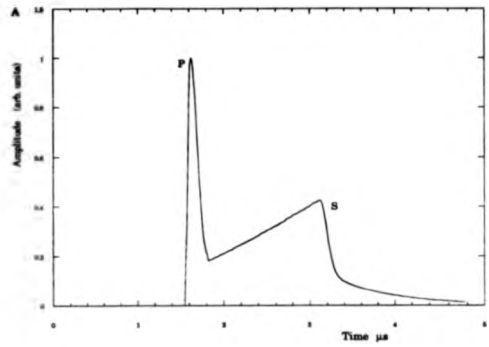

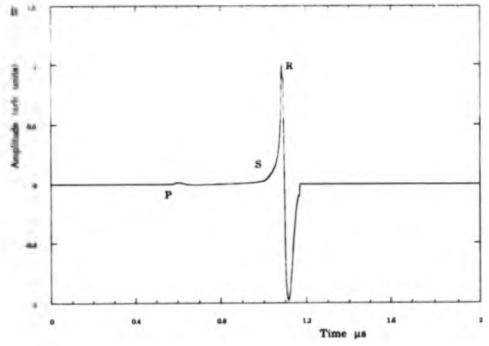

Fig 4.3 a & b Time derivatives of Knopoffs and Pekeris' solution representing the surface displacements produced by impulsive source functions

4.3 Experimentally recorded waveforms .

4.3.1 Bulk waves

A series of ultrasonic waveforms , detected interferometrically employing the general experimental arrangement shown in Fig 4.4 , were recorded on a 10mm thick aluminium sample , one side of which was polished to a near mirror finish to enable detection , while the other side , on which the plasma was generated had a slightly better than machined finish . The alignment of the plasma source and the interferometer , required for accurate detection of on-epicenter bulk waves , was made visually using the visible emission associated with the plasma . The digital , 10ns sampling rate , "Lecroy 9400" oscilloscope was triggered by means of a signal taken from the lasers electronic discharge pulse . This produces a signal which occured ~1μs before the emission of the radiation . The jitter on this trigger is less than ±2ns from shot to shot and thus gave sufficient stability from which accurate timing measurements were made .

Fig 4.5 shows an epicentral waveform detected with a L P source . Comparison with Fig 4.1a shows a very good agreement between this rather complex source and the simplified stress profile required for Knopoff's solution , although it differs in two respects . Firstly a plateau is observed after the initial longitudinal step and secondly the post shear arrival sees an inward displacing motion as opposed to the continuation of the outward displacement predicted by Knopoff . These observations are characteristic of a temporal stress function which is not totally Heaviside in nature but decreases in amplitude shortly after its initial onset . This suggests that the either the duration and energy of the laser pulse is too low to provide a total Heaviside type force at the sample or that the plasma becomes overdense and shields the sample surface from the incoming laser radiation .

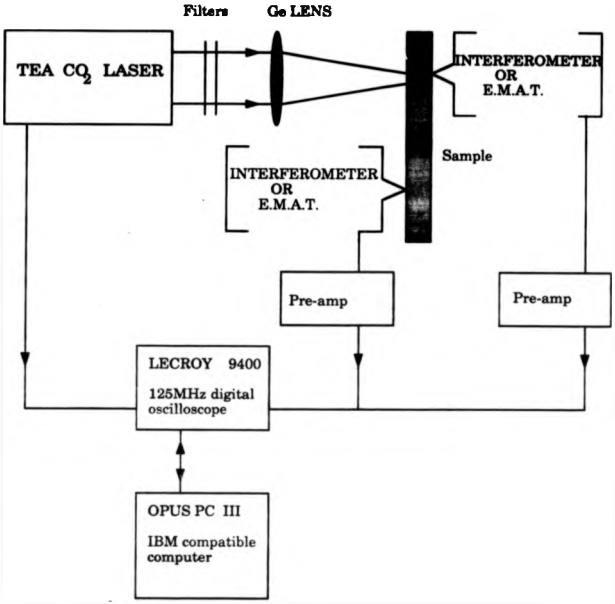

FIG 4.4

General experimental arrangement for the generation and detection of bulk and surface ultrasonic waves .

Fig 4.6 shows the corresponding waveform to that in Fig 4.5 but produced under the action of a L D W plasma source . Here the longitudinal arrival is marked by a monopolar pulse after which the surface continues to displace outward until the arrival of the shear wave . Comparison with Fig 4.3 shows a distinct similarity between the two waveforms . Thus as predicted the shielding of the surface by the plasma produces only a very short lived impulse at the sample surface , which may validly be modelled as delivering an impulsive force at the surface . As shown by Dewhurst et. al. [8] the acoustic wave generated may vary in shape between the two extremes of Fig4.1a&b and Fig4.3 as the source varies from a Heaviside to a delta type time dependence and hence as the plasma source varies from a LP to a LDW type motion .

4.3.2 Surface Waves

The distinct difference predicted in source characteristics between the LP and LDW sources is born out again when studying the surface waves . Fig 4.7 shows a L P generated surface wave , which is in close agreement with Pekeris's solution (Fig 4.2) . The surface is seen to stay suppressed after the monopolar Rayleigh wave arrival . This contrasts strongly with the ultrasonic waveform generated by a LDW (Fig4.6) . Once again direct comparison may be made between this waveform and Fig 4.4 , the time differential of Pekeris's solution , which yields a bipolar Rayleigh wave .

The form of these equations allows the impulse delivered to the target by the plasma source to be calculated . From Knopoff's solution the surface displacement of the initial longitudinal arrival is related to the impulse by

$$W(Tp) = \frac{Z}{8\pi\mu z} \qquad 4.4$$

A surface displacement of 10nm on a sample of 10mm thickness is typical of the ultrasonic displacement produced by the plasma . Using a value of $\mu = 2.6 \times 10^{10}$ Pa for aluminium for eq. 4.4 gives a surface force of ~ 65.3 N ,

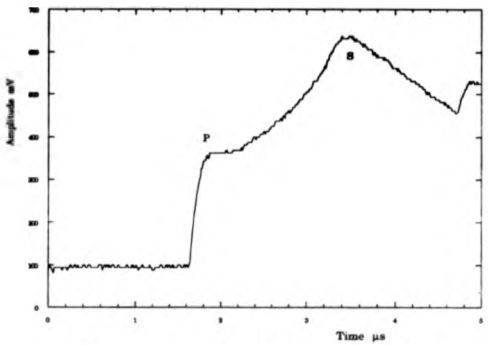

Fig 4.5 Epicentral displacement generated under the action of a L.P. plasma source.

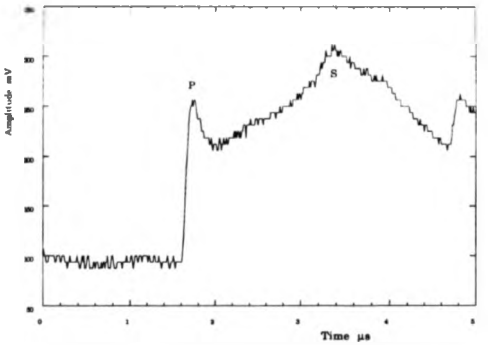

Fig 4.6 Epicentral displacement generated under the action of a L.D.W. plasma source.

corresponding to an impulse of 6.5 dyne-sec . We chose taken here the streak camera of 10^{-6} s for the plasma duration (an order of magnitude longer than the laser pulse)

Pekeris's solution may also be used for impulse estimation by considering the post Rayleigh arrival , surface displacement . This value is the most suitable for analysis as unlike the Rayleigh wave peak displacement it does not depend on the source duration and is given in terms of the surface force by

$$W = \frac{3Z}{8\pi\mu r} \qquad 4.5$$

which using the experimental waveform of Fig 4.7 gives an impulse of 57 N for a source - receiver separation of 100mm and a displacement of 3nm . These values agree well with those discussed in chapter 3 . The previous analysis measures the impulse over the entire duration of the plasma , being when the shock pressure equals atmospheric . It is correct to consider the initial impulse to be generated only over the risetime of the ultrasonic wave and not over the entire duration of the plasma . This increases the value of the impulse by an order of magnitude as the ultrasonic risetimes , as discussed in the next section , are approximately 100 ns . The distinct change in source strength between L P and L D W indicates that the main ultrasonic interaction originates predominantly from the initial plasma - sample coupling while subsequent plasma growth and motion plays little role in the generation of ultrasonic transients .

4.4 The Ultrasonic Frequency Spectrum

The frequency content of the ultrasound generated is of importance as it limits the interactions which may occur with the internal structure of the sample under inspection . In terms of an N.D.T. setting the minimum

detectable defect size detectable is of the order of the minimum ultrasonic wavelength . Thus the ability to generate high frequency ultrasound is of great importance in the detection of flaws and defects in materials .

Two methods of examining the frequency content of the CO_2 laser generated ultrasound have been employed :- fast fourier transforming and risetime measurements . The fast fourier transform (FFT) technique suffers from the comparatively low (10 ns) sampling rate which is the limit of the Lecroy 9400 digitizer and also the presence of digital noise generated by the pre-amplification and the oscilloscope . Fig 4.9 shows an averaged FFT obtained a direct ,EMAT longitudinal wave showing the frequency envelope extending up to ~4 MHz . The peaks in the spectra are artifacts of the low sampling . Fig 4.9 may be compared with the FFT of the laser pulse shown in Fig 3.2 which shows the frequency spectrum of the laser pulse to extend up to ~10 MHz , indicating that the ultrasonic generation is limited by the rate at which the plasma may be produced . This contrasts with the mechanism of ablation produced by the interaction of Nd:YAG laser radiation with targets in which the ultrasound is limited purely by the risetime of the laser pulse .

Due to the poor quality of the FFT data the above measurements were complemented by risetime measurements , which gave a higher accuracy in determining the maximum frequency content . The risetime , R_t ,of the longitudinal arrival between the 10% - 90 % amplitude level is recorded and relates to the maximum frequency content , F_m , via the relationship

$$F_m = \frac{1}{\pi R_t} \qquad 4.6$$

The ultrasonic transients were recorded using an out-of-plane sensitive EMAT coupled to a wideband pre-amplifier . This detection system was tested for its bandwidth limitation by measuring an ultrasonic pulse generated by a 10ns , Nd:YAG source , detecting a risetime of 25ns thus having sufficient bandwidth to measure CO_2 risetimes .

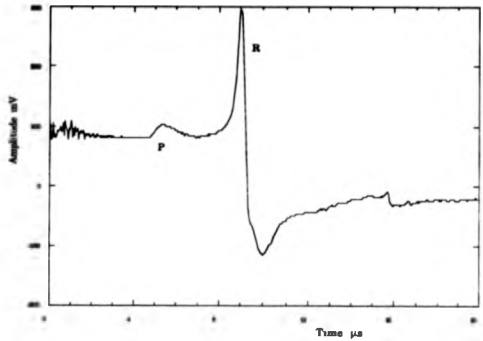

Fig 4.7 Surface duplacement waveform recorded under the action of a L.P. plasma source

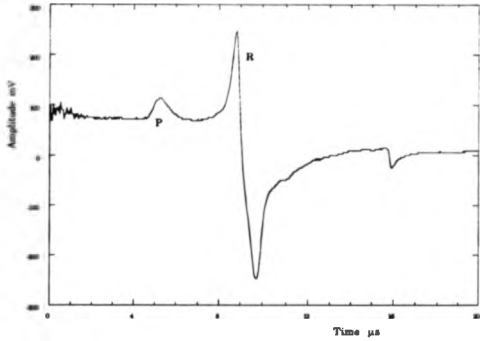

Fig 4.8 Surface displacement waveform generated under the action of a L.D.W plasma source

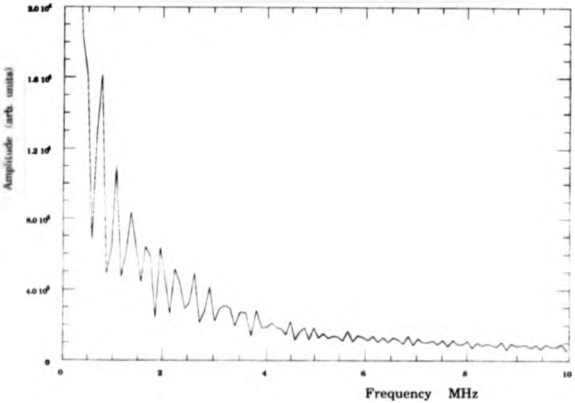

Fig 4.9 Fast Fourier transform of an EMAT detected longitudinal wave .

The detected ultrasonic risetime is a combination of the plasma risetime duration , τ , and the spread in ultrasonic arrival time , Δt , over the finite length of the detection coil , Thus the measured risetime , R_t , may be given as

$$R_t = \tau + \Delta t \qquad 4.7$$

and is shown in Fig 4.10 . The geometrical term may be calculated if a point source of spherically expanding waves is assumed . For a sample of thickness D and a detection coil of length 2L , Δt is the time between for the wave to reach the outer and central portions of the coil , given for the direct longitudinal wave by

$$\Delta t_p = \frac{\left((D^2+L^2)^{1/2} - D\right)}{Vp} \qquad 4.8$$

Where Vp is the longitudinal velocity . Using a binomial expansion on the power term and keeping only the first two terms gives

$$\Delta t_p = \frac{L^2}{2DVp} \qquad 4.9$$

Similarly if the 3P arrival is considered , as shown in Fig 4.10b , the geometrical spread may be calculated similarly as

$$\Delta t3_p = \frac{L^2}{6VpD} = \frac{\Delta t_p}{3} \qquad 4.10$$

Substituting these geometrical terms for the P and 3P waves arrivals into eq 4.5 and subtracting leaves a purely geometrical term $\Delta T = \Delta t_p - \Delta t3_p$,given by

$$\Delta T = \frac{L^2}{3DVp} \qquad 4.11$$

Therefore from the difference in risetimes of the first and second longitudinal arrivals the effective coil length may be calculated and the geometrical effect removed from the measurements . The risetimes of the P and 3P arrivals as a function of varying lens - sample separation are shown in Fig 4.11a and are

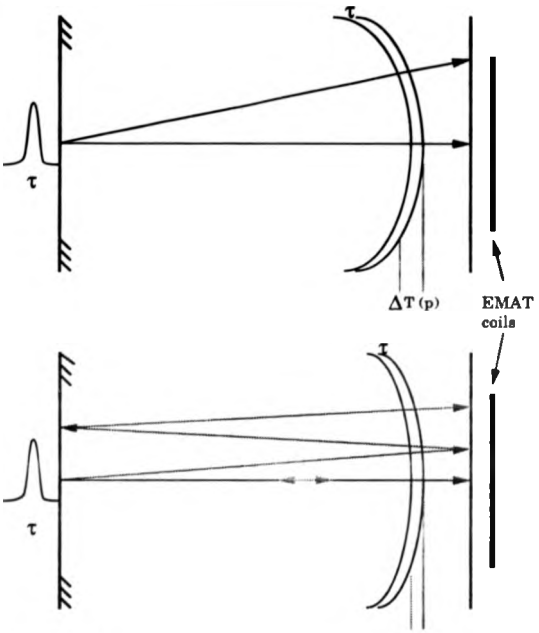

Fig 4.10

The change in ultrasonic wavefront curvature due to multiple reflections and hence the reduction in the spread in arrival times across the coil leading to a decrease in measured risetime .

shown to be symmetrical about the focus of the lens . The L D W source gives a much lower risetime than the L P source , by 12 - 15 ns . Using eq 4.10 yields a value of $\tau = T_p$ - 15ns and hence a maximum frequency content for the L D W of ~9 MHz while the L P source gives a frequency content of ~5.5 MHz . This trend may be expected due to the higher electron density and faster plasma growth produced by increased laser power densities .

To remove the effect of source size variations which may perturb the previous results , a series of measurements were taken at constant source size while the incident laser energy was varied by means of filtering . Fig 4.11b shows the risetime variation for two different lens-sample separations , one at 10.5cm separation which with no attenuation produces a L P source while the second set of data was recorded with a 9.5cm separation producing a well defined L D W source at full incident power . Both sets of data show the risetime to increase as the incident energy is decreased . The two graphs show that for incident power densities is well above the breakdown threshold the risetime stays approximately constant . As is discussed in the next section , the beam attenuation results in a change in the source character from a L D W to L P type plasmas . No distinct transition in the risetime is observed from one source type to the other , indicating that the ultrasonic risetime depends purely on the initial growth of the electron density . The 9.5 cm lens - sample separation data show the risetime to start increasing well before the corresponding point in the 10.5 cm separation data indicating once again that the risetime is purely a function of incident power density .

4.5 Amplitude variations of on-epicentre waves as a function of incident power density

As discussed in the previous section the power density may be varied either by changing the source dimensions or the incident energy . The source

size is simply controlled by variation of the lens - sample separation and gives information on the relative position sensitivity of the lens and sample with respect to the effective generation ability . The incident energy is varied by means of filtering . The filters used in this work are made of varying polymer films , such as ,mylar , melinex and polythene . The filters were calibrated using the photon drag detector which measured the transmitted levels of radiation . The variation in the shot to shot laser pulse energy of ~2% were accounted for by taking multiple measurements of the transmitted energy giving an accuracy of ~1% for the transmission coefficient . It must be noted however that the transmission coefficient of individual filters may vary over a large number of shots due to the absorption of radiation causing heating within the polymer resulting in a change to the structure or thickness of the filter .Regular recalibration of the filters is the only solution .

4.5.1 Source Size Variations

Fig 4.12 shows the variation in epicentral longitudinal surface displacement as a function of lens - sample variation recorded on an aluminium target . The lens-sample separation passes through the focal plane of the 9.5 cm focal length lens where the power density is at a maximum of 10^9 Wcm^{-2} . The graph shows a distinct symmetry about the focal plane of the lens . Below power densities of $3.3*10^7$ Wcm^{-2} corresponding to lens sample separations of 7.5cm and 11.5cm only a weak thermoelastic signal is observed , the features of which are discussed in chapter 6 . Increasing the power density slightly above the breakdown threshold yields a rapid rise in the ultrasonic amplitude corresponding to a well defined L P source . The two peaks in displacement amplitude correspond to a power density of $6.25*10^7$ Wcm^{-2} As the power density and hence the plasma electron concentration increases , a transition from a L P to a L D W sources is observed and is marked by a steep fall in the epicentral displacement , which reaches a minimum at the

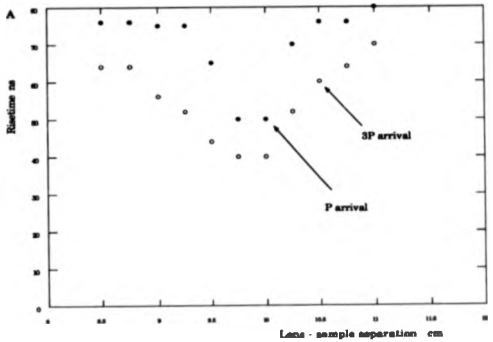

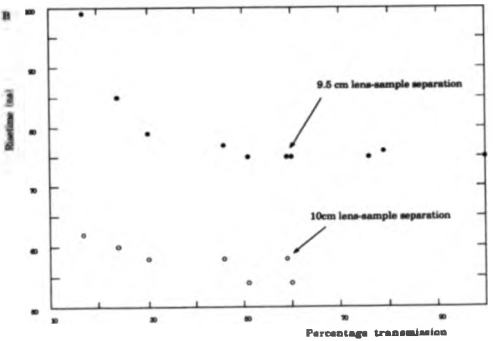

Fig 4.11a & b Longitudinal risetime variations as a function of source size and energy density respectively

maximum power density . A similar observation was made by Aindow [9] using a focused Nd:YAG laser source . For very tight focusing conditions the material vapour above the target is sufficiently dense to produce significant absorption of the incident radiation , resulting in a dramatic decrease in the ultrasonic amplitude . As eq 3.15 indicates , 1.06 μm radiation will penetrate a plasma to greater depths than 10.6 μm radiation and thus this effect is significantly lower than for CO_2 radiation .

The symmetry between the cases of the lens focusing before or after the target surface is however broken . Geometrically the two cases are identical if one considers a ray optics approach , as shown in Fig 4.13 . In this model the power density originating from the sum of the incident and reflected beam components , are totally symmetrical about the focal plane . However as shown by open symbols in Fig 4.12 the pre-focused case gives an additional or bistable behavior . This lower amplitude level corresponds to the presence of a well defined L D W being created under the same focusing conditions as the LP source resulting in the observed amplitude fluctuations . This behavior was also observed on stainless steel and brass (Fig 4.14 a & b) .

An explanation of this behavior may be that the power density of the radiation at the focal point is sufficient to produce a degree of multiphoton ionization creating a region of high electron concentration well above the target surface , as indicated in Fig 4.13a . Thus inverse Bremstrahlung absorption will occur both at the target and in the focal region of the lens . The resulting extended electron rich region may provide the correct conditions for the formation of a L D W to propagate . For the post focus case where the reflected beam may undergo absorption and scattering at the sample surface , the focal point power density will be less well defined and weaker than for pre-focusing . Thus the electron concentration within the focal volume will be significantly lower and the extended electron region is not generated and only a L P source may develop associated with the target surface .

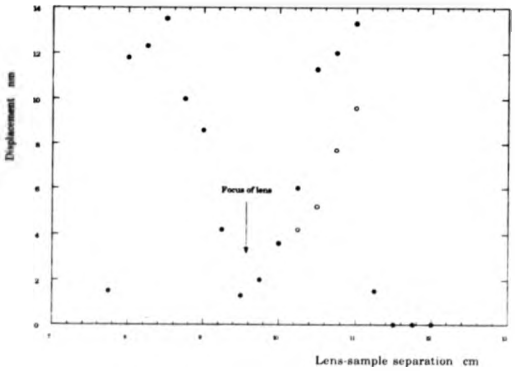

Fig 4.12 Variation in epicentral displacement produced by a plasma source as a function of lens-sample separation.

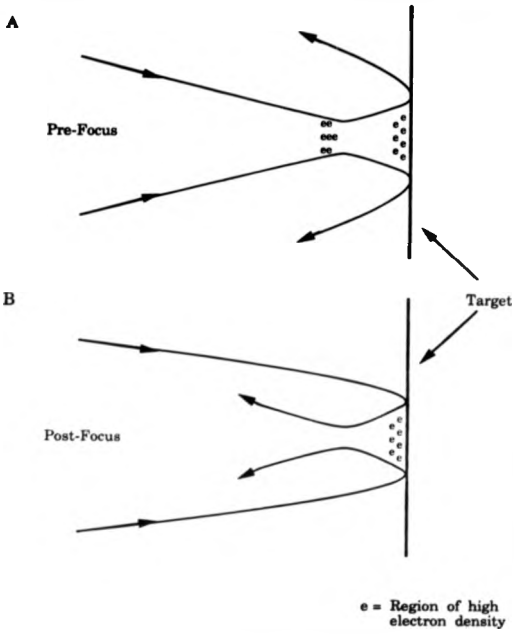

Fig 4.13

The geometrically identical ray-optic cases of pre and post focusing , with their regions of high electron density .

The graphs in Figs 4.12 and 4.14a&b can be used to determine the variation in breakdown threshold for the different materials . Comparison of the laser power density required to generate a 2nm epicentral displacement , for the three metals , gives the breakdown threshold for aluminium and stainless steel to be approximately $4.25*10^7$ Wcm^{-2} and Brass is a factor of ~1.1 less . These values lie well within the broad experimental measurements recorded by Ageev [3.21] Comparison of the displacement may also be made to give a possible insight into the generation mechanism . For plane and spherical waves the pressure , P , and particle displacement , u , are related by

$$P = Z' \upsilon u \qquad 4.12$$

where Z' is the acoustic impedance and υ the acoustic frequency . Thus a plasma source generated at a sample surface creates particle displacement in the air , u_{air}

$$u_{air} = \frac{P}{Z'_{air}\,\upsilon} \qquad 4.13$$

while in the metal the particle displacement , u_m ,may be similarly given as

$$u_m = \frac{P}{Z_m\,\upsilon} \qquad 4.14$$

Comparison of the displacement amplitude in two metals removes the necessity to have knowledge of the air dynamics , leading to the relation

$$\frac{u_{m1}}{u_{m2}} = \frac{Z'_{m2}}{Z'_{m1}} \qquad 4.15$$

which from the comparison of the respective acoustic impedances give the amplitude ratio of aluminium to stainless steel to be 2.72 while for aluminium and brass the ratio is 2.10 . The mean ratios for the ultrasonic displacement were determined from the individual ratios measured for each separate power density . This yielded values of 2.68±0.07 and 2.2±0.1 for the aluminium to

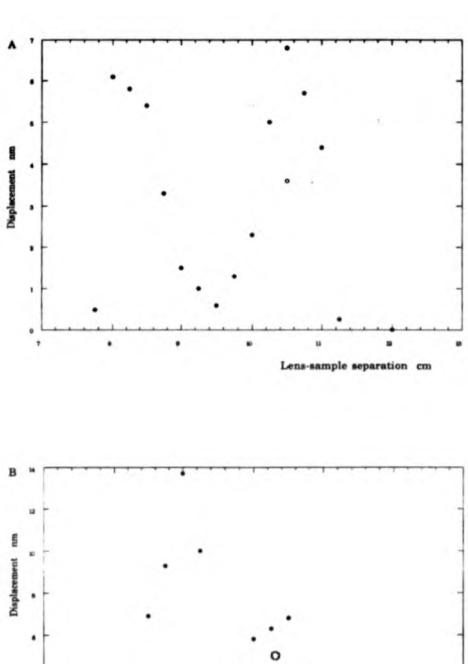

Fig 4.14 a& b Variation in ultrasonic epicentral displacement produced by a laser supported plasma for stainless steel and brass respectively .

stainless steel and aluminium to brass ratios respectively in agreement with the theoretical values calculated above showing again that the ultrasonic generation process originates almost purely from the plasma generated shock wave .

The breakdown process is however governed by many material properties and thus a standard , target independent source is not achievable . The properties effecting breakdown are : (i) the material - radiation absorptivity , which governs the sample heating , (ii) the boiling point , which will effect the temperature dependence of the absorptivity , (iii) the sample quality and smoothness and thus the number of defect sites for plasma initiation and (iv) the work function which is a measure of the ease of electron emission . The relative weighting of these individual factors in the generation efficiency of an ultrasonic wave is difficult to access theoretically due to the complexity of the breakdown process . However as the above results suggest , as long as plasma initiation occurs the amplitude of the ultrasonic source depends primarily on the acoustic impedance of the material under inspection

4.5.2 Incident radiation energy variations

The variation in ultrasonic amplitude , as a function of incident radiation energy was recorded over a range of source sizes . The results show a distinct difference in amplitude variation dependent on the initial plasma source . Fig 4.15a shows the decrease in measured ultrasonic amplitude as a result of beam attenuation from an initial L P source . The variation in ultrasonic amplitude is approximately linear above the power density required to produce a well defined L P source . This behavior is changed dramatically when the initial source is a L D W , as shown in Fig4.15b . The ultrasonic amplitude increases sharply as the beam is initially attenuated and the degree of plasma shielding of the target surface is reduced . Further beam

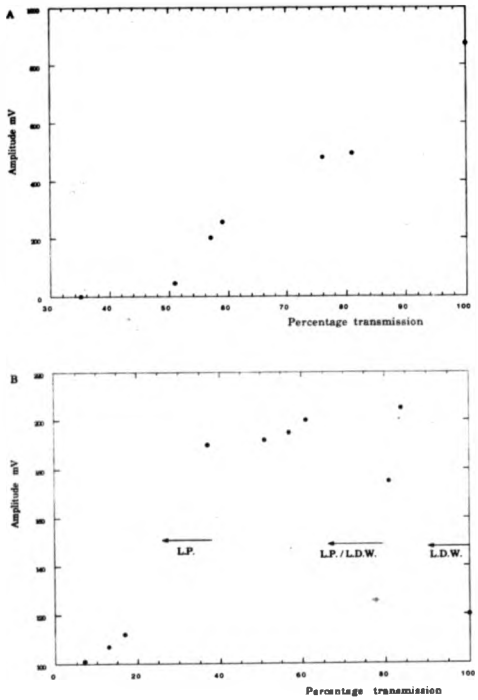

Fig 4.16 a & b Variation in measured ultrasonic amplitude as a function of beam attenuation , for unattenuated L.P. and L.D.W. sources respectively .

attenuation while the plasma is in the mixed state yields little change in the ultrasonic amplitude thus , in terms of the ultrasound amplitude per joule , the coupling of the plasma to the target is increased . At the point when a well defined L P source is reached the ultrasonic amplitude decreases (Fig 4.15a) .

From the work of Pirri [3.21] the pressure behind the blast wave increases as $E^{2/5}$, where E is the incident laser energy . Thus the resultant increase in obtained blast energy varies only weakly with increased incident energy and does not account for the observations made . The enhanced models of both Pirri [3.21] and Ageev [3.20] defining both spherical and cylindrical shock waves predict closely the relative change in impulse delivered by L P and L D W sources . The source strength variation in the measured displacements recorded for aluminium , stainless steel and brass give the displacement ratio between L P and L D W sources of 9 , 10 and 4.6 respectively . The theoretical ratios for the impulse per joule , taken from Ageev , delivered from the two source types is ~4.5 which increases to a value of 9 if the L P source has a large area and tends from spherical to plane wave in nature . The maximum impulse delivered by the spherical L P source varies linearly with incident energy which agrees with the observed trend in Fig. 4.15a . The theoretical variation in the impulse delivered by a L D W also depends linearly on the incident energy , however as previously discussed the source changes via a mixed state from the cylindrical model to the spherical model and can no longer be described accurately by either of the two limiting case .

Finally these results can be used to determine the effect of source size on the breakdown threshold . The breakdown threshold is determined as the incident power density required to produce a fixed ultrasonic amplitude , the results of which are shown in Fig 4.16 . The graph shows a rapid decrease in power density required to produce breakdown as the source diameter increases from 1mm to 2mm , where after the continued decrease levels off at ~5mm diameter ; this behavior having been noted previously [10] . For smaller

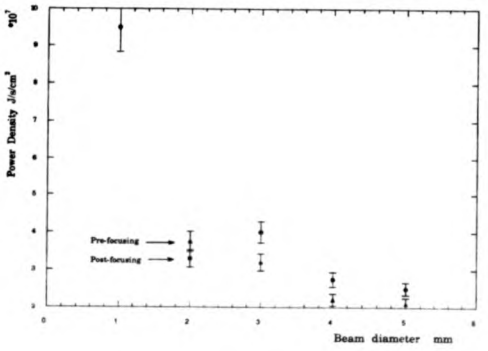

Fig 4.16 Variation in plasma breakdown threshold as a function of beam cross section .

plasma volumes and hence high electron concentrations the number of elastic collisions between electrons increases , as well as the rate of electron loss from the pre-plasma volume . As the source volume increases the losses are reduced as the surface area does not grow as quickly as the volume of the source . Secondly the electron concentration is reduced with respect to the number of atoms and molecules hence reduces the frequency of elastic electron - electron collisions .

4.6 Surface Quality and the role of Oxide Layers

4.6.1 Surface Quality

The effects of surface quality on the generation efficiency of thermoelastic Nd:YAG generation were investigated by Aindow [9] . The ultrasound produced showed a slight textural dependence , the origin of which may lie in the fact that as the irradiated material expands the unevenness of the surface may give rise to forces directed normally into the bulk of the material . The ablation regime , due to the violence of the reaction , shows no textural dependence .

Similar measurements were undertaken with the CO_2 laser working in the plasma regime to study the degree to which the surface quality governs the generation process . Surfaces were roughened , using Carborundum abrasives , to give a range of textures from 50μm down to a mirror quality target surface . Above a surface roughness of 1μm no difference in breakdown threshold or ultrasonic amplitude was observed . Below 1μm surface flatness the breakdown threshold rose sharply to a degree where breakdown is suppressed totally . This degree of surface quality ensures that the number of potential breakdown initiation sites , especially flake type defects , is greatly reduced . Air breakdown was observed to occur at the focal point of the lens , seeded either by air impurities or thermal electrons emitted from the target .

The air blast produced a very weak ultrasonic source even with the focus of the lens just above the target , giving rise to surface displacements of ~0.5nm , an order of magnitude lower than surface generated plasmas .

Thus as long as the target material is not polished to a mirror finish , initiation of the plasmas occurs at the material surface producing large ultrasonic signals . With a surface roughness above ~1μm , where there are sufficient number of initiation sites , no ultrasonic amplitude variation was observed as the target only provides the initial electron concentration from which breakdown is initiated and plays no further role in the generation process .

4.6.2 Surface Oxides

As discussed in chapter 2 surface oxides act in a similar fashion to other surface modifying layers in that they provide a highly absorbing layer which is rapidly vapourized by the incident radiation . The recoil of the ejected material into the target produces the ultrasonic transients . The presence of surface oxides should play an important role in determining the breakdown threshold when generating plasmas above irradiated targets. Oxides have lower work functions than bulk metals and their absorption of 10.6μm is much larger than metals , hence thermoelectrons generation from oxide layers is theoretically easier than for clean metal surfaces . In the literature to-date only qualitative measurements of the degree of threshold lowering by surface oxides has been made . Ageev et. al. [3.21] were unable to measure the threshold level difference between oxide and clean metal surfaces , while Barchakov [3.11] reported the threshold to be lowered by a factor of ~7 from a clean target threshold level of $7 \cdot 10^7$ Wcm^{-2} .

An EMAT was used to record the amplitude of on-epicenter ultrasonic signals produced on targets with oxide layers . The breakdown threshold was determined to be the power density required to produce a fixed amplitude

signal . This technique therefore gives a direct measure of the effect of surface oxides . The power density was varied by varying the focusing conditions , as only slight focal variations were required in these measurements . Variation of the laser energy would be a more accurate method of varying the power density , although the poor range of filter variations available made this impossible . Non-polished samples of aluminium and copper which had been previously cleaned were uniformly heated in air to a temperature of ~1500 C to produce a degree of surface oxidation . As the atmosphere was not controlled the surface will also have impurities , such as hydrocarbons , absorbed onto it .

The measured thresholds recorded for aluminium and copper were determined with and without surface contaminants . The threshold on aluminium was found to be reduced by a factor of 1.35 from the clean surface threshold of $3.5 \cdot 10^7$ Wcm^{-2} and by a factor of 1.25 on copper from a pure metal level of $3.9 \cdot 10^7$ Wcm^{-2} . Thus a significant lowering in the required power density is observed in both cases . An approximate upper limit to the degree of threshold lowering can be determined using the work of Ageev [3.21] presented in chapter 3 , who determined the required incident power density to produce breakdown in a gas when differing materials were irradiated . Inspection of eq. 3.13 shows the threshold to be governed by the mean ionization energy or work function Δ^* and the mean atomic weight ,A^*, of the irradiated target material as

$$S \propto \frac{\Delta^*}{A^*} \qquad 4.16$$

The work function for copper is ~4eV while for copper oxide this is reduced to ~1eV . The atomic weights of the two are such as to result in a lowering of the oxide over that of the metal threshold levels by a factor of 2 . As pure substances (metal and oxide) were considered this is an upper limit in the degree of breakdown suppression . For partially oxidized targets , regions of pure metal and oxide will be simultaneously irradiated and thus the mean work function and atomic weight will correspondingly vary . The variation

may be observed by measuring the ultrasonic amplitude as a function of the number of times irradiated . On each pulse a small amount of oxide will be evaporated and removed from the target . Therefore the relative amount of oxide to metal will fall and the breakdown threshold will increase , resulting a reduction in the measured ultrasonic amplitude . Fig 4.17a shows this trend for three different irradiation sites on an aluminium target , while Fig 4.17b gives corresponding data recorded on copper . The ultrasonic amplitude falls continuously with the number of times irradiated material The aluminium oxide is removed quicker than the copper oxide which may be due to a lower percentage of oxide present or to a higher degree of evaporation than for the copper oxide . Since the evaporation of the oxide is relatively low per pulse it does not lead to a significant impulsive contribution to the ultrasonic transients produced , hence the source temporal profile is not altered as in the case of surface modified , Nd:YAG irradiated sources . The very high suppression of the breakdown threshold reported by Barchukov [3.11] may be accounted for by the possible absorption of hydrocarbons onto the surface of the samples and also the fact that the targets were of mirror quality which , as shown , increases considerably the power density required for breakdown .

4.7 Effects of the Nitrogen Tail

As discussed in chapter 3 , the presence of the nitrogen in the gas adds a low power tail , of duration ~ 1.5 -2 μs , to the initial laser spike which is also enhanced in energy by ~10% . The streak camera pictures , Fig 3.10 & 3.11 , show that the low power tail increases the duration of the laser supported detonation . In the L D W regime the coupling of the plasma to the target surface is the same as for the case of the reduced nitrogen gas mix . However the subsequent motion away from the sample is increased due to the longer

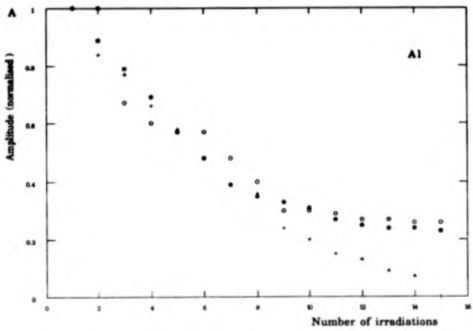

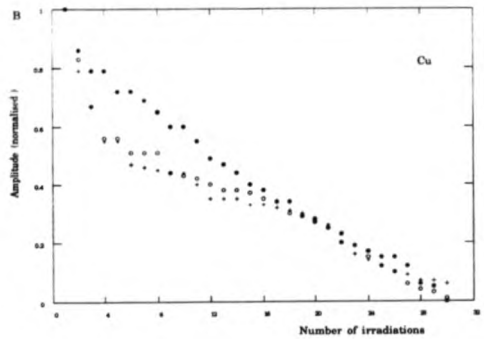

Fig 4.17 a & b The decay in the ultrasonic amplitude as a function of the number of times irradiated measured on aluminium and copper , resulting from the loss of the oxide layer .

laser pulse duration . This enhanced motion of the plasma plays no role in the initial ultrasonic generation and the waveforms recorded are directly comparable to those recorded with a reduced nitrogen gas mix . The ultrasonic signals generated under the action of a L P are however effected by the presence of the nitrogen tail . As the plasma is effectively transparent to the incident radiation , it is continually being regenerated next to the sample surface . Thus the condition of a Heaviside force function at the sample surface is met more fully than for the short pulse duration of the reduced gas mix . Fig 4.18b shows an on-epicentre bulk wave , equivalent to Fig 4.5 , recorded with the nitrogen gas mix . The structure of the surface displacement is very similar to that predicted by Knopoff as shown in Fig 4.1 . The increased duration of the plasma ensures that the displacement is continually positive in direction and the shear wave is seen to be a change in gradient as opposed to a change in polarity as observed when generated with the reduced nitrogen mix.

The analysis of an increased surface pressure duration for L P sources and an unchanged L D W source is however too gross a simplification to explain the phenomena observed from a nitrogen enhanced a source . Fig 4.18b shows an on-epicentre waveform recorded under the action of a well developed L D W source , showing the form of the displacement to contrast strongly with those produced by reduced gas mix L P and L D W sources . The rise in the displacement after the initial longitudinal arrival does not follow that predicted by Knopoff , and secondly the shear wave arrival in not detected . Such behavior may only be explained if the source function is one which continues to rise after the initial Heaviside step . To investigate such behavior further , interferometric studies of surface waves and EMAT studies of bulk longitudinal and shear waves were recorded . The EMAT was chosen as a detector of bulk waves as it differentiates the displacement waveforms ,

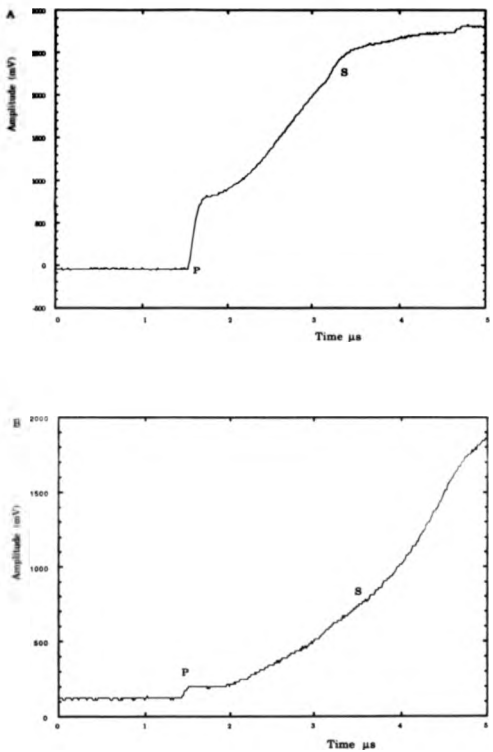

Fig 4.18 Epicentral displacements recorded on an aluminium sample under the action of nitrogen tail assisted L.P. and L.D.W. plasmas.

making it particularly sensitive to changes in gradient revealing greater structure in the ultrasonic signals .

Fig 4.19 shows a series of interferometrically recorded surface waveforms . Waveform (a) shows good agreement with that shown in Fig 4.7 and Pekeris's theoretical solution given in Fig 4.2 , differing only in its width . This broadening which is not simply a source size effect , is seen to change with focusing to become a distinct second feature . The series of waveforms shows this second feature to have a spread of arrivals ranging from nanoseconds to microseconds . Fig 4.20 gives a series of on-epicentre bulk waves detected with an out-of-plane sensitive EMAT . Once again a similar behavior is observed to that of the surface waves . The second feature is seen not only to move relative to the initial longitudinal wave but also vary considerably in amplitude . The timing of the second feature makes it longitudinal in nature , produced some time after the initial wavefront . Further measurements of off-epicentre shear waves gives corresponding behavior of a second shear wave generated at a variable time after the initial wave .

The form of the second feature has a bipolar nature although comparison of the longitudinal and Rayleigh wave data reveals that the exact form of the second feature varies between the two . Timing measurements on the duration of the second feature shows its frequency content to be lower than that of the initial ultrasonic waves by approximately an order of magnitude . The bipolar nature of the second feature suggest that the source function consists of an initial Heaviside source function , as required by Knopoff and Pekeris followed , later , by a broad monopolar force function superimposed on the initial Heaviside function .

To demonstrate this theoretically , the surface and bulk waves have been convolved with a source function consisting of the two components described above giving a source function , F(t) , presented in the form required for the

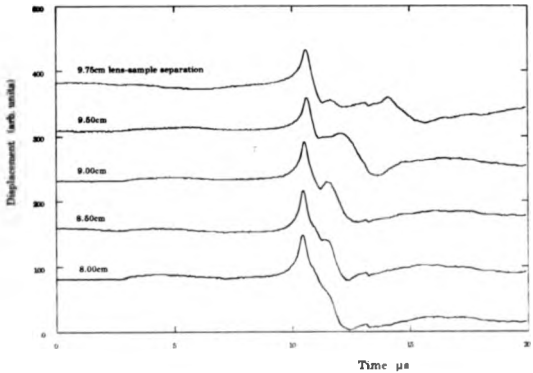

Fig 4.19 A series of Rayleigh waves generated by nitrogen tail assisted plasmas , showing the relative position and amplitude of the **secondary pulse** .

time domain convolution algorithm , being the differential of the true force function as expressed by

$$F(t) = \begin{matrix} \exp(-\alpha^2(t-\tau_0)^2) \\ + W_1(\tau_1-t)\exp(-\beta^2(t-\tau_1)^2) \\ + W_2(\tau_1-t)\exp(-\gamma^2(t-\tau_1)^2) \end{matrix} \qquad 4.17$$

where α , β and γ are inversely proportional to the rise and fall of the individual ultrasonic pulses , W_1 and W_2 are weighting functions relative to the initial Gaussian amplitude and τ_0 and τ_1 are the times corresponding to the centre of the two pulses . Fig 4.21a&b shows Rayleigh waves convolved with such a function with pulse separations of 400 ns and 1000 ns respectively , the relative source functions being shown on each graph . The waveforms agrees closely with those in Fig 4.19 and predict the relative amplitude and duration of the two pulse components . The convolution was repeated on Knopoff's displacement solution using the same source function employed on Fig4.21b , having a pulse separation of 1000 ns , the result of which is shown in Fig 4.22 . This gives a close comparison with the interferometrically recorded waveform shown in Fig 4.18 , showing the distortion of the purely Heaviside produced waveform and the loss of distinction in the shear arrival .

Differentiation of this theoretical waveform to model the EMAT recorded waveforms gives poor agreement with the experimental results shown in Fig 4.20 , particularly in that the gradient does not become negative in the region of the second pulse . To determine the sensitivity of the convolution process to the source function the convolution was repeated using a source function having an increased fall in surface pressure after the maximum of the second pulse . The new source function and the differentiated displacement waveforms are shown in Fig 4.23a & b . The rapid decrease in surface pressure does generate a negative going tail to the second pulse , however the overall waveform structure agrees poorly with experiment . Some degree of frequency loss ,

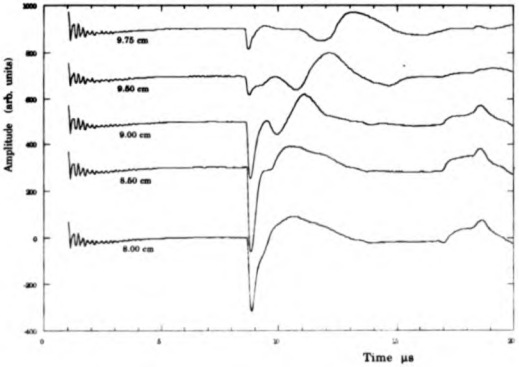

Fig 4.20 Longitudinal wave arrivals , for various lens-sample separations , generated with the nitrogen gas mixture , laser pulse

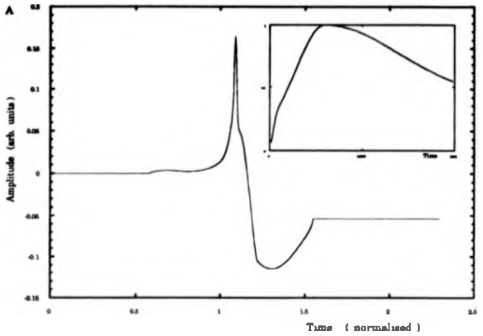

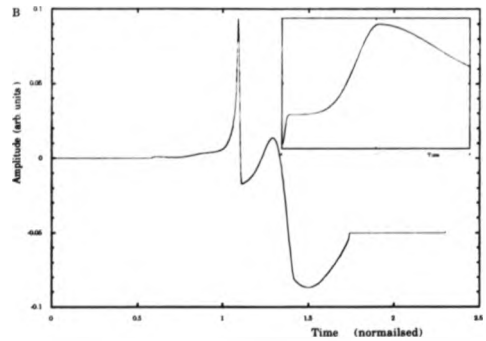

Fig 4.21 a& b Results of the convolution of Pekeris' surface wave solution with double pulse source functions , shown as insets , for pulse separations of 400ns and 1000ns respectively .

resulting the smoothing of the experimental waves is expected from the finite bandwidth of the detection EMAT , however this does not account for the discrepancy between experiment and theory .

For a further insight into the origin of the second waves a plot of the pulse separation from their peak positions , as a function of lens sample separation is presented in Fig 4.24a . The graph shows a scan of relative lens - sample separations , starting with the focal plane behind the target surface and moving back to eventually become pre-focused . Comparison of this graph with that in Fig 4.11 shows the range of power densities able to generate breakdown is extended , which is simply due to the slightly enhanced energy in the nitrogen gas mix laser pulse and is not a double pulse phenomena . Initially , as seen from in Figs 4.19 and 4.20 , the pulse separation is non-resolvable . As the focal plane is scanned back towards the surface the wave separation increases . The transition from a L P source to a L D W source sees a continual increase in the pulse separation , which reaches a maximum at the focal length of the lens corresponding to the existence of a well developed L D W . The pulse separation then falls rapidly to zero , or a level where the pulses are again unresolvable , corresponding to only a slight movement of the lens position . This transition , which breaks the symmetry of the process , occurs within the L D W regime and is not associated with a sudden change to a L P source . These results were supported by beam attenuation measurements to study the pulse separation variation with incident power density . Fig 4.24b shows such behavior for a lens - sample separation of 8.75 cm where the pulse separation is clearly defined . With an initial L D W plasma motion , attenuation results in little change in the pulse separation , however as a L P source is reached the pulse separation falls uniformly . For lens - sample separations between 10.25 cm and 11 cm where the two peaks are initially unresolvable , the attenuation of the beam results in the reduction of the ultrasonic amplitude to a degree where two peaks become resolvable , with

a separation of a few hundred nanoseconds , suggesting that the pulse reflections are always present in the ultrasonic waveforms and are observed as a broadening of the ultrasonic waveform .

4.7.1 Double Pulse Theory and Discussion

Previous authors have referred to the presence of secondary shock waves being recorded from laser supported plasmas . Barchukov et al [3.11] discussed the possibility of obtaining pulsating plasmotron plasmas , in which a sequence of shock waves are generated at the surface of the target under irradiation . The secondary shocks are associated with the clearing of the plasma above the target . As the plasma expands , the electron density decreases allowing penetration of the radiation into the plasma . Eventually , if the radiation is of sufficient intensity breakdown of the gas above the target occurs for a second time producing a secondary shock wave . This process may be further repeated provided the laser source is of sufficient length . No mention of a similar process occuring in the L D W regime was made , however if the process did occur one may imagine the pulse separation to be increased due to the motion of the plasma being directed towards the laser keeping the electron density high for a greater time before it .clears allowing the radiation to pass through it . If this process were the cause of the secondary waves observed in this work , the streak camera measurements would show the clearing of the plasma followed by secondary breakdown sources at the target surface . No such behavior is observed in the photographs in Fig 3.11 recorded the with the nitrogen gas mix in either L P or L D W regimes .

Ageev et. al. [3.21] suggested a second mechanism capable of producing such shock waves . In an instantaneous point explosion the plasma expands spherically . As the plasma expands the ions and atoms involved in the explosion meet resistance from the cold surrounding gas . The inner

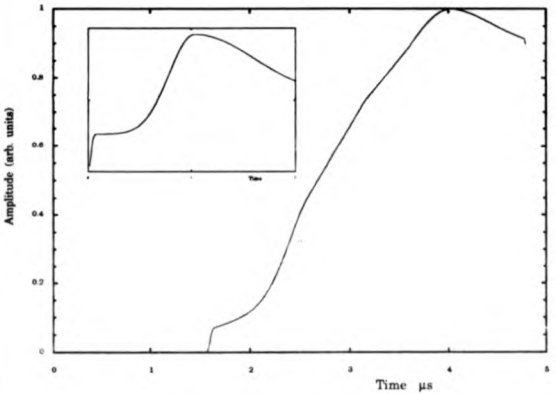

Fig 4.22 Knopoffs solution convolved with the 1000ns , pulse separation , temporal source function , shown in inset .

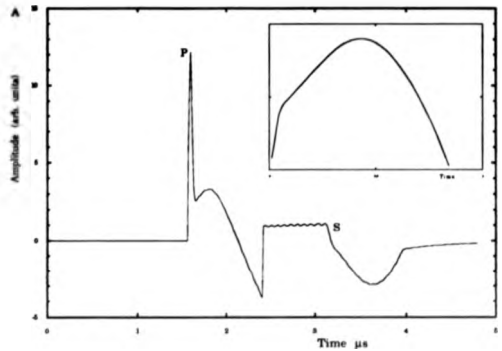

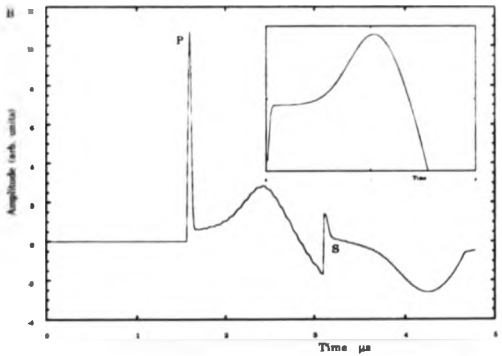

Fig 4.23 a & b Differential displacement waveforms obtained from convolution with 400ns and 1000ns pulse separation , temporal profiles having increased decay rate on those used in Figs 4.21 & 4.22

components of the plasma meet little resistance due to the rapid expansion of the outer material , and quickly catch up with the outer regions of the expanding plasma . A high pressure region is established at the outer edge of the plasma where it comes into contact with the cold gas , and the pressure cross section shown in Fig 3.15 , is rapidly established . The effect of a non instantaneous energy release , due to the finite duration of the laser pulse , is to continually release energy into the plasma . As the newly created plasma expands and traverses across the internal region of the plasma it rapidly meets the high pressure region at the plasma - gas interface , resulting in a partial reflection of the newly arrived plasma back towards the target surface . This reflection manifests itself as a secondary shock . As the release of new energy into the plasma is simply a function of laser pulse duration , this process will be a continual process . Inspection of the experimental data reveal that a well developed L P source produces the strongest pulse reflection , lending weight to the above theory , as the symmetry of this type of plasma motion means that the reflected shock is coherently directed back towards the initial target spot , which is not the case for a L D W plasma motion .

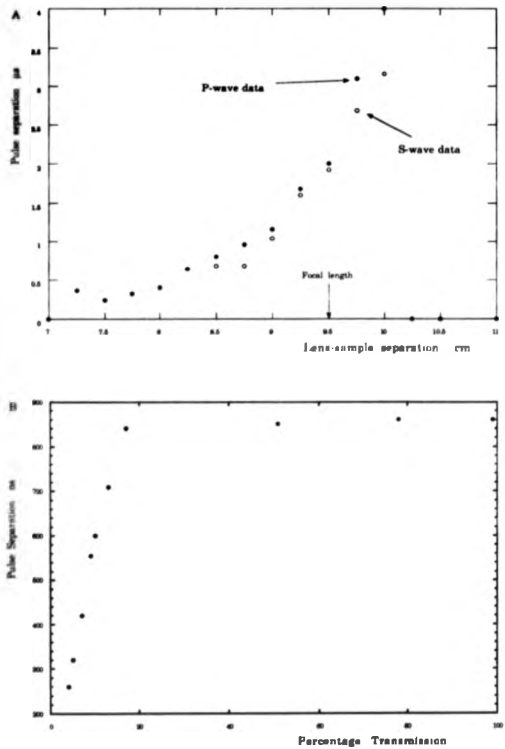

Fig 4.24 a & b Variation in pulse separation as a function of source radius and energy density respectively .

References Chapter 4

1D.C. Emmony , T. Geerken & H. Klein - Baltink , J. Acoust. Soc. Am. vol73 no1 pp220-224 (1983)
2A.A. Karabutov , V.T. Platonenks & V.A. Chupryna , Sov. J. Quant. Elect. vol15 no10 (1985)
3 N.E. Aver'yanov , Yu. A. Boloshin , L.I. Martyukhina & I.V. Pavlishin , Sov. Phys. Tech. Phys. vol32 no11 (1987)
4M.R. Wang & H.C. Meng , J. Appl. Phys. vol66 no1 (1989)
5I. Urse , I. Apostol , D. Barbulescu , J. N. Mihailescu & M. Molchovan , Opt. Comm. vol39 no3 (1981)
6 L. Knopoff , J. Appl. Phys vol29 no4 pp661-670 (1958)
7 C. L. Pakeris , Proc. N.A.S. , Geophysics , vol41 p469 (1955)
8R.J.Dewhurst , D.A.Hutchins , S.B. Palmer & C.B.Scruby , J. Appl Phys. vol53 no6 (1982)
9A. Aindow , chapter 3 Ph.D Thesis Hull University
10B.A. Raikhman & V.N. Smirnov , Sov. Phys. Tech. Phys. vol 22 no9 pp1155-1156 (1977)

Chapter 5

Characteristics of the CO_2 Laser Ultrasonic Source Profile

5.1 Introduction

The inspection of the ultrasonic source generated by the plasma using epicentral and surface waves gives a convenient means of determining the basic source properties , as a function of the laser pulse and target variables . This chapter continues the analysis of the ultrasonic source produced from the complex , time varying shock wave . This examination is carried out using two aspects of the ultrasonic transients ; its wave structure as a function of angle off-epicentre and secondly the directivity patterns of the longitudinal and shear wave arrivals . The wave structure produced by the plasma source is compared to line , disk and expanding source models . On the basis of this work a study into the effects of a wide static source on the ultrasonic directivity is examined in terms of top-hat and non-uniform source profiles .

5.2 Transient Ultrasonic Generation In Solids by Line , Disk and Expanding Sources

5.2.1 The Line Source

Achenbach [1] gives the generalized equation for elastic waves in isotropic homogeneous media in the absence of body forces as

$$\rho \frac{d^2u}{dt^2} = (\lambda+2\mu)\,\nabla(\nabla.u) - \mu\nabla^2 u \qquad 5.1$$

where λ and μ are Lame constants , ρ the density and u is the displacement vector . The displacement vector may be considered as the sum of two components originating from the scalar potential ,Φ ,associated with the longitudinal motion and a vector potential Ψ associated with the shear wave motion such that

$$u = u_p + u_s \qquad 5.2$$

with

$$u_p = \text{grad}\,\Phi \quad \& \quad u_s = \text{curl}\,\Psi \qquad 5.3$$

These relationships may be substituted back into eq. 5.1 to give the individual wave equations for the scalar and vector potentials as

$$\nabla^2\Phi - \frac{1}{V_p^2}\frac{\partial^2\Phi}{\partial t^2} = 0 \qquad 5.4$$

$$\nabla^2\Psi - \frac{1}{V_s^2}\frac{\partial^2\Psi}{\partial t^2} = 0 \qquad 5.5$$

where Vp and Vs are the longitudinal and shear velocities respectively

Pilant [2] considered the case of motion due to a line , surface , normally applied force ; the source function , F(x,y,t) ,of which may be given as

$$F(x,y,t) = -Z\,\delta(x)\,\delta(t) \qquad 5.6$$

which represents a downward , normally applied , force of magnitude Z , existing for all x=0 with impulsive time dependence . The solution of eqs. 5.4 & 5.5 is treated by taking the Laplace transform with respect to time , of the elastic wave equation and solving the transformed potential with the boundary conditions $\sigma_{zz} = F(t)$ and $\sigma_{zx} = 0$ defining the stress profile of the source . The time domain displacement solutions are obtained by taking the inverse transform using the Cagniard- de- Hoop technique [1] . This technique requires the path integration to be deformed in the transformed plane , such that the new path of integration can be obtained by inspection , ie. it is a standard Laplace transform . The exact longitudinal motion U(r,θ,t) solution to the line source problem is given by

$$U_P(r,\theta,t) = \frac{Z V_s}{\pi\mu r}\,\mathrm{Re}\left[\frac{\tau(2q^2+1)}{R(q)}\frac{dq}{d\tau}\right] H(\tau - a) \qquad 5.7a$$

$$U_\theta^P(r,\theta,t) = \frac{ZVs}{\pi\mu r}\ \mathrm{Im}\left[\ \frac{(\tau^2 - a^2)^{1/2}(2q^2 + 1)}{R(q)}\ \frac{dq}{d\tau}\ \right] H(\tau - a) \qquad 5.7b$$

where $\tau = V_s t/r$ is the normalized time function , $a = Vs/Vp$ the ratio of the longitudinal and shear velocities , θ the angle from the normal with

$q(t) = i\tau\sin\theta + (\tau^2 - a^2)^{1/2}\cos\theta$ & $R(q) = (2q^2 + 1)^2 - 4q^2(q^2 + a^2)^{1/2}(q^2 + 1)^{1/2}$

5.8a&b

The solution of the shear wave displacement is essentially the same although a different contour deformation is required . The shear motion is split into two components for both radial and tangential motion dependent on whether the angle of inspection is greater or less than the critical angle θc , given as

$$\theta c = \sin^{-1}\left(\frac{V_s}{V_p}\right) \qquad 5.9$$

For angles greater than the critical angle a "Head" wave is observed at a time between the longitudinal and shear arrivals dependent on the angle of observation . This wave is derived physically from the conversion of the surface skimming longitudinal wave to shear waves , in order to satisfy the surface boundary conditions . These waves are also termed "refraction waves"

The solutions to the shear wave motion are given mathematically by

$$U_r^R(r,\theta,t) = -\frac{ZVs}{\pi\mu r}\ \mathrm{Re}\left[\ \frac{(\tau^2 - 1)^{1/2}\ 2q(q^2 + a^2)^{1/2}}{R(q)}\ \frac{dq}{dt}\ \right] H(\tau - 1) \qquad \theta < \theta c \qquad 5.10a$$

$$U_r^R(r,\theta,t) = -\frac{ZVs}{\pi\mu r}\ \mathrm{Re}\left[\ \frac{(\tau^2 - 1)^{1/2}\ 2q(q^2 + a^2)^{1/2}}{R(q)}\ \frac{dq}{dt}\ \right] H(\tau - \tau_c) \qquad \theta > \theta c \qquad 5.10b$$

and

$$U_\theta^s(r,\theta,t) = -\frac{Zv_s}{\pi\mu r}\,\mathrm{Im}\left[\frac{2\tau q\,(q^2+a^2)^{1/2}}{R(q)}\frac{dq}{dt}\right] H(\tau-1) \qquad \theta<\theta c \qquad 5.10c$$

$$U_\theta^s(r,\theta,t) = -\frac{Zv_s}{\pi\mu r}\,\mathrm{Im}\left[\frac{2\tau q\,(q^2+a^2)^{1/2}}{R(q)}\frac{dq}{dt}\right] H(\tau-\tau_c) \qquad \theta>\theta c \qquad 5.10d$$

where $\tau_c = \cos(\theta-\theta c)$ and $q(t)$ is as for eq 5.8 with a replaced by 1. The superposition of radial and tangential components in eqs. 5.7 and 5.10 gives the resultant out-of-plane and in-plane motion within a half space . Fig 5.1 shows a series of out-of-plane motion waveforms predicted using this model for a range of angles away from the surface normal . The longitudinal arrival , over all angles , is characterized essentially as a monopolar pulse while the shear wave arrival is seen simply as a change in displacement gradient . The figure shows the emergence and form of the Head wave which becomes distinct for angles above ~40 degrees using v_p and v_s typical for metals. Fig 5.2 gives the corresponding in-plane motion , the zero degree wave being omitted as no on-epicentre shear motion is generated . The shear motion is marked by a discontinuity at $\tau=1$, the shear wave arrival time , who's motion may be considered as being comprised of separate components before and after $\tau=1$, denoted as s^- and s^+ motion respectively . The $s+$ motion is of opposite polarity to the s^- motion and contains the significant energy associated with the shear wave . The predicted 45° in-plane motion shows the presence of the Head wave observed just before the s^- arrival the two being unresolved . By 60° the Head wave is clearly detached from the shear motion and as the angle increases further it becomes closer to the longitudinal arrival . Fig 5 3 shows the polar wave distribution from such a source , which agrees with the equivalent point source case . The figure shows the relative velocities and form of the wavefronts , indicating the breaking of the Head wave from the shear motion at the critical angle .

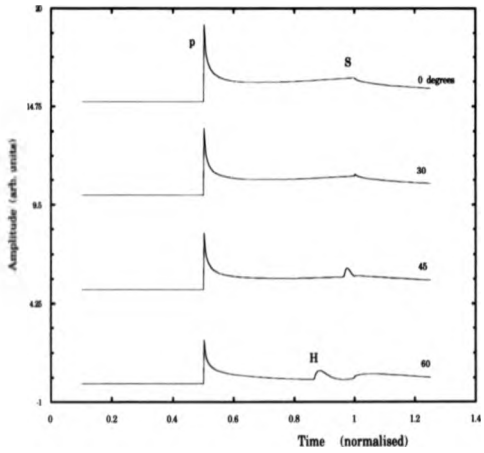

Fig 5.1 A series of longitudinal waveforms calculated from Pilanta line - source model .

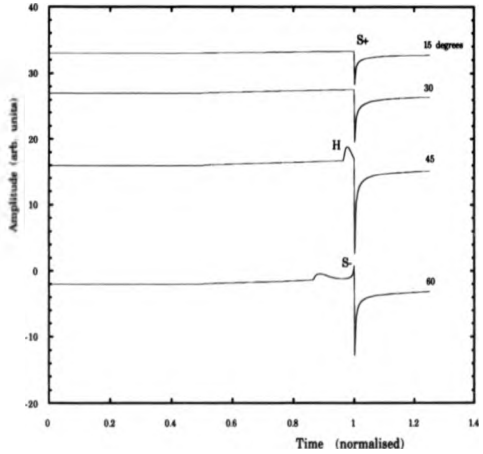

Fig 5.2 A series of shear waveforms calculated from Pilant line - source model .

The solutions give the wave attenuation to be inversely proportional to distance travelled ,r , derived from the line nature of the source . The duration of the waves after the initial arrivals is prolonged , again due to the nature of the source . A single point source would produce a delta type discontinuity at the longitudinal arrival whereas the off-epicentre contributions from the line source extend the time duration of the wave arrivals . The general form , relative polarity and amplitude of the wave arrivals however agrees well with the computationally more complex solutions to the point source case . Pilant's solutions , therefore , give an adequate description of the ultrasonic field within a half space and may be used to model the point source waveforms . However the analysis falls well short of being a description or basis for the understanding of generalized source functions , as is desirable when working with PZT transducers or wide laser sources , which is of particular interest in this work . Simple convolution of Pilant's waveforms over a finite spatial extent to represent a wide ultrasonic source breaks down rapidly as the source size becomes greater . This is due to a summation , over an angular range , of differing source components produced across the wide source .

5.2.2 The Wide Source

In an attempt to solve this problem Bresse [3] used a double Laplace - Hanckel transform technique which enables both time and spatial integration to be carried out over the source dimensions . The Laplace transform , transforms the time domain information, as carried out by Pilant , such that with knowledge of the source stress profile , the point source solution may be calculated for any point in its bounds. Generalization to a wide source is carried out using the Hankel transform on the transformed time domain solution to convolve the source spatially . This impulsive force calculation is an extension of Kawashima [4] who carried out the integral over a narrow

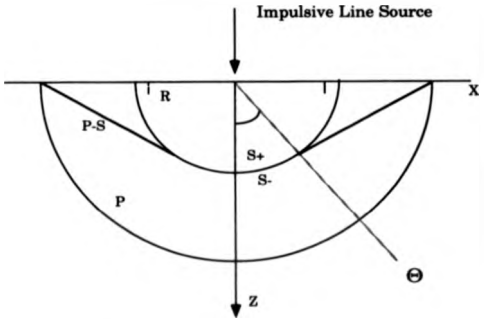

P LONGITUDINAL WAVE

S SHEAR WAVE (S+ & S- COMPONENTS)

P-S HEAD WAVE

Q CRITICAL ANGLE

Fig 5.3

The wavefronts of the bulk and surface waves generated by the impulsive line source

frequency band . The general solutions obtained by Bresse contain a description of the source distribution , F(x,t) . Bresse considered two axially symmetric , normally applied sources , which for clarity had an impulsive time dependence such that any waveform modification would be derived from the source dimensions alone . Arbitrary temporal source distributions may be accounted for by subsequent convolution . The sources considered were that of the simple top-hat function expressed as

$$F(x) = 1 \qquad |x| < a$$
$$= 0 \qquad |x| > a \qquad 5.11$$

and what Bresse termed the "apodized" source function given by

$$F(x) = 2\left(1 - \left(\frac{x}{a}\right)^2\right) \qquad |x| < a$$
$$= 0 \qquad |x| > a \qquad 5.12$$

Both of which are shown in Fig 5.4 . Substitution of these source profiles into the general solutions , which after suitable manipulation of the integration contour and limits yields a form which may be solved using Cagnards method.

The results of this work suggest that a non-point like or extended source will produce waves which emanate from the centre and edge of the source termed "plane" and "edge" waves respectively . Fig 5.5a shows the predicted epicentral waveform , produced by a top-hat source profile , with a ratio of source width to sample thickness of 0.5 . For comparison Fig 4.3a shows the time derivative of Knopoff's solution , given as the corresponding point source solution . The longitudinal arrival in Fig5.5 a, is broadened into effectively a top-hat function , existing in time from t_p to $t_p(e)$ where , p , represents longitudinal waves (a similar convention being used for shear waves) and ,e, represents waves originating from the edge of the source . No shear wave is observed at the time corresponding to the plane wave arrival , due to the fact that shear waves will only emanate from the edge of the source as the region in between has only a planar stress applied . Fig 5.5b shows the corresponding

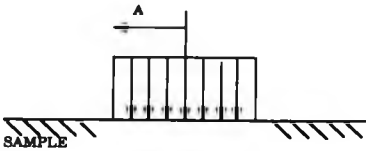

FORCE PROFILE 1 |X| < A
0 |X| > A

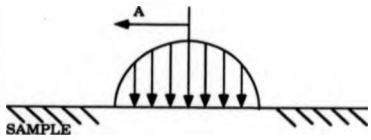

FORCE PROFILE 2(1 - (X/A)^2) |X| < A
0 |X| > A

Fig 5.4

The Top-hat and Apodized source functions considered by Bresse in the development of the wide , ultrasonic source .

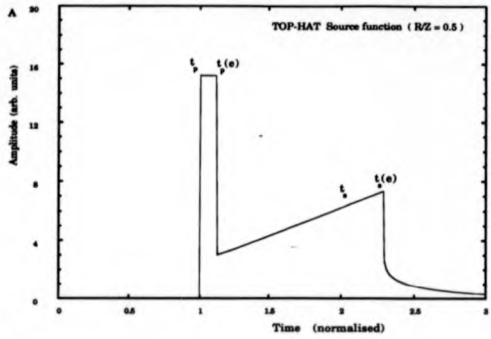

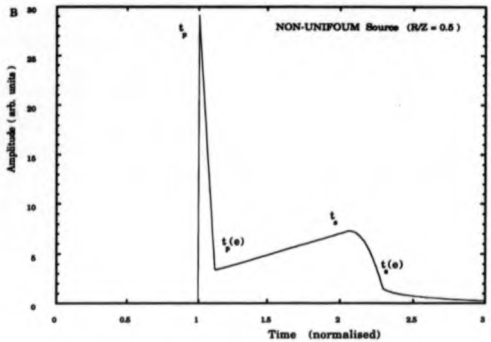

Fig 5.5 a & b Theoretical epicentral displacement waveforms calculated for top-hat and apodized source functions respectively .

waveform to that in Fig 5.5a , but with an apodized source function . The longitudinal arrival decreases uniformly in amplitude from a maximum at the plane wave arrival until the edge wave arrival . This decrease is observed due to the source strength reducing to zero across its radius . The non-uniform nature of this profile also results in shear waves being generated across its width , resulting in a gradual decrease between the plane and edge shear arrivals as opposed to the sharp discontinuity observed in the top-hat solution .

Fig 5.6 shows a series of off-epicentre longitudinal waveforms predicted by Bresse's modal calculated for a 1mm radius , top-hat source , on a 50mm radius hemicylinder . The width of the longitudinal waves is again defined by the limits of the plane and edge wave arrivals and is seen as a sharp monopolar peak . This contrasts with Pilant's solutions which show the elongated post longitudinal arrival structure produced by the line source . Comparison with the Pilant waveforms in Fig 5.1 shows however close agreement in the relative amplitude and polarity of the longitudinal , shear and Head waves between the two models . Similar broad agreement is observed between the shear motion predicted by Bresse , shown in Fig 5.7 , and that of Pilant , Fig 5.2 , over the range of angles from the normal . Increasing the source radius results in the corresponding increase in longitudinal and , in the case of non-uniform source distributions , the shear durations , as shown in Fig 5.8 , for both out-of-plane and in-plane motion at an angle of 45° resulting in the broadening of the wave arrivals due to the increase in source size . Therefore comparison of the experimental data with the theory of Bresse should give an indication of the source size generated using the plasma source.

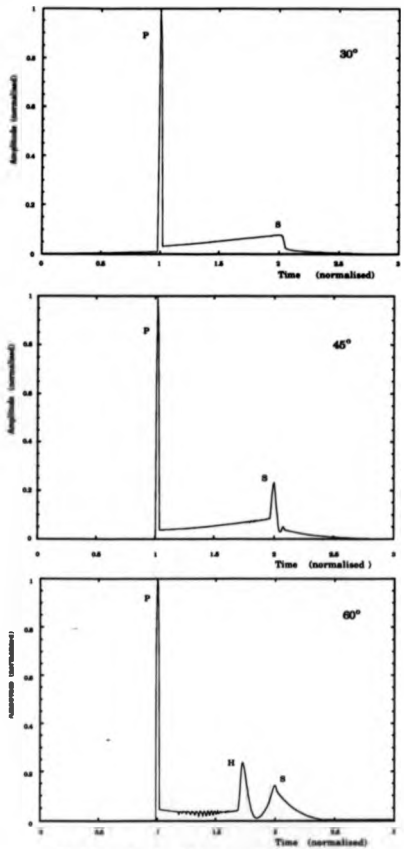

Fig 5.6 A series of [illegible] Brune's wide source model .

5.2.3 The Expanding Source

The work of Bresse thus accurately models sources normal to the surface which are of finite extent but static in dimension throughout their history . Plasma breakdown , as described in chapter 4 , may generate a L D W , which travels in a one dimensional fashion away from the sample surface . It produces to a first approximation a source of constant dimension , and thus one which is satisfied by Bresse's analysis . On the other hand the L P source is one which expands spherically across the sample surface . The radial expansion of the plasma acts to produce an expanding source distribution , which may be modelled as an expanding disk source . Such a source has been described by Gachenheimer [5] , using an axisymmetric normally applied surface load which expands at a constant rate . These loads exert a constant force on the surface which produces a decay of surface stress inversely proportional to time squared , given by

$$\sigma_{zz}(r,t) = \frac{-F_0\, H(vt-r)}{2\pi r^2} \qquad 5.13$$

$$\sigma_{zr}(r,t) = 0$$

where v is the velocity at which the source expands . Three rates of expansion are considered (i), supersaismic expansion ,V>Vp , (ii), transseismic Vs<V<Vp and (iii), subseismic , V<Vs , where Vp and Vs have their usual meaning .

In a manner similar to Bresse , Gackenheimer employed a double Laplace - Hankel transform technique to solve the temporal and spatial problem . The solution of the wave splits into two components dependent on the relative source and ultrasonic velocities as discussed above . A hemispherical wave originates directly from the sudden application of a load at a point on the surface , a solution which is in agreement with stationary source solutions . A second wave originates from the edge of the source forming a conical wavefront . This wave only becomes observed when the

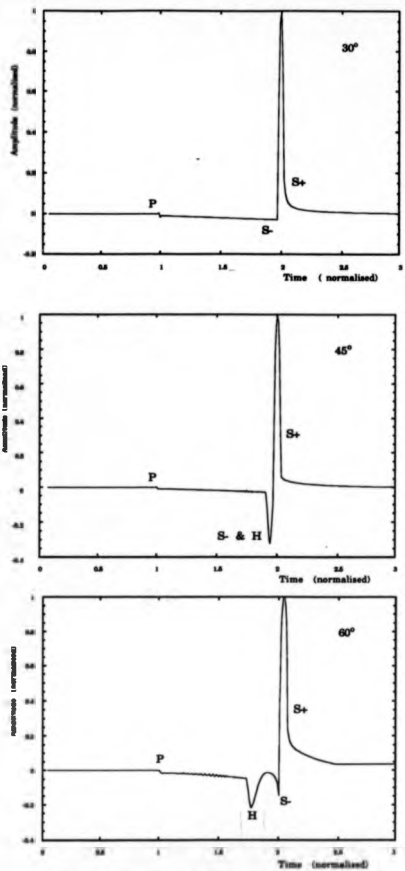

Fig 5.7 A series of in-plane motion waveforms calculated using Bresse's wide source model .

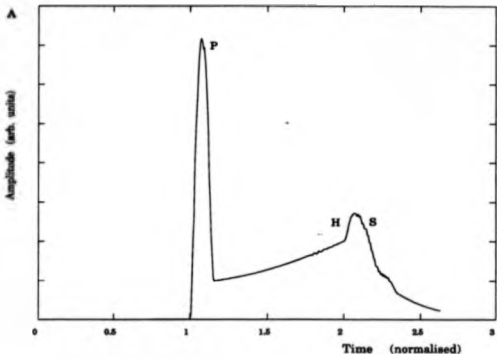

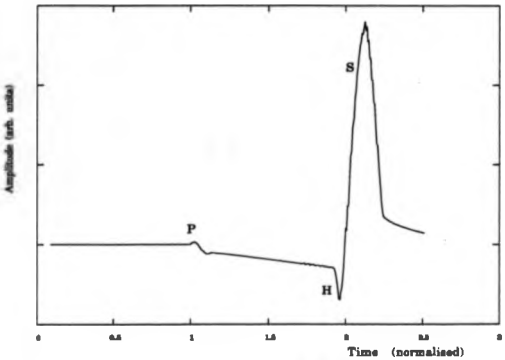

Fig 5.8 a & b Out-of-plane and in-plane motion derived from a 5mm radius , non-uniform source calculated at 45° , using Brune's wide source model .

source expansion velocity is superseismic . The angle above which the conical wave is observed in the case of longitudinal wave is given as

$$\phi_c = \sin^{-1}\left(\frac{V_P}{V}\right) \qquad 5.14$$

Subseismic source velocities only produce hemispherical wavefronts . Fig 5.9 shows the wavefronts produced by both superseismic and transseismic source expansions . The superseismic case shows conical wavefronts associated with the longitudinal and shear motion , while the transseismic case produces only one conical wavefront which is derived from the shear motion . The resultant detected waveform therefore shows distinct arrivals associated with the individual wavefronts . Fig 5.10 shows the predicted waveform produced by a superseismic source , for 60° off-epicentre . The wave , which may be compared to the integral of Fig 5.6c , shows the effect of the conical waves . These wave arrivals occuring before the normal longitudinal and shear waves and also result in a distortion of the static source wavemotion .

5.3 Plasma Generated Off-Epicentre Waveforms

To enable correct comparison between experimental and theoretical waveforms to be made , the correct source - receiver combination must be used The theoretical models for both Pilant and Bresse employ delta function time dependencies in the calculation of surface displacement . Both out - and in - plane EMATs were used to detect the ultrasound and as such differentiate the surface displacement . Therefore to obtain the correct source - receiver combination a Heaviside source type is required , generated with a L P source . The ultrasonic transients were recorded on a 50mm radius aluminium hemicylinder . Fig 5.11 shows a series of experimentally recorded longitudinal waves . On inspection it is firstly worth noting that the negative portion of the longitudinal arrival indicates that the source was not a true Heaviside , and is

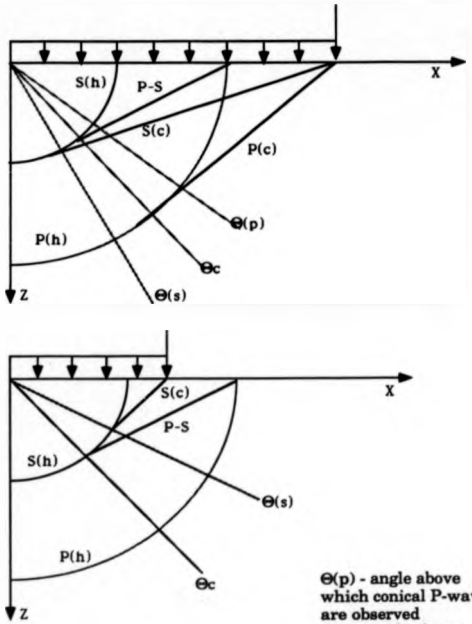

Fig 5.9

The wavefronts produced by Gackenheimer's expanding disk source function , showing the hemispherical and conical waves .

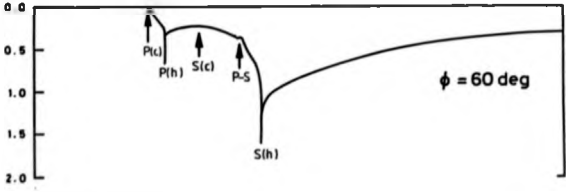

P(c) conical longitudinal wave
S(c) conical shear wave
P(h) hemicylindrical longitudinal wave
S(h) hemicylindrical shear wave
P-S Head wave

Fig 5.10 Gackenheimer's predicted displacement at 60° off-epicentre generated by a supersesmic expanding disk source .

in agreement with Fig 4.1 which would on differentiation produce such a slight negative pulse and is purely a limitation of the reduced nitrogen gas mixture . This effect will also be observed on the shear motion , however the overall wave structure agrees well with that expected from such a source combination and comparison between theory and experiment may be made .

The essentially monopolar pulse of finite width predicted by Bresse is closely matched by the experimental data . The shape , width and polarity of the wave arrivals agree closely with those in Fig 5.6 , however the shape of the shear arrival gives no indication of uniformity of the source function . Fig 5.12 gives the corresponding shear waves to those in Fig 5.7 , again showing close agreement , adding weight to Bresse's calculations . The shear wave data shows a distinct longitudinal arrival to be detected , which may be a result of fringing fields from the EMAT making the device sensitive to out-of-plane motion . The F.W.H.M. of the longitudinal wave may be used to determine the source size . The ultrasonic pulse width , W , is dependent on of the time duration of the laser pulse , τ , the EMAT detector width response ,Δt , and the geometrical source width , giving W as

$$W = \tau + \Delta t + \frac{2a\sin\theta}{V_p} + \frac{a^2}{2V_pR} \qquad 5.15$$

where R is the sample radius . Terms in a , the source radius , are due to the source geometry which has an angular independent term originating from the difference in travel times from the centre and edge of the source and an angular dependent term accounting for the difference in travel times from across the source width . Measurement of the longitudinal pulse widths over a range of angles gives a value of 0.8±0.1 mm for the source width compared to 1.2±0.1 mm obtained from heat sensitive paper measurements .

The ultrasonic waveforms recorded with either the interferometer or the EMAT show no distinct pre-longitudinal or shear wave arrivals associated with an expanding disk source . Velocity calculations of the plasma growth

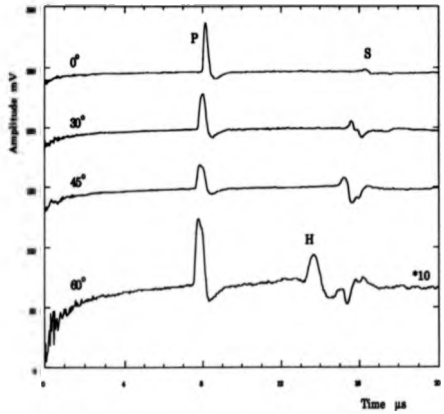

Fig 5.11 A series of experimentally recorded longitudinal waves detected over a range of angles from the surface normal. Measured with an out-of-plane sensitive EMAT.

The 60° waveform is magnified for clarity

from the streak camera results show the plasma to grow in the L P regime with an average velocity of ~400ms^{-1} . This indicates that the velocity of the plasma expanding across the surface is transseismic . Initially however this velocity is higher by a factor of between two and three , leading initially to a superseismic source . The subsequent decrease in velocity causes the source to continually change in nature , from superseismic to subseismic , giving a corresponding change in the direction of the conical longitudinal and shear wavefronts resulting in a smearing of these wave components and a general loss in definition .

Therefore the complex nature of the plasma can be modelled , within the sensitivity of these measuring techniques , by a stationary source of finite width . Measurements of the wave widths indicates that breakdown does not occur uniformly across the whole irradiated area but is effectively localised within this area resulting in a smaller source width than expected , a fact which is considered further in the directivity measurement section . The experimental results agree closely within the limits of the imposed source requirements , with the theoretical results of Bresse . Chapter 6 will extend the comparison between this model and the wide source , CO_2 laser generated ultrasonic transients .

5.4 Modified Directivity Patterns

5.4.1 Introduction

The effect of the finite source size on the ultrasonic waveforms described in the previous section also results in the modification of the directivity pattern of the ultrasound within the material . Previous studies of laser generated ultrasound , using Nd:YAG , ruby and nitrogen lasers , have suggested that the source approximates well to a point source . Hutchins et. al. [6] used the

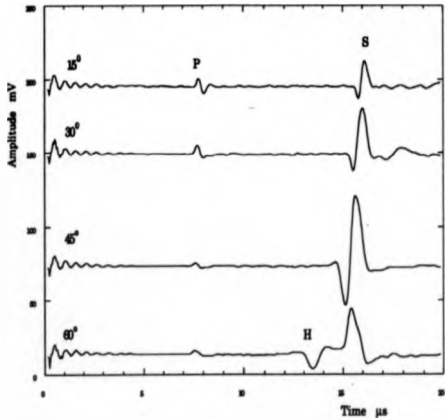

Fig 5.12 A series of experimentally recorded shear waves detected over a range of angles from the surface normal. Measured using an in-plane sensitive EMAT.

theory of Miller and Pursey [7] to show the form of the normal force longitudinal directivity as generated in the ablative regime . It is important to note that for dispersionless media and a point acoustic source the directivity amplitude will be independent of the driving frequency . Thus under these conditions the model should hold for any arbitrary driving force function , which in the case of the laser may be impulsive . The results of the theoretical directivities gives close agreement with the measured longitudinal directivity but poor agreement with the corresponding shear wave energy distribution . The theory of Miller and Pursey , Cherry [8] and also Lord [9] give only the peak to peak amplitude variations of the ultrasonic transients as a function of angle

This is sufficient for the longitudinal wave motion as it remains a monopolar pulse over all angles , however the nature of the shear wave is more complex as it contains both the s^- and s^+ motion as well as the Head wave mixing over a range of angles about the critical angle . The effect of the Head wave is thus to artificially increase the peak to peak amplitude of the shear directivity over the angles where it is unresolvable from the shear wave . Therefore as a basis for an understanding of the effect on directivity of a finite , broadband ultrasonic source , the point case must first be fully understood . A potentially valid model for the point source directivity is that of Pilant , which despite using a line source , agrees with the relative wave arrival amplitudes as predicted by the more computationally complex point source models .

5.4.2 Point Source Directivities

Pilant's model allows the angular directivity of the longitudinal , s^- and s^+ waves to be determined by calculating their amplitude at the corresponding arrival times . The longitudinal directivity in Fig 5.13 , shows that the energy associated with this wave has a maximum value on-epicentre and falls off continually with increasing angle . This distribution is very similar to those predicted by Miller & Persey [7] and Lord [9]. The experimental data , shown

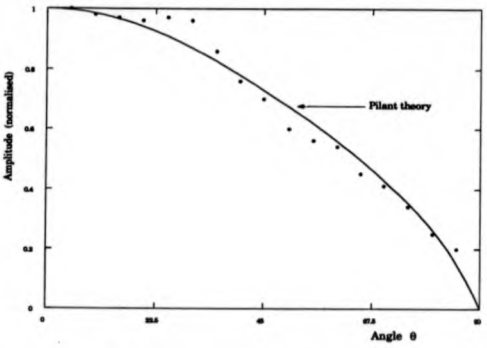

Fig 5.13 Measured longitudinal directivity derived from a point source and that predicted by Pilant's line source model .

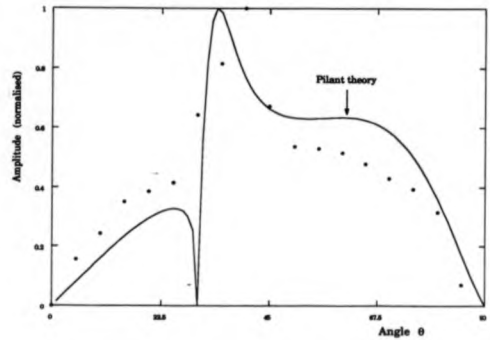

Fig 5.14 Comparison of Nd:YAG , point source , shear directivity with that derived by Pilant

as points , were recorded using a tightly focused Nd:YAG laser source working in the ablative regime . The data shows a very close match between theory and experiment . Fig 5.14 shows a similar comparison between theory and experiment for the peak to peak shear wave amplitude . Overall agreement is observed apart from the discrepancy in the peak position . The angle of the experimental peak is seen to be just after the critical angle where the Head wave is still associated with the s^- motion . This leads to a false estimation of the peak to peak and s^- amplitude in this region . A guide to the presence of the Head wave is the sudden broadening of the s- wave but this does not however lead to the accurate measurement of the two amplitudes .

The individual s^+ and s^- components are shown in Fig 5.15 a & b respectively together with the experimentally recorded data . The s+ data shows something of the pre - 30 ^{o} lobe followed by a broad , large energy lobe which peaks at -35^o and falls away to zero at 90^o . The s- data reveals a peak in the data before 30^o which is not shown in the theoretical directivity , the data then peaks at 40^o , due to the reason of the Head wave mixing discussed previously . The s^- energy detected for angles above 45^o does not show the broad nature of the second lobe , staying zero up to angles of -65^o followed by a localized peak which again falls to zero at 90^o .

5.4.3 Line Source Directivities

An attempt was made to reproduce the source conditions required by Pilant for an infinite line source . To facilitate this a hemicylindrical sample of radius 50mm and width 15 mm was used . The width of the sample corresponds to the length over which an ablative line source may be generated , using a -250mJ laser pulse energy , and thus the source may be considered as being infinite with respect to the sample width dimension . The form of the waves generated did not change noticeably from the point source case . The effect of filtering by the EMAT amplifier will remove the very low frequency

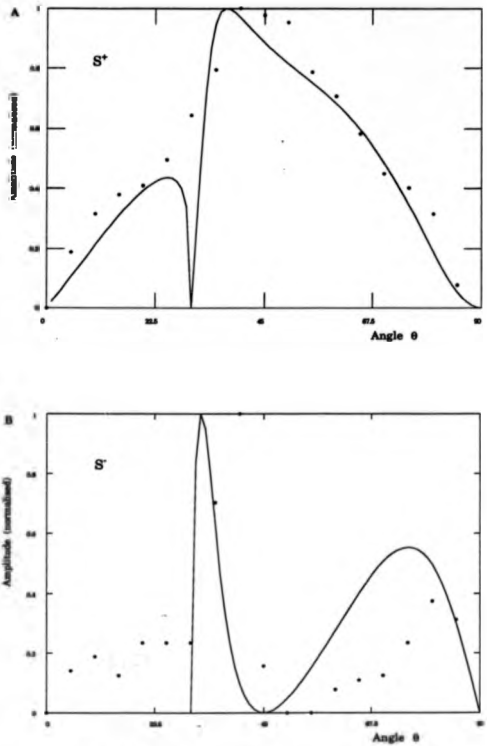

Fig 5.15 a & b Nd:YAG point source transmission , with the corresponding Pilant theory , for the S^+ and S^- components of the shear wave .

components derived from wave contributions across the source , making the obtained waveforms tend closer to the point source case . The measured directivity agreed to within experimental errors with that of the point source case . In conclusion the directivity patterns calculated from Pilant's work agree well with the experimental data for both line and point sources . In addition this approach provides a computationally simple basis on which to to extend the work to wide source directivities .

5.5 Wide Source Directivities

The starting point on which the extension to a finite source size is made , is based on the standard model of radiation from a piston source into an infinite baffle . Fig 5.16 shows the geometrical arrangement of such a source . The acoustic potential at a point P is derived from the sum of all source elements across the area of the piston . The elemental potential , $d\Phi$, from such a source may be given as

$$d\Phi = \frac{dQ}{4\pi h} \exp i(\omega t - kh) \qquad 5.16$$

where $dQ/4\pi h$ is the elemental source strength measured at P a distance h away from the source element , ω and k are the angular frequency and wavenumber of the acoustic wave . The source strength , Q , may be defined as

$$Q = \int_{(l)} u_s . n . ds \qquad 5.17$$

where n is the normal to the source and u_s is the amplitude of oscillation , giving $dQ=2u_s ds$. The factor of two originates from the integration around the surface of the source . Using the Cartesian coordinate system shown (Fig 5.16) , h may be expressed exactly by

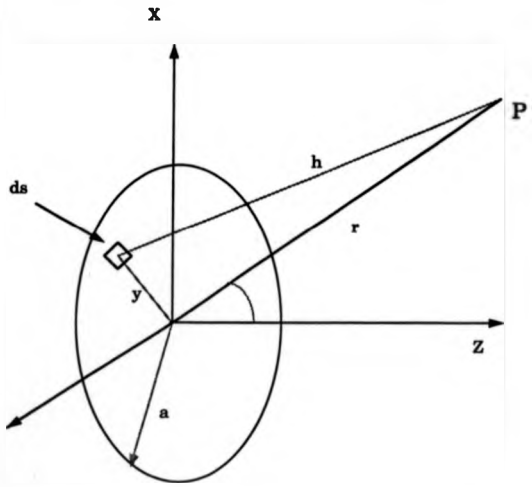

Fig 5.16

Geometry for wide source analysis , showing a uniform piston of radius a being observed at a point P in the far field .

$$h = r\left(1 - \frac{2y\sin\theta\cos\phi}{r} + \left(\frac{y^2}{r^2}\right)\right)^{1/2} \qquad 5.18$$

Observations in the far field constrain the allowable values of y and r to y/r << 1 removing the third term in eq. 5.18 . The expression for h can be simplified further if a binomial expansion is used and again only first order terms are retained , resulting in

$$h = 1 - \frac{y}{r}\sin\theta\cos\phi \qquad 5.19$$

Thus substitution of eq. 5.19 into eq. 5.16 gives the elemental acoustic potential as

$$d\Phi = \frac{u_o y d\phi dy}{2\pi r\left(1 - \frac{y\sin\theta\cos\phi}{r}\right)} \exp\left(i(\omega t - kr + ky\sin\theta\cos\phi)\right) \qquad 5.20$$

Further simplification is undertaken by keeping only the angular dependence in the exponential term , which is again reasonable assuming y/r <<1 . Thus the total potential at P , Φp ,can therefore be obtained from integration across the whole source as given by

$$\Phi p = \frac{u_o}{2\pi r}\exp i(\omega t - kr)\int_0^{2\pi}\int_0^{a}\exp\left(iky\sin\theta\cos\phi\right) y\, dy\, d\phi \qquad 5.21$$

Employing the change of variables , z = kysinθ , and using the definitions

$$J_o(z) = \frac{1}{2\pi}\int_0^{2\pi}\exp(iz\cos\phi)d\phi \qquad 5.22$$

and

$$\int zJo(z)dz = zJ1(z) \qquad 5.23$$

where Jo and J_1 are the zero and first order Bessel functions . This gives upon integration the final form of the potential as

$$\Phi_p = \frac{u_o a^2}{r} \exp i(\omega t - kr) \left(\frac{J_1(ak\sin\theta)}{ak\sin\theta} \right) \qquad 5.24$$

which if a and k tend to zero gives the spherical , point source directivity solution . This form of Bessel function modification of a point source solution is very common and is directly analoga to the electromagnetic case of waves diffracting from a circular aperture [10] and was derived by , amongst others , Miller & Pursey and is the form which will be used in this work . The form of the point source directivity used is that of Pilant which was shown in section 5.4.2 , to give an accurate description for the point source case.

5.5.1 Arbitrary Source Functions

The top-hat source distribution described above can be used as a basis of a non-uniform source distribution . Assume a simple source profile as given below

$$F_1 = \begin{cases} 2A & |x|<a/2 \\ A & a/2<|x|<a \\ 0 & |x|>a \end{cases}$$

where a is the radius and A an arbitrary amplitude or source strength . This function may be rewritten as the addition of F_2 and F_3 which are expressed as

$$F_2 = \begin{cases} A & |x|<a/2 \\ 0 & \text{elsewhere} \end{cases}$$

and

$$F_3 = \begin{cases} A & |x|<a \\ 0 & \text{elsewhere} \end{cases}$$

In the limit such an approach is that of integration , as shown in Fig 5.17 ,and as such much more complex source geometries may be examined purely as a sum of top-hat source functions .

A different approach has however been adopted in this work to determine an exact solution for a non top-hat type source . The source type chosen was the "apodized" source profile considered by Bresse , in an attempt to cross

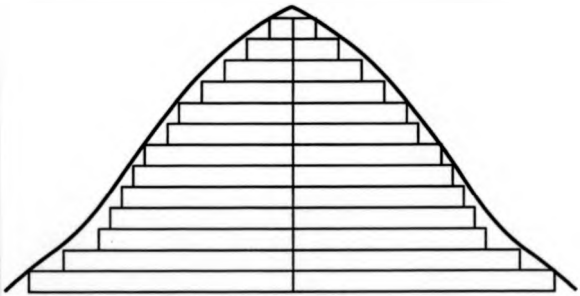

Fig 5.17

A general source distribution deconvolved into a series of top-hat source functions .

correlate the ultrasonic directivities and waveforms obtained from the CO_2 laser supported plasma source . The analysis proceeds as for the case of the simple top-hat source , giving an expression for the source strength

$$Q = \int_s u_o\left(1 - \left(\frac{y}{a}\right)^2\right) y \, dy \, d\phi \qquad 5.25$$

This is then substituted into the elemental acoustic potential . The same geometrical limitations and subsequent simplifications are made in this case , as they are independent of source geometry yielding an expression for total potential which may be considered in two parts . Firstly a contribution which is simply the top-hat source and as such gives the solution presented in eq 5.22 . The second contribution originates from the non-uniform , $(y/a)^2$ term in eq 5.23 leading to the potential ,Φ_2 , given by

$$\Phi_2 = \frac{u_o}{4\pi a^2 r} \int_0^{2\pi}\int_0^a y^3 \exp(ik \sin\theta \cos\phi) \, dy \, d\phi \qquad 5.26$$

which using the change of variable employed before and eq 5.22 gives

$$\Phi_2 = \frac{u_o}{2a^2k^4\sin\theta^4} \int_0^x z^3 \, Jo(z) \, dz \qquad 5.27$$

From the general expression for Bessel functions used to derive eq. 5.23 , expressed as

$$\int x^m J_o(x) \, dx = x^m J_1(x) + (m-1)x^{m-1}J_0(x) - (m-1)^2 \int x^{m-2} J_0(x) dx$$

gives on expansion and substitution into eq 5.27 the final expression for Φ_2 . Combination of the two potential terms results in the general expression for the acoustic potential at any point in a half space , provided it is in the far field which may be expressed as

$$\Phi_p = \frac{u_o a^2}{2r}\left(\frac{J_1(z)}{z} - \frac{1}{z^2}\left((z^2-4)\frac{J_1(z)}{z} + 2J_0(z)\right)\right) \qquad 5.28$$

The above analysis may be easily extended to include source terms which are modified by higher power terms than that used in the apodized source function . The presence of the zeroth order Bessel function , which is out of phase by π with the first order Bessel function will serve to lessen the sharpness of any source size effects as is physically reasonable as the source is no longer uniform across its radius .

Both the above modifying factors require exact solution of the Bessel functions for a large range of arguments . The calculations for both order functions are split into two parts , using a series expansion for arguments below sixteen and an asymptotic expansion above this value , as described by

$$J_n(x) = \sum_{k=0}^{\infty} \frac{(-1)^k \left(\frac{x}{2}\right)^{2k+n}}{k!\,\Gamma(n+k+1)} \qquad x<16 \qquad 5.29a$$

$$J_n(x) = \sqrt{\frac{2}{\pi x}} \cos\left(x - \frac{n\pi}{2} - \frac{\pi}{4}\right) \qquad x>16 \qquad 5.29b$$

where Γ is the Gamma function and n the order of the Bessel function . The series expansion solution becomes unstable for x>20 , even for summations of up to k=1000 and thus it is convenient to use the asymptotic expansion . To ensure a continuous interchange across the two a nodal point at x=16 is chosen . The result of the Bessel function analysis is shown in Fig 5.18 , demonstrating the continuous evaluation of both orders of Bessel function and also shows the relative phase difference between the two .

5.5.2 Integration over Frequency

The integration over frequency cannot be carried out in a similar manner to that used to calculate the non-uniform source distribution . Therefore a technique of numerical integration is used over frequency . The frequency

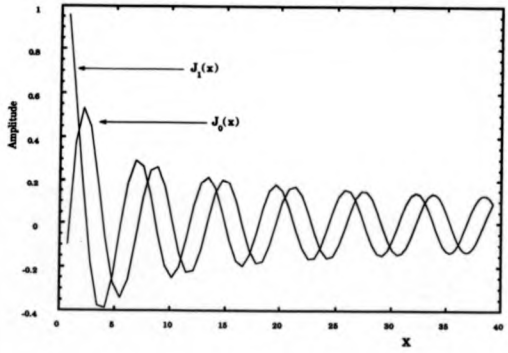

Fig 5.18 The 0th & 1st order Bessel functions .

spectrum of the longitudinal waves shown in Fig 4.9 , gives a spectrum from which a weighting function of the relative frequency components may be obtained . An expression for the frequency envelope was determined by a trial and error approach leading to a solution of

$$W(f) = \frac{0.37}{f} \qquad f > 1MHz \qquad 5.30$$

where f is the frequency of the ultrasound , in MHz , and W is the weighting amplitude . This expression becomes invalid for frequencies below 1 MHz , however in the range of a•k values considered in this study contributions from frequency components lower than this do not effect the overall result . The final expression for the acoustic potential , for the top-hat source function is therefore given by , assuming all frequency elements have the same phase

$$\Phi_p = D(\theta) \cdot \sum_{kl}^{ku} W(k) \frac{J_1(a k \sin\theta)}{(a k \sin\theta)} \qquad 5.31$$

where $D(\theta)$ is the Pilant point source directivity , $W(k)$ the weighting function in terms of wavenumber and k_u and k_l are the upper and lower limits of the acoustic wavenumber , the non-uniform , apodized , source function being treated in exactly the same manner . The integration is performed using a Simpsons rule formulation summed over ten points , which will give solutions accurate to the forth decimal place , an accuracy far superior in that associated with the weighting function .

Before the overall directivities are presented the effect of the Bessel function summed over frequency is described . Fig 5.19a shows the Bessel function modifying term calculated for a top-hat source , with frequency components of 1- 4 MHz and source radii between 1- 4 mm . The first point of consideration about the form of this function is that it is non-oscillatory , a result which is due to the summation over frequency components within the

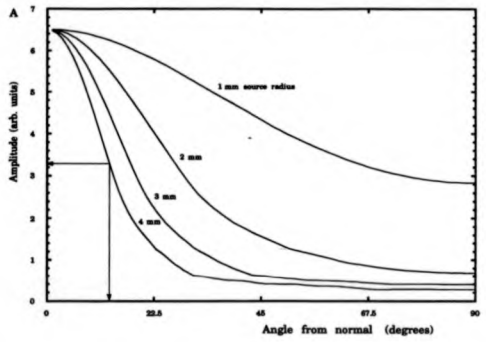

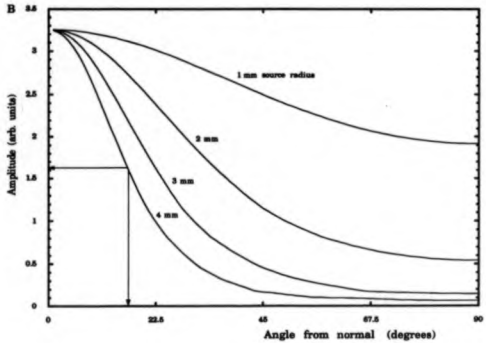

Fig 5.19 b Bessel function modifying envolopes integrated over frequency from 1- 4 MHz , for the top-hat and non-uniform source distributions respectively .

ultrasonic wave . Thus the wideband directivities derived from a laser source differ from the narrow band , PZT type directivities which do produce side bands or lobes of radiation in the directivity pattern . The effect of increasing source size is to reduce the angular range over which the modifying envelope exists . As the Bessel function is only dependent on the product of the source radius and the ultrasonic wavenumber then the same effect would be observed from a small radius , high frequency source . This possibly explains the discrepancy between Pilant's theory and the experimental Nd:YAG measurements presented in Fig 5.14 as the Nd:YAG produces ultrasonic frequencies up to ~25MHz . Fig 5.19b shows the corresponding modified envelopes to those in Fig 5.19a for the non-uniform source function .

As for the top-hat source type the non-uniform Bessel modifying envelope shows no oscillatory motion and becomes narrower as the a•k product becomes larger . The apodized source results shows that the envelope does not decay as sharply as for the top-hat case . This effect is most noticeable for the wider source radii case as this is where the the Bessel function oscillates most rapidly . Comparison of the FWHM for the 4mm source radius top-hat and apodized functions shows an increase in the envelope width by a factor of a third for the non-uniform case as is expected from the reduced weighting from the outer regions of the source .

5.6 Experimental Directivity Results & Discussion

Experimental directivity data was recorded over a range of source sizes ranging from 1mm to 4mm in radius . The experimental arrangement used was that shown in Fig 5.20 , which is identical to that used to record the waveforms shown in Figs 5.11 & 5.12 . The use of a reference signal not only assures a constant source type but also ensures that the ultrasonic source is of the same shot-to-shot amplitude thus reducing one source of measuring error

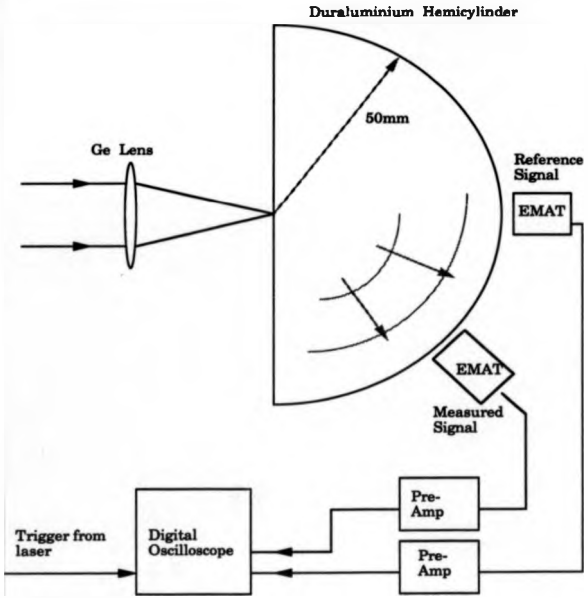

Fig 5.20

Experimental arrangement for the measurement of ultrasonic directivities .

The positioning of the EMAT is another possible cause of experimental error , as the magnetic field may detect a mixture of out-of-plane and in-plane motion if it is not aligned tangentially to the the surface of the sample . The results shown are averaged over three EMAT placings for each individual directivity measurement , thus again reducing the experimental errors . The determination of the individual source size was made via burn paper , as this produces a repeatable measure for the irradiated area . This is however an upper limit to the source size as indicated by the F.W.H.M. measurements of the longitudinal wave durations presented earlier .

The results show the peak to peak amplitudes of the longitudinal and shear waves . The s^+ and s^- data become unresolvable as the plasma source changes from a L P to a L D W and the waveforms become partially differentiated . The data recorded for a 4.00 mm source radius is discussed in chapter 6 and matches the required source conditions required for Pilant's theory . Fig 5.21 a,b,c & d show the experimental longitudinal directivities for source radii of 1.00, 1.75 , 2.13 and 4.00 mm's respectively . The figures also show the predicted theoretical calculations for both the top-hat and apodized source functions . The graphs show the experimental data to follow the predicted trend of decreasing width with increasing source radius . The non-uniform source profile directivity is seen to give better agreement than the top-hat source , to the experimental data , as is expected from the nature of the breakdown source , which grows rapidly from one or more initiation site .

Fig 5.22a,b,c & d show the corresponding shear wave data to that in Fig 5.21 . The main effect of the widening of the source is to shift the distribution of the energy into the low angle lobe . The relative heights of the first and second lobe agree well over the range of source sizes , suggesting that the source size , wavenumber product is in close agreement to that generated by the plasma source . Again the apodized source directivity show closer agreement with the experimental data than does the top-hat function , which gives over-prediction

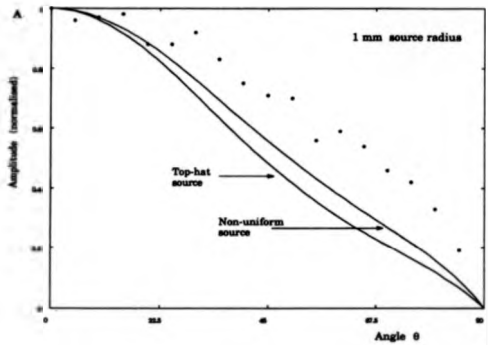
A
1 mm source radius
Amplitude (normalised)
Top-hat source
Non-uniform source
Angle θ

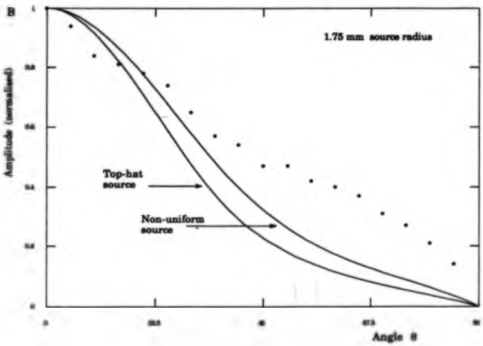
B
1.75 mm source radius
Amplitude (normalised)
Top-hat source
Non-uniform source
Angle θ

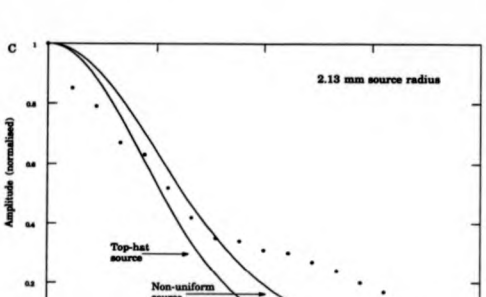

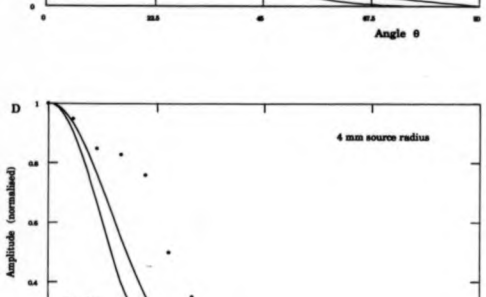

Fig 5.21 a , b , c & d Measured and theoretical longitudinal directivities for a range of source radii .

of the decay of shear amplitude with increasing angle . This is most apparent in the calculation of the 4.00mm radius source directivity where the relative heights of the two shear energy lobes is dramatically different for the two theories , the top-hat source leading to a large over-prediction in the effect of the source width modification.

5.7 Conclusion

The plasma ultrasonic source has been shown to produce a non-point , wide source with a non-uniform spatial profile . The comparison of the ultrasonic wave structure with the spatially static line source model of Pilant and the wide source model of Bresse shows that the plasma generated , ultrasonic waves may be described closely by the wide source model . The effects of an expanding disk source , as proposed by Gackenheimer , being the existence of conical longitudinal and shear wavefronts were not observed . The non-uniform expansion velocity of the plasma across the sample surface may however result in the loss in definition of such conical wave arrivals .

The use of Pilant's line source model , which is far from being ideal in representing the plasma source , is justified in two respects . The model accurately predicts the relative amplitude , polarity and form of the longitudinal and shear arrivals yielding a close fit to the "point " source directivities measured experimentally . Secondly the model is computationally simple , the combination of the two advantages offering a sound basis on which wide or array type sources may be based .

The directivity analysis based on Pilant's work , uses both the top-hat and apodized source functions to model the plasma source profile , with the non-uniform profile producing the closest agreement . This is as expected due to the variations in the optical power density across the beam profile , which is reflected in the plasma density . This analysis is not as complex or rigorous as

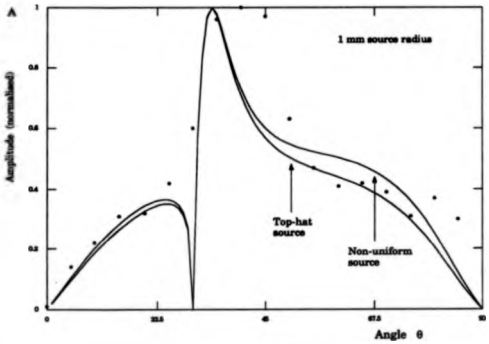
A
1 mm source radius
Amplitude (normalised)
Top-hat source
Non-uniform source
Angle θ

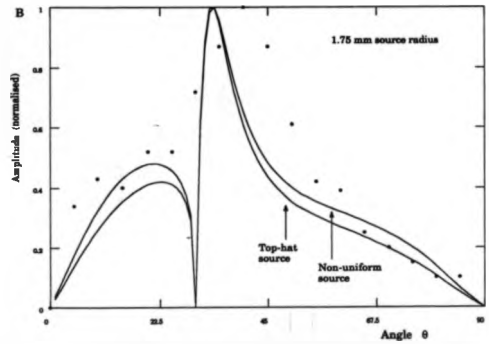
B
1.75 mm source radius
Amplitude (normalised)
Top-hat source
Non-uniform source
Angle θ

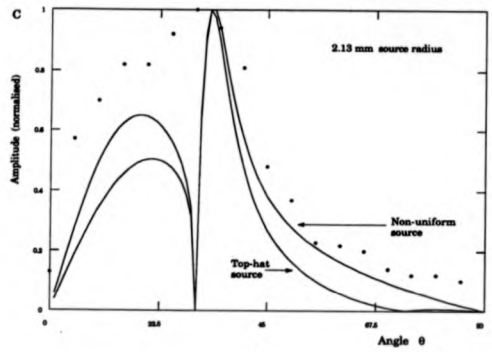

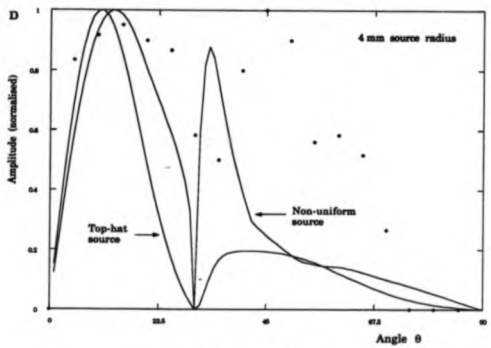

Fig 5.22 a , b , c & d Measured and theoretical shear wave directivities for a range of source radii .

the finite element approaches which are being increasingly used to model the ultrasonic directivity patterns [11] . However the degree of agreement achieved between this theory and experiment , with the ability to extend this approach to a range of spatial source profiles , may offer sufficient accuracy in modelling the wide source directivity that more complex analysis gives only slight additional information .

References Chapter 5

[1]J.D.Achenbach , "Wave Propagation in Elastic Solids" vol16 (North-Holland Publishing) (1973)
[2]W.L. Pilant , "Elastic Waves in the Earth " pp103-118 (Amsterdam:Elsevier 1979)
[3]L.F. Bresse , J. Appl. Phys. vol65 pp1441-1447 (1989)
[4]K. Kawashima , J.A.S.A vol60 pp1089-1099 (1976)
[5]D.C. Gachenheimer , J. Appl. Mech. vol17 pp99-110 (1971)
[6]D.A. Hutchins , R. Dewhurst & S.B. Palmer J.A.S.A. vol 70 no 5 p1362 (1981)
[7]G.F. Miller & H. Pursey , Proc. Roy. Soc (London) A223 521 (1954)
[8]J.T. Cherry , Bull. Seism. Soc. Am. vol 52 no 1 p27 (1962)
[9]A.E. Lord , J.A.S.A. vol 39 no 4 p650 (1966)
[10] E. Hect & A. Zajac "Optics" chapter 10 (Addison Wesley and Sons, New York ,1980)
[11]J. P. Weight , J. A. S. A. vol81 no 4 (1987)

Chapter 6

Non-Breakdown Ultrasonic Generation

The Thermoelastic Interaction

6.1 Introduction

In the initial discussion of chapter 3 the heating efficiency of 10.6μm radiation on metal surfaces was discussed as being very weak . The generation of thermal electrons was described as being reliant on the presence of thermally uncoupled regions of metal from which heat diffusion is greatly reduced . This chapter describes more fully the relative thermoelastic generation efficiency of 10.6μm to 1.06μm and shows the longer wavelength to be able to produce a measurable interaction . Previously Gaussian beam profiles have been obtained from the laser radiation sources of Nd:YAG and other traditionally used lasers , the diameters generally associated with such sources is being in the region of a few millimeters . Unless great effort is made such pulses always maintain their Gaussian profile . The CO_2 laser beam profile provides a excellent means of studying the effects of a wide non-Gaussian thermoelastic source . The results of bulk wave measurements are compared with the analysis of Bresse , who's work included the modelling of thermoelastic interactions . An understanding of the source profile is used to predict the form of the Rayleigh waves produced by the wide thermoelastic source generated by the CO_2 laser .

6.2 Temperature Rises in Metals

Classical electromagnetic theory may be used to give valid transmission and reflection coefficients for infrared radiation incident on metals . In the infrared range the wavelength is sufficiently long such that no selective electron-photon interactions occur . The radiation , which creates eddy currents within the metal , decays in amplitude by 1/e within a characteristic

skin depth , δe , of the surface . The absorption , T , and skin depth being given as

$$T = 2\sqrt{\frac{2\omega\varepsilon_o}{\sigma}} \qquad 6.1$$

$$\delta_e = \sqrt{\frac{2}{\omega\sigma\mu_o}} \qquad 6.2$$

where ω is the radiation angular frequency , σ the conductivity and μ_o and ε_o the permeability and permittivity of free space respectively , the expressions using the approximation $\mu_r \sim 1$ valid for non-magnetic metals . The above two equations show the absorption to increase with increasing frequency while the skin depth decreases . The absorption of 10.6μm radiation on metals is therefore reduced by a factor of $\sqrt{10}$ on that of 1.06μm giving typically 2% absorption . The skin depth for 10.6μm radiation ranges from between 10-15nm , being the instantaneous depth to which heat is generated . This initial heating , due to the large temperature differentials generated , is followed by rapid diffusion into the sample to the characteristic thermal skin depth , δ_t , [1] which for a pulsed heat source is given by

$$\delta_\tau = \sqrt{4\kappa\tau} \qquad 6.3$$

where κ is the thermal conductivity and τ is the laser pulse duration . Due to the duration of the laser pulse , of the order ~100 ns , it is clear that the thermal skin depth is much greater than the electromagnetic skin depth by several orders of magnitude , with δ_τ lying in the range , for a typical thermal conductivity of 0.98 cm^2s^{-1} for Al , of a few microns . Ready [2] used the differential heat flow equation , given in eq. 2.2 and produced a solution for an essentially one dimensional heat source , with non-instantaneous time duration , giving a temperature rise , θ ,of

$$\theta(x,y,z,t) = \frac{I_o S(x\,y)}{c\rho\sqrt{\kappa\pi}} \int_0^t \frac{\exp\left(\frac{-z^2}{4\kappa t'}\right)}{\sqrt{t'}} P(t-t')\,dt' \qquad 6.4$$

where S(x,y) is the spatial distribution of the radiation source , P(t-t') is an arbitrary temporal pulse profile , I_o the peak absorbed laser intensity , ρ the density and c the specific heat . Aindow [3] calculated the surface temperature rise obtained from a 30 ns , TEM_{00} pulse from a Nd:YAG laser with an energy of 2.5 mJ and a Gaussian radius of 0.3 mm obtaining a peak surface temperature rise of ~140° . This value is readily increased using higher laser energies , increasing the temperature up to and beyond the melting points of most metals , being 660° for Al , 1540° for Fe and 1084° for Cu .

The calculation for the surface temperature rise has been rerun for the CO_2 laser pulse . The temporal profile of the laser may be treated as a triangular function described by

$$I(t) = \frac{I_o t}{t_1} \qquad t<t_1$$

$$= \frac{I_o(\tau-t)}{(t-t_1)} \qquad t_1<t<\tau \qquad 6.5$$

where Io = 1.33×10^7 W for a total energy of 1J and τ=150ns gives a surface temperature rise in aluminium of ~140° using a value for the reflectance of 0.98 . As discussed in chapter 3 this value is a function of temperature and as such the value of 140° is a minimum estimate . Considering both the effects of increased absorption and a non-ideal surface gives a more realistic value of the surface temperature rise of ~200°-220° . Similarly pure iron and copper yield ideal temperature rises of 170° and 90° respectively , copper experiencing the lowest temperature rise due to its high thermal conductivity .

The result of these calculations shows that despite the increased reflectivity of the metal to 10.6 μm radiation and the longer pulse duration allowing diffusion to occur to greater depths , the 1J of energy supplied by the CO_2 laser is sufficient to produce comparable surface heating to that of the 3-5

mJ , Nd:YAG laser discussed earlier . Thus a significant thermoelastic interaction exists from which wide source ultrasonic measurements may be made .

6.2.1 Source Profiles

To determine the corresponding thermoelastic stress profile for a given radiation profile consider two adjacent volume elements within the irradiated area on the sample surface , shown in Fig 6.1 , where the volume elements are sufficiently small that uniform heating occurs throughout the element . The irradiated region , increase in volume as a result of which the two volume elements will exert thermally induced stresses on the adjoining faces . The resultant radial force , F , at the interface between the two elements may be expressed as

$$F = a*b(\sigma(r) - \sigma(r+\Delta r)) \qquad 6.6$$

where a and b are the width and depth of the elements (Fig 6.1) and σ is the thermally induced stress which is a function of the laser pulse profile and hence radial distance , r , from the centre of the source . The volume element and therefore Δr are sufficiently small that a Taylor's expansion may be carried out on the second term in eq 6.6 which yields , if only first order terms are retained

$$F = a*b\left(\sigma(r) - \sigma(r) - \Delta r \frac{d\sigma}{dr} \right) = - a*b\,\Delta r \frac{d\sigma}{dr} \qquad 6.7$$

The thermally induced stresses acting on each face of the volume element may be given as

$$\sigma_{ii} = -3\alpha_T K\theta(t) \qquad 6.8$$

where α_T is the coefficient of linear expansion , K the Bulk modulus and θ the time dependent temperature rise within the volume element . As the temperature rise is directly proportional to the incident energy from eq.6.4 ,

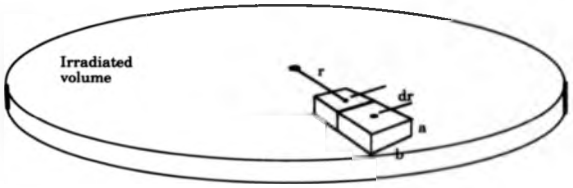

Fig 6.1 Diagram showing the volume elements within the irradiated sample region , for the determination of the thermoelastic source function for a given laser spatial profile .

then the force distribution is directly proportional to the spatial derivative of the radiation profile . This result was stated but not discussed by Bresse [5.3] in his consideration of the thermoelastic source and a similar analysis led Aindow [3] to use the differential form of the ultrasonic monopolar source function derived by Chao [4] and not the laser source distribution to model the effect of wide Gaussian laser sources .

Application of this result to a circular cross-section , top-hat laser source distribution of radius a , is to produce a circular ring source at r=a . This analysis shows there to be an acoustically dead region of the source for r<a , from which no ultrasonic contributions originate . The bulk waveforms originating from such a ring source were calculated by Bresse as well as those originating from the apodized source function . Fig 6.2 summerises the expected source distributions originating from the above two source types and also includes the expected thermally induced stress distribution from a Tukey profile laser source which closely models that of the CO_2 laser.

6.3 Bulk Waves

6.3.1 Theoretical Predictions

The epicentral displacement waveform generated by a top-hat thermoelastic source is shown in Fig 6.3 calculated for a 5 mm source radius on a 10 mm thick sample . There is no ultrasonic arrival at the expected transit time of a longitudinal wave directly through the sample , at time t_p . Instead the first arrival , $t_p(a)$ corresponds to a wave travelling from the edge of the source to the detector . The overall waveform structure , typified by the inward , step displacing longitudinal arrival and the arrival of the positive displacing shear wave being identical to that predicted by Rose [2.5] , who used a point source analysis , the exact form of which will be discussed in greater detail in the chapter 7.

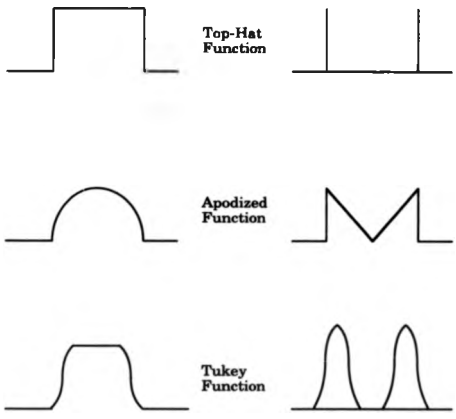

Fig 6.2 Laser and thermoelastic source profiles studied in the analysis of wide ultrasonic sources .

Fig 6.4 shows two on-epicentre waveforms calculated by the apodized source type , for source radii of 2.5 mm and 7 mm . Contributions from across the source with arrival times from t_p to $t_p(e)$, are observed as expected from such a source profile . The initial longitudinal arrival is instead of being a sharp step , spread in time between the plane and edge wave arrivals . Similarly the shear wave suffers an increase in risetime due to the summation over source components . The 7mm radius source shows how an almost total loss of initial longitudinal definition is observed for such a broad source type in a comparatively thin plate .

The third source type is that generated from the differential Tukey function which may be estimated by obtaining the ring source solution at the appropriate radius which corresponds to the peak in the differential Tukey function . The resultant ultrasonic waveform is calculated by carrying out a spatial summation over individual source contributions , using the weighting shown in Fig 6.2c . The results of this source type , shown in Fig 6.5 are calculated with the same laser pulse steepness , α_l . As expected the waves arrive at different times corresponding to the source width with the loss in longitudinal and shear wave distinction predicted by the finite source width . Increasing α_l , makes the source broader and therefore has a similar effect to that of the apodized source function used by Bresse , in producing source components from an increasingly large fraction of the irradiated region .

6.3.2 Experimental Results

To remove this effect and verify the effect of a well defined top-hat source , an adjustable aperture was used to produce circular thermoelastic sources of variable radii . Fig 6.6 shows two such waves recorded for 7 mm and 10 mm source diameter , the 10 mm waveform showing a delay in the longitudinal arrival compared to the smaller source wave . The waveforms show the shape of the wave to be maintained as predicted from such a top-hat source function .

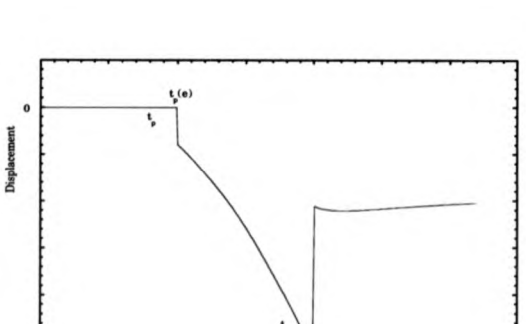

Fig 6.3 Thermoelastic epicentral wave derived from a top-hat profile laser source .

Fig 6.7 shows a series of interferometrically recorded , thermoelastic , on-epicentre waveforms whose source size was adjusted by varying the optical focusing conditions . The waveforms show a distinct shift in the arrival times of the initial longitudinal wave . As the extent of focusing is reduced , giving a wider source diameter , the source becomes broader as α_1 increases to its unfocused value of ~0.4 , which as described above results in the source profile becoming similar to that of the apodized source distribution of Bresse . A second effect which reduces the definition of the wave is due to the source profile being almost square resulting in its width varying by a factor of $2\sqrt{2}$, making the 7 mm source have components of 10 mm width .

The difference in the three source types , top-hat , apodized and Tukey is detectable and with careful timing measurements the difference between them is resolvable although the finite pulse duration , leading to a loss of signal definition , coupled with the non-ideal source function makes clear definition between the source types slight . A superior method by which the finite source size may be investigated is by the inspection of Rayleigh waves . Being surface waves they directly reflect the extent of the source and their comparatively slow velocity makes the experimental measurement easier although the effect of detector size becomes more important .

6.4 Rayleigh Waves

6.4.1 Theory

Chao [4] derived the outward displacement produced by an in-plane monopolar source , being described mathematically by

$$U(\bar{r},T) = \frac{\sqrt{6FT}}{32\pi^2\mu r}\left(6K(m) - 18\Pi(8m^2,m) - (4\sqrt{3}-6)\Pi(-(12\sqrt{3}-20)m^2,m) + (4\sqrt{3}+6)\,\Pi((12\sqrt{3}+20)m^2,m)\right) \qquad \frac{1}{\sqrt{3}}<T<1$$

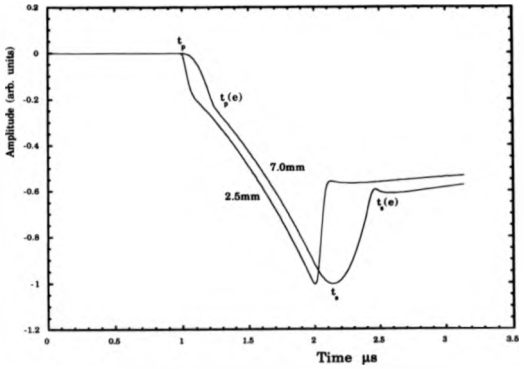

Fig 6.4 Thermoelastic waveforms derived from an Apodized laser spatial profile calculated for source radii of 2.5mm and 7.0mm , showing the plane and edge arrivals .

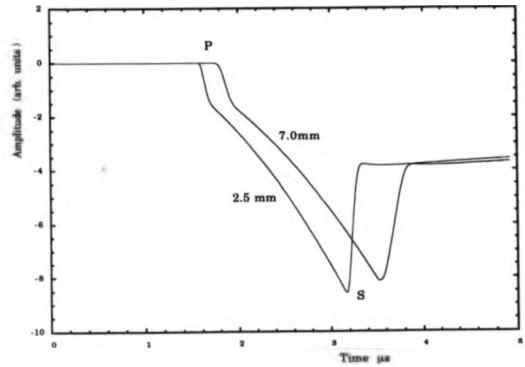

Fig 6.5 Thermoelastic waveforms derived from a Tukey function laser profile , for source radii of 2.5mm and 7.0mm .

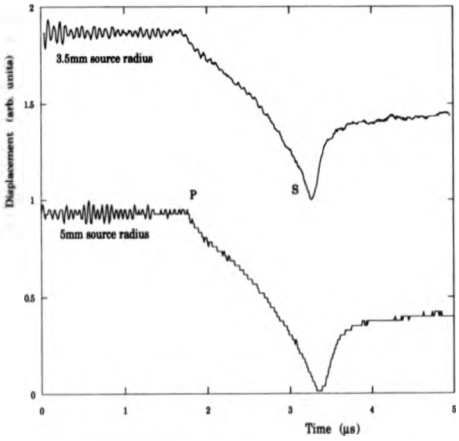

Fig 6.6 Interferometer measured epicentral displacements for a circular apertured , top-hat source function .

$$= \frac{\sqrt{6FT}}{32\pi^2\mu r}\left(6K(n) - 18\Pi(8,n) - (4\sqrt{3} - 6)\Pi(-(12\sqrt{3} -20),n) + (4\sqrt{3} - 6)\,\Pi((12\sqrt{3} + 20),n)\right) \qquad 1<T<\gamma$$

$$= \frac{\sqrt{6FT}}{32\pi^2\mu r}\left(6K(n) -18P(8,n)-(4\sqrt{3} - 6)P(-(12(3) - 20),n) + (4\sqrt{3} + 6)P((12\sqrt{3} + 20),n)\right) + \frac{FT}{8\pi\mu r(T^2 - \gamma^2)} \qquad \gamma< T \qquad 6.9$$

where Uz (r,T) is the vertical displacement at some time , $T = \frac{V_s t}{r}$ and distance r and F is the source magnitude with the following substitutions having been made

$$m = \frac{3T^2 - 1}{2} \quad , \quad n=\frac{1}{m} \quad , \quad \gamma=\frac{\sqrt{3 + \sqrt{3}}}{2}$$

and K(x) and Π(y,x) are standard elliptic integrals [5] . The solution which is given in three parts associated with the longitudinal , shear and Rayleigh waves , (Fig 6.8) , is characterized by the discontinuity at the Rayleigh arrival , and the subsequent slow decrease in amplitude . This solution has an angular dependence , measured away from the direct line of sight of

$$U(r,T) = U(r,T)\cos\theta \qquad 6.10$$

Chao's solution is for a Poissons ratio of 0.25 as compared to 0.33 for aluminium which leads to the relative wave velocities being different from those recorded experimentally , however the form of the displacement is effectively unchanged . For the analysis of Nd:YAG generated thermoelastic waves [6] , a bipolar stress of width δr has previously been considered . Therefore in any direction the surface wave is composed of two components , one from either side of the dipole , out of phase by π due to eq 6.10 . Thus as $\delta r \to 0$ the resultant wave is effectively the differential of Chao's solution . To obtain a wide source solution the differential Chao solution is convolved with a variable Gaussian source function [7] .

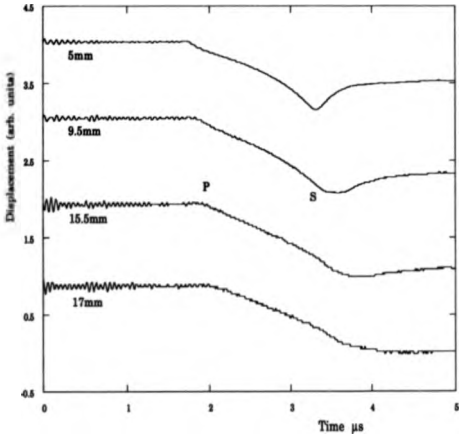

Fig 6.7 Series of displacement waveforms generated by unapertured , square cross-section CO_2 radiation for the source diameters given .

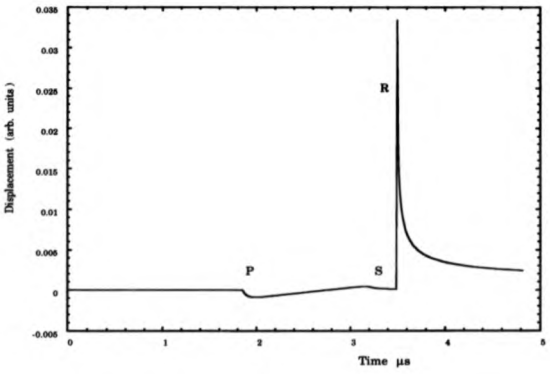

Fig 6.8 Chao solution for the surface displacement due to an in-plane monopole .

The source produced by the CO_2 laser , as described , has a non-Gaussian profile and is in general too large to allow such a differential approximation to be made . The resultant waveform from a large , several millimetres wide , top-hat source may be calculated by summing all source contributions from a ring of monopolar sources . Fig 6.9 shows the geometry of the source , being similar to that used be Copper [8] to estimate the source strength from a Gaussian profile , Nd:YAG source . An ultrasonic element at a point P on the ring source , will be observed at a point O , with a source strength which is dependent on the angle θ and the distance H . For a radius of R and a source-centre to detector separation D , H may be given by

$$H^2 = D^2 + R^2 - 2DR\cos\phi \qquad 6.11$$

Using the cosine rule within the triangle OPS and noting that $\cos\theta = -\cos\phi$, gives the angular dependence of θ as

$$\cos\theta = \frac{D\cos\phi - R}{H} \qquad 6.12$$

Thus H and $\cos\theta$ may be substituted into eq. 6.10 to give the form and amplitude of the wave at any point P on the ring source . The resultant waveform is obtained by carrying out a numerical summation of waves components around the ring and as the problem is symmetrical this summation may be carried out for $0 < \theta < 180$. Fig 6.10 shows the result of such an analysis for source widths of 7 mm and 9.5 mm . The surface longitudinal wave becomes less distinct and tends positive due to the source components from the far side of the source . The Rayleigh wave has an initial well defined outward displacing arrival , which then tends negative due again to the contributions from the far side of the source . After reaching a peak in inward displacement the surface relaxes back to zero displacement , as observed in the monopolar solution . As forecast the results of these calculations show the wave width to be proportional to the source width . The

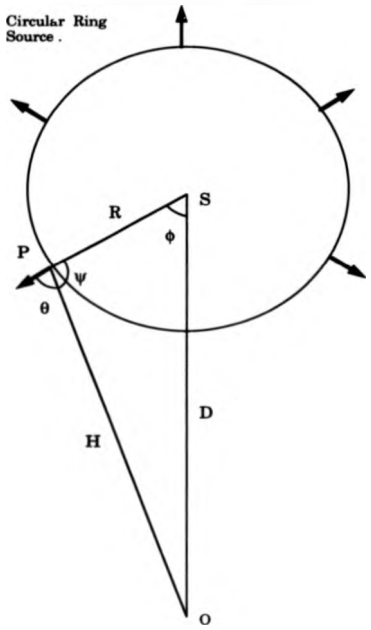

Fig 6.9 Circular ring source geometry for the calculation of source element strength and wave arrival time .

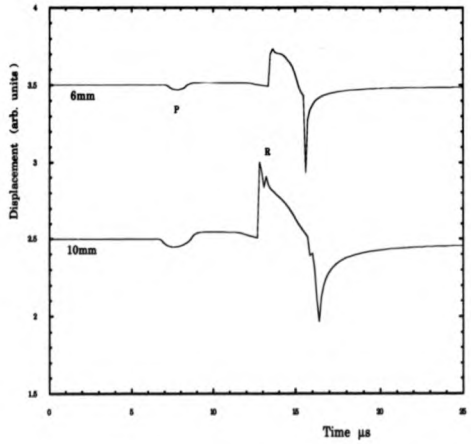

Fig 6.10 Ring source Rayleigh waves calculated for 6mm and 10mm source diameters .

small oscillations observed in the waveforms are due to the limited number of summations and the effect of adding a series of high frequency arrivals . Fig 6.11 shows the ring source theory waveforms convolved with a typical CO_2 laser source temporal profile , which as the waves were detected interferometrically , is the only limit on the bandwidth . The convolved waveforms show an expected loss of frequency content seen as giving the Rayleigh arrival a finite risetime .

6.4.2 Experimental Results

The experimental arrangement used in the generation and detection of wide source thermoelastic Rayleigh waves , was similar as for the top-hat bulk wave measurements , the radiation first passes through a variable width , circular aperture and is then focused . Due to the geometrical limitations of the interferometer size the radiation strikes the sample at an angle . This has the consequence of producing a slight variation in source strength across the irradiated area , however this variation is only generates a temperature gradient of a few percent insufficient to generate any significant source variations . Fig 6.12 shows a series of Rayleigh waveforms recorded for varying source sizes . The smallest width of 3.5 mm approaches the upper limit of the Nd:YAG source dimensions and the waveform has the appearance of a broad bipolar wave as predicted by Cooper [8] . As the source size is increased the resultant waveforms show close agreement with those generated from the above model . The relative amplitude of the longitudinal wave is seen to increase and become more bipolar with increasing source size . The Rayleigh wave shows as predicted , a sharp positive displacement followed by a gradual negative displacement resulting in a broad negative peak , the width of the wave agreeing well with the measured source diameter . The experimental data however shows a plateau in the Rayleigh motion . This may

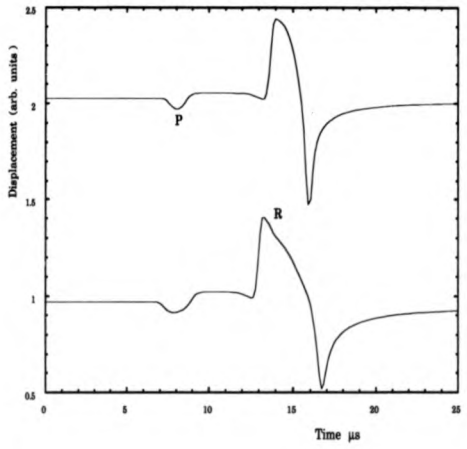

Fig 6.11 Ring source waveforms from Fig 6.10 convolved with the CO_2 temporal profile .

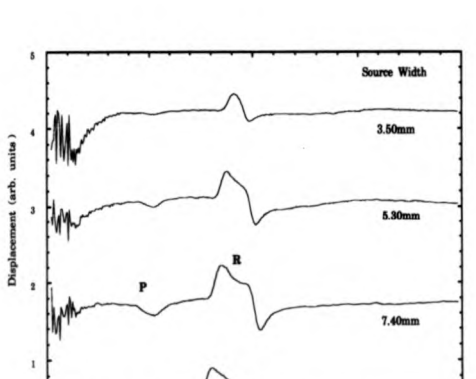

Fig 6.12 Series of experimental Rayleigh waves recorded with a top-hat source function for increasing source radius

be due to the non-exact Heaviside source time dependence which will increase the rate at which the post Rayleigh arrival falls in amplitude .

6.5 Conclusion

The analysis of the thermoelastic source as the differential of the radiation profile is shown to be correct . The wide source analysis by Bresse has been , in part , extended to include the differential Tukey source function which results in waveforms slightly different to those produced by top-hat and apodized source types . By far the most significant effect of the wide CO_2 laser source is on the Rayleigh wave which becomes almost separated into two individual monopolar arrivals instead of a broad bipolar pulse as obtained from a typical Nd:YAG source . The source strength , as shown from the surface temperature calculations , is very weak producing surface longitudinal displacements of only a few tenths of nanometers . This coupled with the broad source makes the CO_2 laser unsuitable for the generation of thermoelastic waves in metals in an NDT setting .

Surface Modified Sources

6.6 Introduction

The evaporation of a thin surface layer from the sample was described in chapter 2 as being a means of generating large amplitude ultrasonic transients . The interaction of 10.6 μm radiation with liquids is stronger than that of 1.06 μm radiation due to the enhanced infrared absorption , which manifests itself as a large reduction in the absorption depth resulting for the longer wavelength radiation . The use of overlying liquid media on a metallic surface is examined in terms of liquid type and thickness and the resulting source strength and ultrasonic waveform structure . The large radiation spatial profile is again used to complement the wide source thermoelastic data

and to extend the initial plasma induced , normal force , wide source study described in chapters 4 and 5 .

6.7 Calculation of Induced Surface Pressure

Assume first the case of uniform absorption of heat , H throughout a liquid . A temperature rise θ will result due to the input of energy , the two being simply related by

$$H = mc_l\theta + mL + mc_v\theta \qquad 6.14$$

where m is the mass of liquid irradiated , c_l and c_v the specific heats of the liquid and vapour respectively and L is the latent heat of vapourization . This reduces to $E_T = mc_l\theta_b + mL$ for the energy required to reach the boiling point , where E_T is the transmitted energy required for a phase change . The surface force , F , induced by the action of such evaporation is given by

$$F = \frac{dp}{dt} = Ve\frac{dm}{dt} \qquad 6.15$$

where p is the momentum of the ejected liquid and Ve the ejection velocity . Substitution of eq.6.15 into eq. 6.14 and equating dt=τ the laser pulse duration , being the timescale of the reaction gives

$$F = \frac{VeE_T}{\tau\,(L+\theta_b c)} \qquad 6.16$$

and the pressure is simply inferred from eq 6.15 as

$$P = \frac{W_T Ve}{(L+\theta_b c)} \qquad 6.17$$

where W_T is the transmitted power density . This result was derived by Rudd [9] , although he assumed the latent heat of vapourization to be far greater than the heat required to elevate the liquid temperature , which is not the case

for volatile liquids as demonstrated later in this chapter . The ejection velocity may be calculated by considering the average kinetic energy of the liquid molecules due to heating , which from thermodynamics is given as

$$\frac{1}{2} k_B \theta_b = \frac{1}{2} m_m V_{-z}^2 \qquad 6.18$$

where k_B is Boltzmann's constant , m_m the molecular mass and V_{-z} is the component of the velocity away from the target surface such that $V_{-z} = V_e$. Therefore the delivered surface force may now be fully defined as

$$F = \frac{E_T}{\tau (L + \Theta_{bc})} \sqrt{\frac{k_B \Theta_b}{m_m}} \qquad 6.19$$

This analysis neglects the effect of heat diffusion throughout the liquid and target material as such effects are small on the timescales of interest . This analysis for a uniform heating is also independent of liquid depth and gives the same result regardless of geometry , such that the heating and subsequent force developed due to evaporation is independent of the depth and area of the overlaying liquid . However 10.6μm radiation is absorbed strongly in liquids and decays in amplitude exponentially from the liquid surface in a typical Beer's law decay , giving a temperature profile as a function of depth , z , into the liquid of

$$\theta = \theta_o \exp(-\alpha z) \qquad 6.20$$

where θ_o is the surface temperature and α is the absorption coefficient of the liquid , which for water is 0.087 μm^{-1} . Thus for all but liquid layers less than a few microns thick , the uniform absorption method is invalid . A full description of the temperature profile as a function of depth for a given input energy may be obtained by solving the differential heat flow equation for the relative source and boundary conditions . This has been analyzed elsewhere by Sigrist et. al. [10] , who considered the case of a Gaussian beam penetrating

a liquid . Such complete analysis is not however required for this work as only an estimation of the degree of vapourization is required to discuss the magnitude of the pressure exerted onto the sample . The energy , E(d) , absorbed within a depth , d , of the surface may be given by

$$E(d) = E_T[\exp(-\alpha z)]_d^0 \qquad 6.21$$

which gives a value of 0.34 J absorbed within one half absorption depth , allowing for a transmission coefficient of 0.96 , a value which accounts for air-liquid loss and reflector losses . Rearranging eq 6.14 and substituting $m=\rho Ad$, where A is the area of irradiation and ρ the liquid density , gives the maximum area , A_{max} , which is able to produce evaporation to $\alpha/2$ as

$$A_{max} = \frac{2E_T(\alpha/2)}{\rho\alpha\,(L + c_l\Theta_b)} \qquad 6.22$$

which for $L= 2{\cdot}10^6$ Jkg^{-1} , $\rho= 998.2kgm^{-3}$, $c_l= 4.2{\cdot}10^3$ $Jkg^{-1}C^{-1}$, gives A_{max} of $\sim 26mm^2$ corresponding to a source width of ~5mm . Thus the incident power density required for this level of evaporation is $\sim 3.7{\cdot}10^7$ Wcm^{-2} , which is well below the required threshold for gas breakdown . Increasing the power density will increase the vapour energy and the depth to which evaporation will occur , thus increasing V_s and Δm respectively , both of which will increase the source strength . This analysis gives a pressure of ~550 N , which is approximately eight times greater than the peak surface plasma pressure of 65 N calculated in chapter 4 and eight times lower than that calculated above . This estimation however drastically simplifies the analysis as it gives only a mean value of the ejection velocity and the mass of material ejected and therefore should not be treated as a general description , but as an order of magnitude calculation for the prediction of source strength .

6.7.1 Experimental Arrangement

Fig 6.13 shows the experimental arrangement used to measure the ultrasonic transients generated on surface modified targets . The CO_2 radiation is reflected through 90º by a polished , mirror quality , brass plate making the experiment lie in the vertical plane . The radiation is focused onto the surface of a polished aluminium target , the mirror quality of the which suppresses breakdown allowing a range of source sizes down to 1mm wide and incident power densities up to a maximum of $\sim 10^{+9}$ Wcm^{-2} to be achieved . To facilitate a liquid layer of variable depth above the sample , a perspex cell was bonded onto the sample surface , the liquid being inserted by a calibrated pipette to ensure accurate measurement of liquid volume . Two liquids , water and ethanol , were used as surface modifiers . To produce a uniform water layer a small amount of detergent was added to break the surface tension , this additive being insufficient to change the bulk properties of the water . Due to the large peak amplitude of the ultrasonic transients generated in this manner , interferometric detection may not be used due to the non-uniformity of the device in response to large amplitude displacements . Detection of epicentral waves was made via a longitudinal sensitive EMAT , the active area of the EMAT coil was reduced by a aperturing with a thin brass shim to ensure that the preamplifier was not saturated and provided a linear output .

6.7.2 Wave Structure

As the radiation intensity on a liquid surface decays in amplitude according to Beer's law , the depth to which evaporation occurs will be dependent on the incident power density . This is also true of the thermoelastic generated which , if the liquid depth is sufficient , will always accompany the evaporative source . Fig 6.14 shows a series of ultrasonic transients generated by a $0.16mm^2$ beam of power density $10^7 Wcm^{-2}$, for increasing liquid depth . At such relatively low power densities the thermoelastic interaction is the

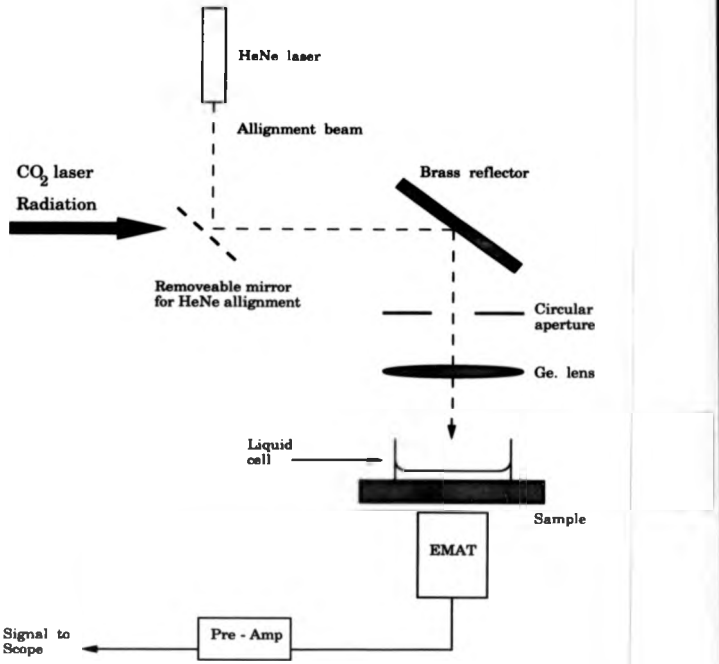

Fig 6.13 Experimental arrangement for measuring the effect of liquid overlays on metal targets .

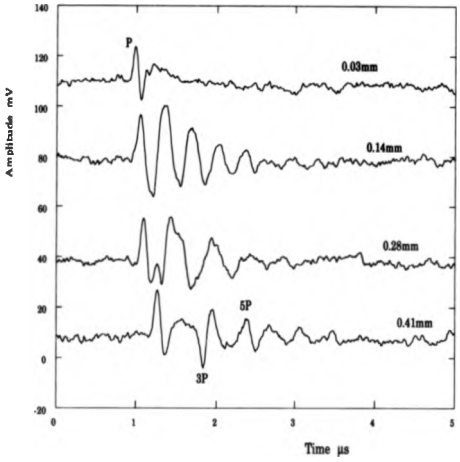

Fig 6.14 Longitudinal waveforms recorded for varying liquid thickness overlays . Lens-sample separation of 11cm . 9.50cm focal length lens .

dominant source of ultrasound . As predicted by Sigrist [10] the displacement pulse is monopolar , which is differentiated by the action of the EMAT . From similar work of Aindow [7] the differential pulse should have a risetime , R_T , between the 10% and 90% levels , of

$$R_T = \frac{2.2}{\alpha V_p} \qquad 6.23$$

where Vp is the longitudinal velocity in the liquid . The measured risetime of 58ns therefore corresponds to an absorption depth of 34μm , this measurement must however be dominated by the CO_2 laser pulse risetime . The polarity of subsequent arrivals is seen to alternate due to the phase change on reflection from the surface of the liquid . As the liquid depth decreases the subsequent arrivals begin to merge and the arrivals are seen as a series of unresolvable oscillations and eventual cancelation leaves only the first arrival visible . The longitudinal arrival time shows the wave to originate from the surface of the liquid rather than from the metal surface .

Fig 6.15 shows a second series of waves recorded under the action of a 1mm square beam of power density of $8.5 \cdot 10^8$ Wcm^{-2} . At the depth of ~0.03mm a single predominantly monopolar wave is observed , which is derived from a strongly evaporative source . The presence of a negative going component in the tail of the longitudinal arrival is seen to be depth dependent . At low liquid depth , where the arrival time is that of the aluminium target transit time , the waveform corresponds to the differential of a purely surface generated force , a point which is considered more fully later in the chapter . For larger liquid depths , where the ultrasonic source is a finite distance from the target surface the negative component will also have contributions from reflections within the liquid layer produced by both source types . However the violence of the interaction will strongly perturb the liquid surface and the reflected wave will be greatly reduced in coherence lowering its amplitude and definition .

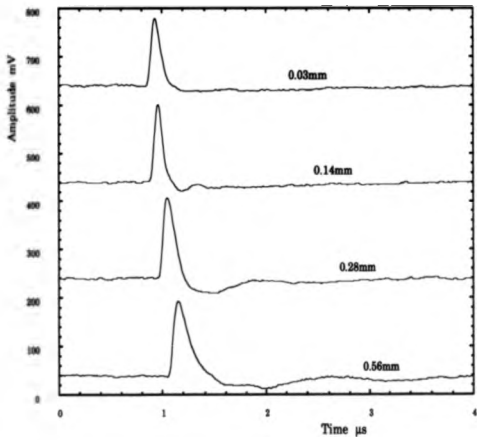

Fig 6.15 Longitudinal waveform variation for increasingng liquid thickness overlaya . Lens - sample separation of 9.5 cm .

The monopolar nature of the detected wave generated from a strong evaporation indicates the source to be Heaviside in time . This contrasts strongly with the expected delta function time dependence from the ejection of a thin liquid layer and may indicate the continual evaporation of liquid for times of the order or longer than the laser pulse duration and as will be discussed later is also a source size effect .

The graph in Fig 6.16 shows the amplitude of the evaporative longitudinal wave as a function of increasing depth for power densities of $9.6 \cdot 10^6$ and $2.4 \cdot 10^6$ Wcm^{-2} . Both sets of data follow the same behavior for thin layers of water , below 0.06mm , showing the ultrasonic amplitude to increase from zero to a maximum after which the amplitude stays approximately constant as the source composition of evaporation plus thermoelastic remains fixed with the peak amplitude occuring at a greater depth for the high intensity source as the higher power is able to evaporate material to a greater depth . Therefore the peak corresponds to a maximum depth to which evaporation may occur and as such is power density dependent . The near linear increase in ultrasonic amplitude at the low liquid depths indicates the uniform heating model to be valid in this region .

This interpretation is supported by timing measurements of the first arrival , which are shown as a function of liquid depth in Fig 6.17 for the two power densities used above . The higher of the two power densities shows the first arrival to occur at the through transit time of the aluminium target , up to a liquid depth of 0.09mm , showing the liquid to be evaporated through its bulk and agrees with the analysis of the above data . Above this depth the ultrasonic arrival time increases linearly . The lower power density measurements show the arrival time to be greater than the target transit time , indicating that the ultrasonic wave originates from the liquid surface for depths above ~0.03mm . Above a depth of 0.09mm the gradients of the two curves are equal , separated by a time which must represent the difference in depth to which significant

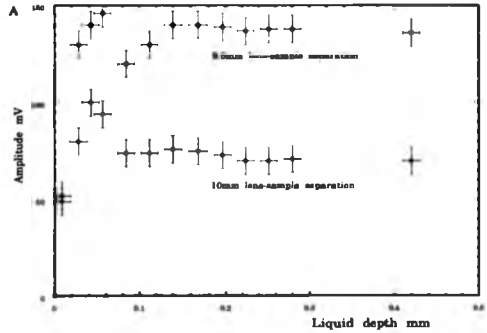

Fig 6.16 Amplitude variations measured for increasing liquid depth .

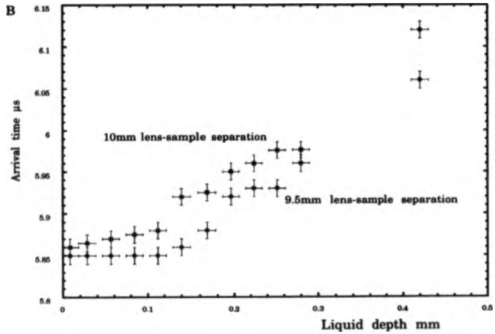

Fig 6.17 Arrival times of ultrasound for increasing liquid depth .

ultrasound may be produced for the two power densities . A difference of 25ns corresponds to 37μm , indicating that ultrasound is generated to a level well in excess of the optical absorption depth . This data is not reflected in the risetimes of the ultrasonic pulses as they are determined predominantly by the depth to which liquid is removed . The higher power density source has a longer risetime by a factor of 1.2 ,corresponding to a depth of 14 μm , over that achieved by the less intense source .

6.7.3 Source Strength

In an attempt to verify the absolute and relative predictions of eq 6.16 the ultrasonic amplitude was measured for both water and ethanol overlying liquids , and compared with plasma breakdown source measurements . To be able to make a valid estimation of the forces produced at the surface the epicentral displacement must be known . As the interferometer is unable to be used , on all but with the thinnest overlying liquids , a method of signal amplitude comparison was be used on results recorded with an EMAT . This requires measurement of the ultrasonic signal amplitude produced using a plasma source and comparing this to known interferometrically recorded displacements , as a means of calibrating the EMAT output . These measurements are then compared to results derived from surface modified sources .

To verify the material dependence the amplitude measurements within the purely evaporative regime were repeated using ethanol as the overlying material . Ethanol is a highly volatile liquid , having a low boiling point of 78.6C , heat of vapourization of $3*10^5$ Jkg^{-1} and specific heat of $2.34*10^3$ $Jkg^{-1}C^{-1}$

These properties yield a value for the required power density to deliver a standard surface force to be approximately three times lower with ethanol than water . Due to the strong directivity modifications produces by source size variations , the measurement of the above factor should be carried out at

constant source size , varying the incident energy . This experiment is difficult to perform accurately as the liquid depth must be varied such that all the available energy is converted into ejection material , avoiding thermoelastic interactions . The attenuation of the beam is discreet due to the limitations of the filters available , enhancing to the difficulty of making accurate measurements . An experimental figure of 2.5±0.7 decrease in incident energy was measured to deliver a constant source amplitude on ethanol as for water . This value is within that calculated above although an error factor of 36% is rather large .

Comparison of the evaporative source to the pure breakdown source strengths falls into two categories . Firstly the evaporative source produces large ultrasonic amplitudes with power densities well below those required to produce air breakdown making relative comparison impossible . Within the range of power densities required for breakdown , the signal amplitudes produced by the plasma source and evaporative sources have different dependencies with power density . The ultrasonic amplitude from an evaporative source being recorded at the power density required to produce a well defined L P source , resulting in a factor of 4 enhancement over the L P source .The peak force delivered from a L P source being 65N indicates that the force derived from the liquid layer boiling-off to be approximately 260N , which is an order of magnitude lower than the predicted value of ~1900N obtained from eq.6.16 . It may be assumed that the presence of a liquid vapour above the target surface will act as a filter to the incoming radiation . Thus a proportion of the incident energy will be absorbed within the vapour reducing the total energy input into the liquid .

If the mirror quality target is replaced by one having an ordinary machined surface , removing the suppression of breakdown a mixed evaporative/ablative source is produced . Fig 6.18a shows the experimental arrangement used to measure the amplitude variations with and without the

Fig 6.18a

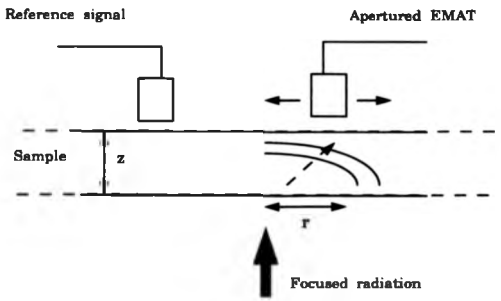

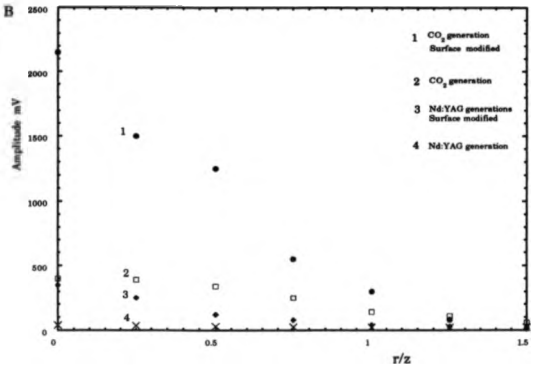

Fig 6.18 a , b Experimental arrangement and results for both CO_2 and Nd:YAG laser sources with and without surface modification .

presence of a modifying liquid , the results being shown in Fig 6.18b . The graph shows the source amplitude variations as a function of angle off-epicentre obtained with the CO_2 laser and for comparison similar results from a 30mJ Nd:YAG laser are shown . The on-epicentre measurements show a five-fold increase in amplitude obtained from a mixed source over a pure breakdown source . The exact weighting of the two source contributions is indeterminable due to the liquid being able to produce a rapid supple of thermal electrons from which breakdown may be seeded and hence less laser energy is involved in heating the metal . The graph also shows the amplitude variations with increasing angle off-epicentre . The rate of amplitude decay is much greater for the mixed source than for the pure breakdown source , which by $\sim 50^{o}$ off-epicentre have the same amplitude . The strong peaking in the ultrasonic energy was shown in chapter 5 , to be a result of increased source radius - frequency product . Thus either the effective source size is increased or the frequency content of the ultrasound is increased . Risetime measurements show no appreciable increase in frequency content , leading to the suggestion that the source size is increased . As the ultrasound pulse width measurements of chapter 5 showed the breakdown area is smaller than the irradiated area by a factor of ~0.5-0.6 a factor which may account for the change in directivities .

The Nd:YAG results showed a similar enhancement in on-epicentre amplitude and directivity . The enhancement of the directivity is , although not as pronounced , still present and may again be due to the increased source size

In the ablation of irradiated material the power density must be sufficient to increase the temperature through the melting and vapourization temperatures and their associated latent heats . Thus only the centre portions of the beam are able to generate such a temperature increase while in the evaporative source the heat input required for the production of a vapour is greatly reduced resulting in a wider source .

6.8 Interferometric Waveform Analysis

As observed in Fig 6.15 the waveforms detected by the EMAT under the action of an evaporative source are essentially monopolar , indicating that the surface source approximates to a Heaviside function . This contrasts strongly with the expected impulsive source giving an epicentral displacement corresponding to the second time differential of Knopoff's predicted displacement , shown in Fig 4.1 . However this wave is derived from a point source whereas the CO_2 laser source has a radius ranging from 0.5mm to 5mm . Secondly the time duration of the source may not be impulsive due to continual evaporation of liquid and the formation of a pressurized gas above the sample which continues to exert a pressure on the surface . The resultant waveforms will therefore be a sum of source elements across the width of the beam , subsequently convolved by a suitable temporal history .

As shown in Fig 6.16 a very thin liquid layer will produce a weak evaporative source on which the interferometer may be used to detect the ultrasound . The typical displacements produced by such a source being ~19nm , yielding a linearity from eq.2.18 , of 0.97% and therefore the peaks corresponding to the longitudinal and shear waves give a faithful description of the actual surface displacement . The liquid layer was applied with a damp swab and allowed a short duration to flow vertically down the sample in an attempt to produce some form of standard source . The liquid thickness will not affect the source size but may affect its time duration , resulting in a variability in the displacement , an indication of this will be given in the course of this section .

Fig 6.19 a,b,c shows a series of epicentral waveforms recorded on a 5mm thick , aluminium sample with source radii of 0.75 , 1.75 and 2.2 mm respectively . The choice of a thin sample ensures that the source width to

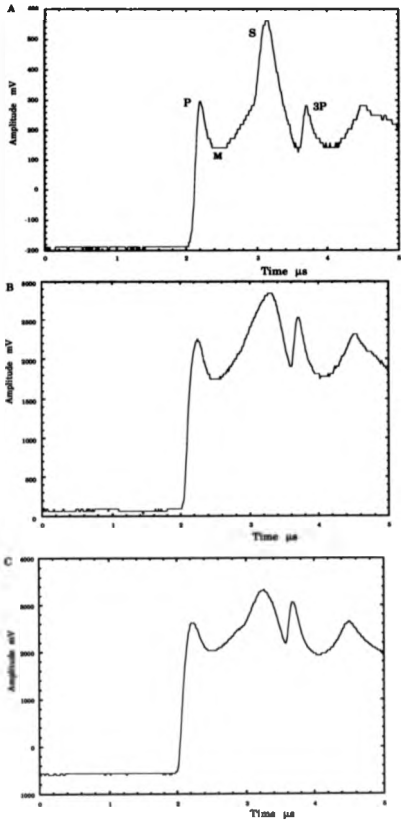

Fig 6.19 a , b , c Epicentral displacement waveforms for source radii of 0.75mm , 1.75mm and 2.2 mm respectively rscorded on 5mm thick Al. sample .

sample depth ratio is large while keeping the source dimensions within the uniform region of the beam profile , ensuring a near top-hat source type . The data shows several trends associated with the increasing source dimensions . The minimum point , labeled M , between the longitudinal and shear waves , shifts away from longitudinal arrival with increasing source size . A general loss of wave definition is observed and accompanied by a decrease in the ratio of the longitudinal to minimum displacements and also the ratio of the longitudinal and shear displacements . To enable inspection of the latter portions of the shear wave , which on the 5mm sample is masked by the multiply reflected longitudinal wave , a 10mm sample was used . Fig 6.20 shows the corresponding measurement to that in Fig 6.19b , having the same source width to sample depth ratio . The tail of the shear wave is seen to extend to times considerable later than the initial shear wave arrival . Comparison of these two waveforms shows the typical fluctuation in displacement due to variations in the source .

6.8.1 Theoretical Predictions

Fig 5.5a shows the from of the epicentral ultrasonic displacement derived from a top-hat , impulsive source , which as discussed may be described in terms of plane and edge waves . The shear wave only originates from the edge of the source and is seen as a discontinuity in displacement , while the longitudinal components originate from across the whole source , resulting in a wave who's width is directly proportional to the source radius . Fig 6.20 shows the shear wave to have a gradual decrease in displacement rather than a step , having a fall time of 0.54μs a value which represents the source duration . The temporal history of the source may be completed by noting longitudinal risetime , being 50ns . Fig 6.21 a shows the result of convolving a 3.25mm radius source solution with the temporal source duration described above and shown in Fig 6.21b , on a 10mm thick sample . The overall wave

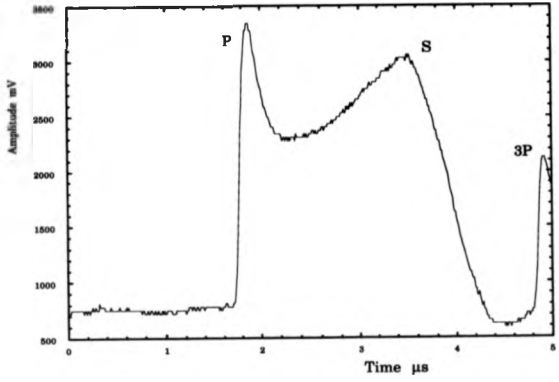

Fig 6.20 Epicentral displacement waveform for source radius of 3.25mm , sample thickness 10mm .

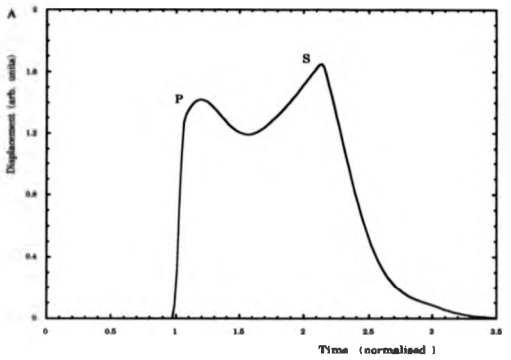

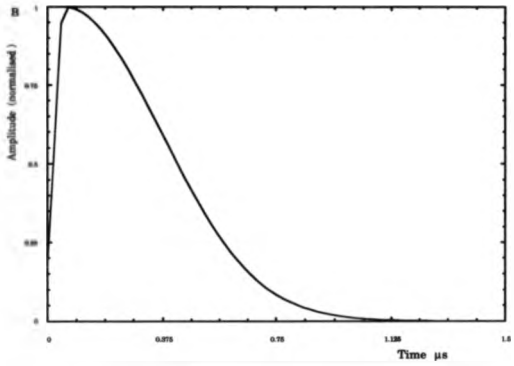

Fig 6.21 a& b Theoretical epicentral displacement for a 3.25mm source radius on a 10mm thick sample with the temporal profile of the source

structure gives good agreement lying between the experimental waveforms of Fig 6.19b and Fig 6.20. The predicted waveform displays the increased extent of the shear wave and the general loss in definition in the longitudinal and shear arrivals , although the width of the longitudinal wave is increased beyond that obtained experimentally . This discrepancy is not accounted for by considering a non-uniform source distribution which produces an almost identical result upon convolution .

The sensitivity of the theoretical resultant acoustic waveform to the initial source width and temporal convolution is examined to estimate the effect of source parameter variations . Fig 6.22 shows the resultant waveform for source radii of 0.75mm , 0.80mm and 0.85mm , convolved with above temporal source profile . The minimum point , M , moves towards the longitudinal arrival while the energy shifts from the initial longitudinal arrival to the shear arrival , as observed in Fig 6.19 .

Conversely Fig 6.23a shows the theoretical predicted waveforms for a range of source time durations given in Fig6.23b . Increased source duration results in the loss of a distinct longitudinal arrival and the minimum point both moves towards the shear arrival which increases in amplitude . The results of Figs 6.22 and 6.23 representing the spatial and temporal source extent , result in the loss of point like waveform structure . The figures show that the shear wave duration is determined almost totally by the temporal source duration alone , while the other main waveform changes , such as the longitudinal and shear wave amplitudes are produced by both source spatial and temporal contributions making deconvolution of the two effects difficult .

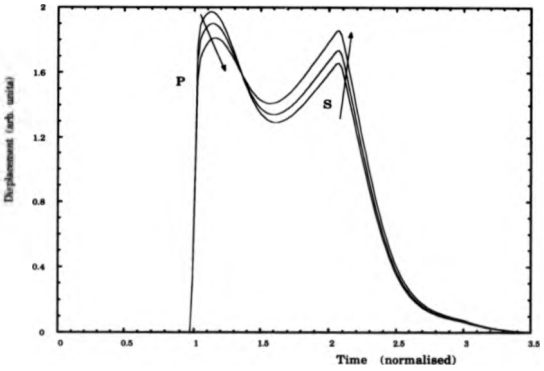

Fig 6.22 Series of epicentral displacement waveforms for varying source radius. Arrows show the effect of longitudinal and shear arrival position for increasing source size. Temporal profile as for Fig 6.21

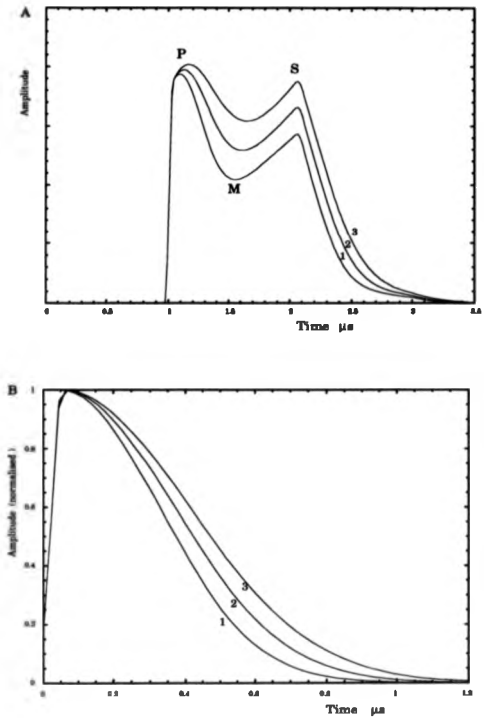

Fig 6.23 a & b Convolved wide source waveforms and the respective temporal source profiles .

References Chapter 6

1E.U. Condon , "Handbook of Physics" , chapter 5 (E.U. Condon & H. Odishaw , McGraw Hill , New York 1968)
2J.F. Ready , J. Appl. Phys , vol36 no2 pp462-468 (1965)
3A. Aindow , Ph.D Thesis chapter 4 Hull University (1988)
4C.C. Chao , J. Appl. Mech. vol27 pp559-567 (1960)
5 M.R. Spieqel , Schaum's Outline Series in Mathematics (McGraw-Hill Book Company 1973)
6 D.A.Hutchins , "Physical Acoustics" (Ed. W.P. Mason & R.N. Thurston , Academic Press , London) vol18 (1988)
7A. Aindow Ph.D Thesis chapter7 , Hull University (1986)
8J. Copper , Ph.D Thesis chapter4 , Hull University (1985)
9M.J.Rudd , Rev. Prog. Quant. NDE vol 2B (1983)
10 M.W. Sigrist & F.K. Kneubuld , J.A.S.A. vol64 no.6 (1978)

Chapter 7

Ultrasonic Generation in Non-Metals

7.1 Introduction

The ability to generate ultrasound non-destructively in non-metals using lasers is highly desirable if the role of such a technique is to be extended . Nd:YAG generation of ultrasound in non-metals has not proved to be widely successful . The range of such materials which are absorbing to 1.06μm radiation is relatively low and often depends on an additive pigment to absorb the radiation rather than the base material itself . The varying degree of absorption is also reflected in the wide variation in source types . Strong absorption will result in a point or two-dimensional source , while a low degree of absorption give rise to a weak cylindrical source type . The difficulties encountered with this method are reflected in the small number of publications discussing the laser technique as a means of generating ultrasound in non-metals . Radiation at 10.6μm is sufficiently far into the infrared that strong absorption occurs in almost all non-metals , over length scales of microns to several hundred microns .

The work presented in this chapter studies the interaction of 10.6μm radiation with two non-metals , glass and perspex which have significantly different optical and acoustic properties . The ultrasonic generation interaction falls into three main categories , thermoelastic , $<10^7$ Wcm^{-2} , evaporative , $(1\text{-}5)\times10^7$ Wcm^{-2} and above these power densities plasma breakdown is achieved . The distinction between the interaction processes is low , the thermoelastic interaction being the only pure source , while the other source types are a linear superposition of thermoelastic and either evaporative or plasma source types . These regimes correspond to 1.06μm radiation interacting with metals , however the strong coupling of CO_2 radiation with non-metals results in a stronger thermoelastic source when compared to the 1.06μm radiation-metal

case and as such the relative weighting of source components is changed . The generation process is discussed in terms of the source function , of which much recent work has been carried out and the damage thresholds of the material .

7.2 Experimental Arrangement

The requirements for examining non-metals are essentially identical to those used on metal samples , Fig 7.1 showing the experimental arrangement used in this work . Variation of the source size and incident radiation energy is achieved in the usual way with a variable radius ,circular aperture and filters. Both the interferometer and EMAT used to measure the ultrasonic transients require that a thin aluminium coating is evaporated onto the detection side of the sample . In the case of the interferometer detection on smooth non-metals may be carried out without any metallic coating , since the ~4% reflection from the glass or perspex is sufficient for stabilization of the device . However the large amplitude of the ultrasonic displacements generated using the CO_2 laser, requires the interferometer to have large dynamic range to ensure a true linear response , this condition therefore calling for the application of a metallic coating . The EMAT detector , required to measure the larger displacements where the interferometers dynamic range is insufficient even with a coating , is unable to operate on non-metals as it relies on the Lorentz interaction , a condition which is met by the presence of the metallic coating . This layer must be sufficiently thin such that multiple reflections of the ultrasound in the layer do not distort the detected signal . Throughout the course of these measurements the laser pulse was generated using the reduced nitrogen gas mixture , removing any double pulse effect and greatly reducing the degree of material heat damage .

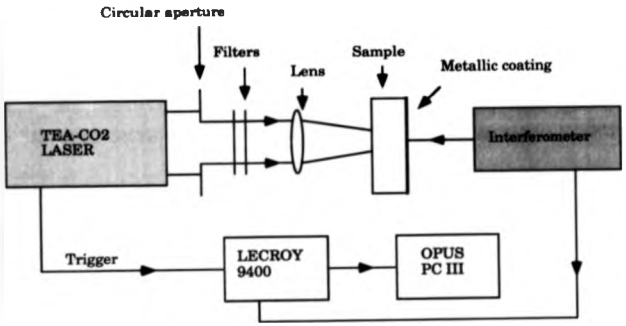

Fig 7.1 Experimental arrangement used to inspect non-metals

7.3 The Thermoelastic Interaction

Aindow [6.7] modelled the interaction of an optically penetrating light source within a medium . As the source width extended over a surface area far greater than its depth a one dimensional model was assumed . The radiation penetration profile is modelled by a Beer's law decay within the solid , which is valid for non-scattering materials having a low thermal diffusion , such that the source profile is constant over timescales of the laser pulse . Thus the temperature profile may be given by

$$T(z,t) = T(0,t)\exp(-\alpha z)\,H(t) \qquad 7.1$$

where H(t) is the Heaviside source function initiated at time t=0 , T(0,t) is the surface temperature and α the optical absorption coefficient . The optical absorption coefficient is not a fundamental material constant and is defined by $\alpha=4\pi k'/\lambda$, where k' is the absorption index or extinction coefficient which is however a material constant within the bounds of the infrared spectrum and λ is the wavelength of the incident light . Thus as the wavelength increases α decreases and the light penetrates further into the material . The resultant source gives the predicted waveform shown in Fig 7.2 from such a 1-D source type and appears as a monopolar arrival with a maximum corresponding to the travel time from the surface of the sample where the source is strongest . This case is directly analogous to the case of laser generation of thermoelastic waves in liquids considered in the previous chapter . As before the risetime , R_T , measured between the 10% and 90% levels is given as $R_T=2.2/\alpha V_p$ a figure which is proportional to the transit time across the heated region . This one dimensional analysis produces no shear wave components and the observed wavetrain is comprised only of a series of longitudinal reflections .

Chang and Sachse [1] discussed a thermoelastic source , which penetrates the sample with the above temperature distribution , as being a sum

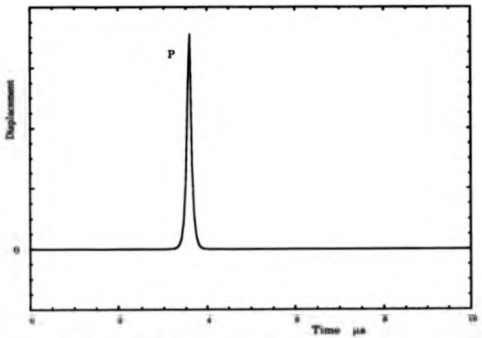

Fig 7.2 Predicted epicentral displacement using a simple 1-D analysis .
V_p=2790 ms^{-1} , α=150 μm , sample depth 10mm . [after Aindow]

of weighted source components . The authors chose as their initial Greens function the surface thermoelastic source solution derived by Rose [2] . The resultant waveform shows no outward displacing component as predicted by Aindow and has the appearance of Bresse's solution for a wide non-uniform source shown in Fig 6.4 . The spread in source positions leads to a corresponding spread in arrival times and a loss of definition in the resultant waveform .

An exact solution to the problem was determined , during the course of this work , by Conant and Telshow [3] who considered both one and two dimensional problems . The one dimensional problem agrees with that of Aindow [6.7] , predicting a single outward displacing monopolar arrival comprising of waves travelling directly from the heated source region and waves reflected from the top surface of the sample with a phase change of π , back towards the detector . This work was extended to a two dimensional model, the source having both the Beer's law decay into the sample and a Gaussian beam profile . The solution of the elastic problem was via the Laplace-Hankel transform technique to solve the temporal and spatial distributions respectively. Fig 7.3 shows the comparison between theory and experiment achieved by the above Conant and Telshow . The epicentral waveform is derived from a Gaussian source width of 1.16 times the sample depth and an optical penetration depth of 11% of the sample thickness . The agreement between theory and experiment is close showing the initial positive displacing precursor followed by a negative going component of the longitudinal wave and a broad shear arrival produced by the wide source . The experimental wave was detected with a flat plate capacitance probe who's size , not discussed by the authors , must be responsible for a degree of reduction in signal resolution. The presence of the positive precursor has different origins in the optical case than in the case of heat diffusion within metals . Both originate from source contributions below the sample surface , however in the optical case the source

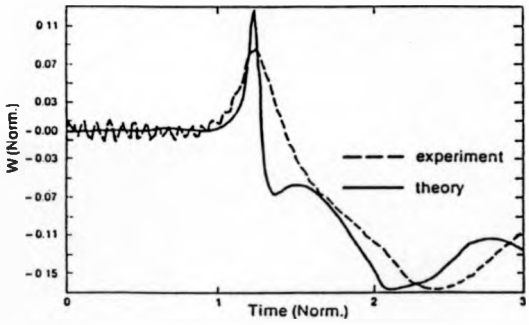

Fig 7.3 Comparison between measured displacement and the theoretical prediction for a two-dimensional , extended thermoelastic source

Optical penetration depth and Gaussian radius are 11.4% and 58% that of the plate thickness respectively . [Conant & Telshow , 7.3]

profile is instantaneous while in metals the precursor originates from the rapid diffusion of heat within the metal and hence evolves in time .

7.3.1 Theory

The description of such an extended thermoelastic interaction is based on the point source case of Rose [2] . Rose described the thermoelastic source as a "centre of expansion" at a point , d , below the surface of the sample , which using the formulation of Aki and Richards [4] for an isotropic material , expressed the displacement as a function of time , t , and distance ,z, from the source as

$$U(z,t) = \Gamma\, q(t) * g^{H}(z,\mathcal{E},t) \qquad 7.2$$

where * represents a convolution process , Γ is the time differential of the source strength and g^H is the Green's function for a centre of expansion source , where $\mathcal{E} \ni V$ the source volume being given as z=d,r=0 and q(t) is the normalised laser pulse profile . Γ is obtained by solution of the differential heat equation and may be expressed simply in terms of the properties of the laser pulse and the irradiated material , given by

$$\Gamma = \frac{E\alpha^{T}kQ}{[(1.2\nu)K]} \qquad 7.3$$

where E is Youngs modulus , Q the total heat input , α^T the coefficient of linear thermal expansion ,k the thermal diffusivity ,ν Poissons ratio and K the thermal conductivity . As verified experimentally [4.3 , 4.9] the source strength shows a linear increase with respect to the total heat input . The normalised laser pulse profile is treated as approaching a delta function as the pulse duration is lower by almost three orders of magnitude than the typical inspection times . The effect of the laser pulse may be examined further using convolution techniques on the delta-pulse wave solution . Eq. 7.2 was solved by Rose using the double integral technique , the resultant solution comprising of

the superposition of three terms . An initial wave travelling in the positive z direction and a reflected wave which has both longitudinal and shear motion . The shear motion originates from mode conversion at the top surface of the sample . Finally the transformed potentials are converted from bulk to surface potentials by letting d→ 0 and thus the source represents a surface centre of expansion . The resultant epicentral displacement is shown in Fig 6.3 . The ratio ,R , of the two discontinuities at the longitudinal and shear arrivals is given by

$$R = \frac{-1}{2}\left(\frac{2(1-v)}{(1-2v)}\right)^{3/2} \qquad 7.4$$

which is dependent only on the materials Poissons ratio . For perspex with measured wave velocities of Vp= 2750 ms^{-1} and Vs = 1390 ms^{-1} . eq 7.4 gives a value of R=3.9 compared to R=4.2 for aluminium and therefore no appreciable theoretical difference in the point source waveforms is expected between the two materials .

A buried thermoelastic source was modelled by considering the source to originate at a point below the surface , where the surrounding material had the same acoustic properties . Rose employed the same analysis as before and the resultant wave includes successive wave components from the top of the sample surface , Fig 7.4 showing the result of this calculation . The initial arrival , at t_1 , corresponds to a direct longitudinal wave from the point below the surface while the arrivals at t_2 and t_3 are the longitudinal and shear waves originate from reflection from the top surface . The longitudinal arrivals are characterised by delta pulses which are absent from the surface source . Inspection of the waveform shows that as the source moves towards the surface the resultant waveform will eventually tend to the surface solution with the cancellation of the delta pulses . The shear wave component is again only derived from mode conversion at the top surface and not from direct longitudinal motion . This proposed solution was verified by Hutchins [5] who

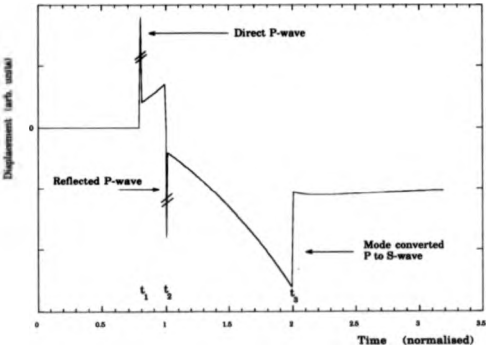

Fig 7.4 Theoretical , epicentral waveform calculated for a buried centre-of-expansion source . [after Rose]

used a thick oil layer above a metallic sample . The resultant waveform showed the essential features of the Rose model , having an initial longitudinal wave followed by reflected and phase changed longitudinal and shear wave components . The oil was able to support the shear motion as it is longitudinally polarized . The resultant acoustic displacement from a laser source decaying exponentially with depth is thus modelled as a summation of source components as given by

$$U(z,t) = \int_0^{\infty} g^H(z,t;d,0) * T(z,t)\, dz \qquad 7.5$$

Here it is assumed that the source is comprised of a series of point thermoelastic contributions , whose amplitude is weighted as a function of depth by the temperature profile . The approach adopted here is similar to that used by Chang and Sachse [5] , discussed earlier , however the authors used a surface and not a buried solution as their initial Greens function , thus neglecting reflections from the top of the sample . Since the laser pulse is not a delta function as assumed in the above mathematical development the resultant waveform is convolved with the CO_2 laser pulse profile q(t) . Fig 7.5a shows the result of the spatial summation , (eq.7.5) for q(t)=δ(t) and an optical absorption depth of 200μm . The summation gives the same features as the analysis of Conant and Telschow , with an initial positive longitudinal precursor followed by a negative longitudinal component and a shear arrival . The effect of the temporal convolution (Fig 7.5b) , shows the resulting loss of frequency content and the removal of the distinct negative longitudinal arrival , the waveform agreeing well with that measured experimentally by [3] (Fig 7.3) . This model , being a summation of buried sources , does not account for the spatial extent of the source which has a significant effect on the ultrasonic wave shape leading to a further loss in signal definition . The effect of source width does not , however , contribute to the initial precursor . An approximate solution to the wide source problem is to carry out a spatial convolution across

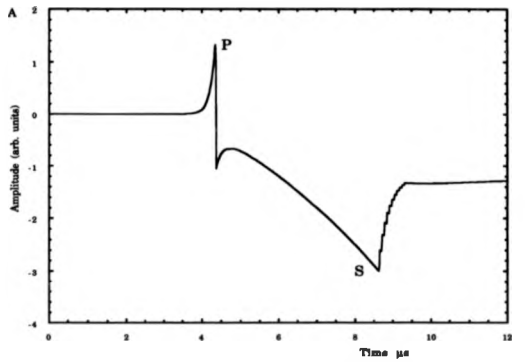

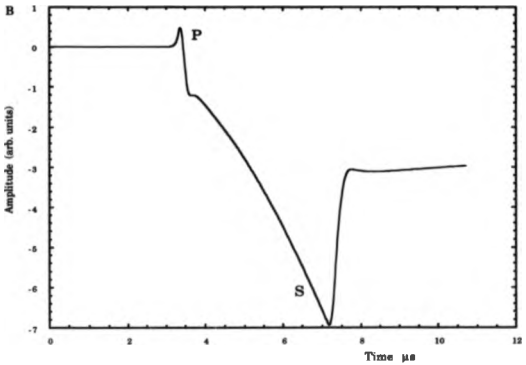

Fig 7.5 a& b Theoretical extended source thermoelastic waves for 200μm absorption depth with and without temporal convolution respectively .

the source width . This will have a similar effect as the temporal convolution , the extent of which will depend on the source width.

7.3.2 Source Strength

The source strength derived by Rose [2] shows a linear increase in displacement with increasing input energy . The equivalent source term , M , derived from Conant and Telachow [3] gives the source strength term as

$$M = \frac{(1-\nu)\alpha^2 T_0 a^2}{(1+\nu)} \qquad 7.6$$

where a is the beam profile , Gaussian radius . The source strength is therefore directly proportional to temperature elevation and therefore to laser energy . Fig 7.6 shows the amplitude variations of the positive and negative thermoelastic components measured intereferometrically . The horizontal scale is shown as the percentage transmitted radiation due to the inability to measure the absolute incident energy . Both portions of the waveform vary linearly , within the range of the thermoelastic regime , with increasing incident energy . As a measure of the source efficiency , the displacement as a function of incident laser energy is compared for CO_2 generation on non-metals with Nd:YAG generating on metals . The Nd:YAG data gives an efficiency of 33.3 nmJ^{-1} which is a factor of six lower than the CO_2 efficiency of 195 nmJ^{-1} . In terms of displacement per absorbed energy , however the CO_2 efficiency becomes lower than that of Nd:YAG generation , as almost all the 10.6μm radiation is absorbed at an air-dielectric interface as opposed to ~7% - 20% for 1.06μm at a metal surface . The decrease in generation efficiency may be accounted for the differing bulk properties of the two materials , although a direct comparison between the two source types cannot be made due to the differing source geometries .

For a thermoelastic source at the solid surface , the shape of the displacement waveform is expected to be independent of the incident energy ,

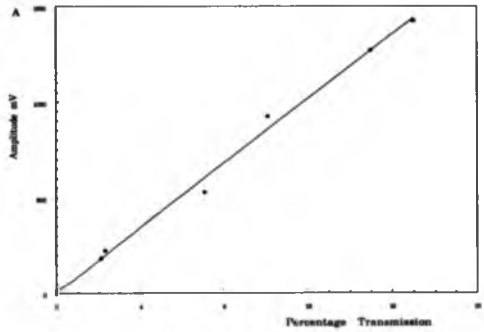

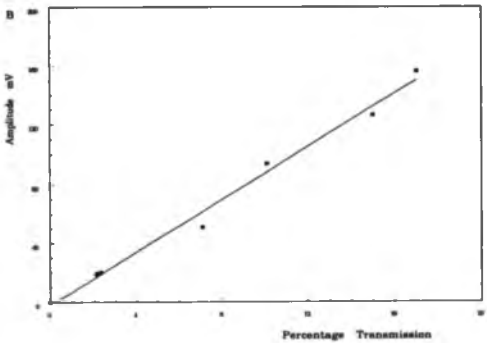

Fig 7.6 Variation in amplitude of the negative and positive components of the extended thermoelastic waveform .

only the overall displacement amplitude changing . For an optically penetrating media the nature of the waveform together with its amplitude will vary . If significant source contributions originate from a temperature of $T_{z'}$, an increase in surface temperature , via increased incident radiation energy , results in the depth , z' , to which the temperature has dropped to this value increasing and thus the source extent increases correspondingly . Rearranging eq 7.1 gives this depth variation to be governed as

$$Z' = \alpha \ln\left(\frac{T_o}{T_{z'}}\right) \qquad 7.7$$

This trend is shown in Fig 7.7 for $T_{z'} = 100^oC$. The form of the increase in depth will depend on the temperature to which significant contributions are produced .The graph clearly shows the "effective" source depth to increase by ~50μm per 100°C increase , a value which is comparable to the optical absorption depth . The effect of the increased source depth is modelled by increasing the effective optical absorption depth of the material , which produces an increase in the risetime of the positive longitudinal precursor , as shown in Fig 7.8 calculated for α≈400μm . The negative going pulse which is lost by convolution in Fig 7.5b ,becomes more pronounced as it has greater "area" associated with it for the deeper penetrating source .

Fig. 7.9a&b shows two thermoelastic waveforms recorded on a 12.5mm thick glass sample . The first was recorded under the action of a 3.5mm source radius as compared to 1.5mm for the lower trace . The effect of the source width is evident in the loss of wave definition at larger source radii resulting in no distinct negative longitudinal arrival and the loss in shear wave gradient change . The result of any source contributions from within the bulk of the material is partly masked by the contributions from the source width . Glass has an optical penetration depth of ~50μm for 10.6μm radiation and therefore the spread in arrival times originating from the source depth is out-weighed by

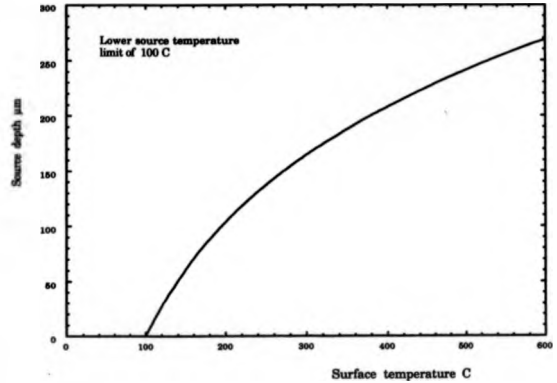

Fig 7.7 Increase in source depth as a function of increasing surface temperature assuming source components originate above a certain temperature .

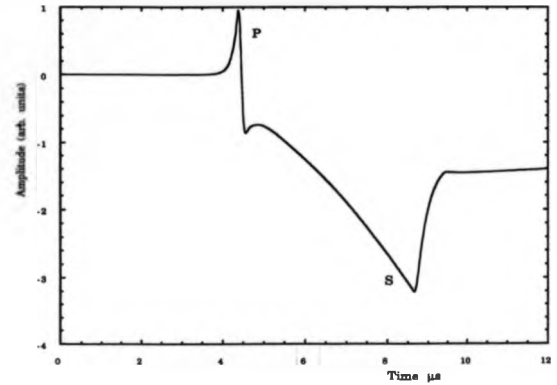

Fig 7.8 Epicentral thermoelastic waveform for 400µm absorption depth to demonstrate the effect of increased optical penetration .

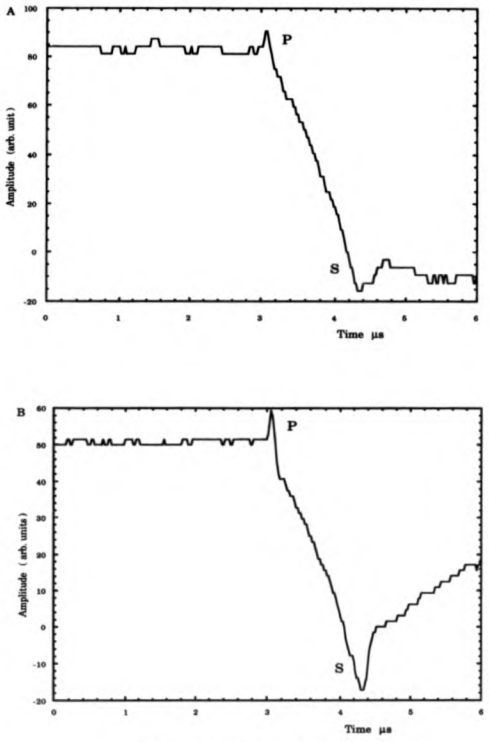

Fig 7.9 a& b Epicentral waves recorded on glass for source diameters 3.5mm and 1.5mm respectively .

the arrival spread originating from across the source by a factor of approximately 2 , from a 1.5mm source radius .

Measurements of the initial longitudinal arrivals show the risetimes to increase from 35.0±2.5 ns to 40.0±2.5 ns in response to increasing the power density by a factor of 1.7 . This increase in risetime corresponds to an increase in source depth of 30±5μm , using v_p=5978.4ms^{-1} determined experimentally . Fig 7.10a&b shows as for the glass sample , measurements recorded on a 12.4mm thick perspex sample , for a source radius of 3.5mm (corresponding to Fig 7.9a) . Both waveforms show the distinct longitudinal precursor , the lower waveform being recorded with an increase in power density of a factor 10 which is reflected in a measurable increased duration of the precursor . Fig 7.11 gives the form of the longitudinal wave for constant source size but increasing incident energy in the ratio 1:6:29 . The pulse risetimes increase from 50±2ns at low energy to 70±2ns at high incident energy , corresponding to an increase of ~60μm to which significant source contributions are produced . The changing form of the longitudinal arrival with increasing energy may be observed more closely by decreasing the source size , as shown in Fig7.12 , with a source radius of 1.5mm. The successive waveforms , corresponding to the same ratio of incident energy , show a similar increase of 20ns in the longitudinal risetime . The increase in the negative component of the wave follows closely the prediction shown in Fig 7.8 for an increased source depth . This effect is masked to a greater extent for the 3.5mm radius source although an observable trend to a more distinct negative arrival is apparent .

The elevation of the surface temperature results eventually in the melting and vapourisation points being reached . Fig 7.13 shows the depth to which the vapourisation temperature is reached for increasing surface temperature , assuming a vapourisation temperature of 400 C as for perspex [6] . This suggests that a layer 50μm will be removed for a surface temperature of 600 C . Therefore the source is no longer purely thermoelastic but is a superposition of

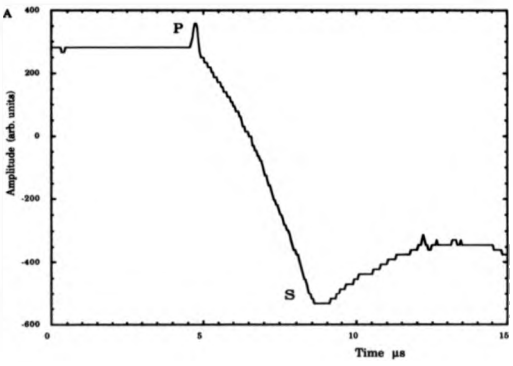

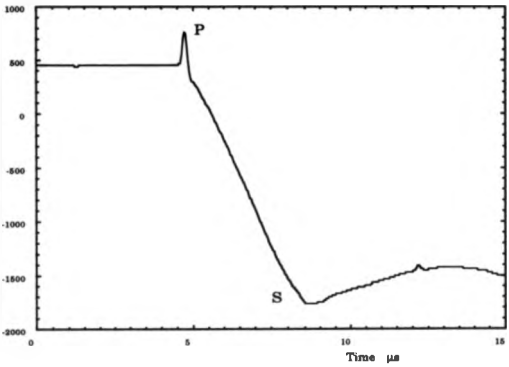

Fig 7.10 a & b Thermoelastic epicentral waves recorded on Perspex with a source radius of 3.5mm for increasing incident laser energy .

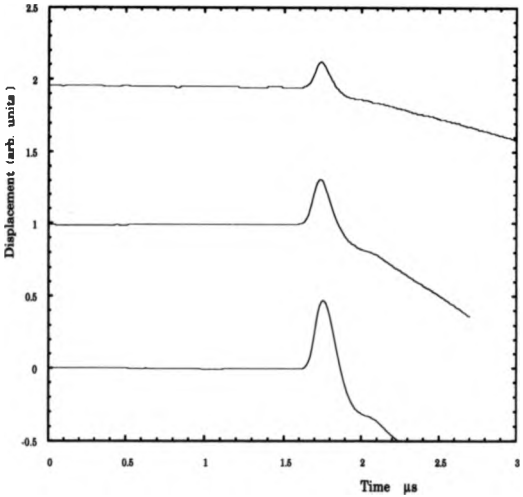

Fig 7.11 A series of longitudinal arrivals recorded for increasing incident laser energy .
Source radius 3.5mm

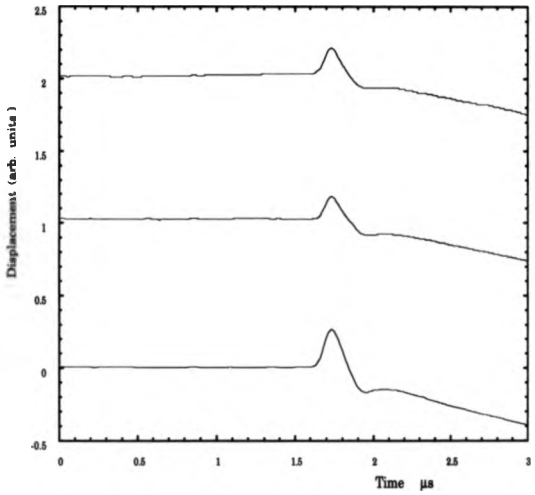

Fig 7.12 A series of longitudinal arrivals recorded for increasing incident laser energy .
Source radius 1.5 mm

sources . Fig 7.14 shows the superposition of waveforms resulting from evaporative and thermoelastic sources in the ratio 1:1 . The definition of the negative component of the longitudinal arrival created by the further extension of the source into the material is increased and the waveform agrees closely with the experimental result shown in Fig 7.15a . The risetime of this waveform , being 100±2ns , reflects the continued effect of the increased source depth . The polarity of the longitudinal and shear displacements changes as the source changes from being predominantly thermoelastic to evaporative , as shown in Fig 7.15b . The increased evaporation results in a non-impulsive source type which extends in time to become almost Heaviside in nature . Dewhurst et. al. [7] showed this trend for varying source functions and demonstrated the normal and radial force components needed to accurately model the transition observed with Nd:YAG lasers on metals . At these very high power densities the risetime reaches ~130ns corresponding to a penetration depth of 400μm , which is over twice the initially measured , low power density value of 150μm .

Glass exhibits a similar behaviour to that in perspex , (Fig 7.16 a&b) , which corresponds closely to those in Fig 7.15 b , having a near Heaviside type , normal , surface force . The relative amplitude ratio of the initial longitudinal to shear waves is much lower in the case of glass as compared to perspex . The results recorded on glass agree closely with the mixed source function work of Dewhurst [7] in which purely surface forces are considered , indicating that the enhanced longitudinal motion observed on perspex is due to the optical penetration depth of radiation within the sample .

The increase in evaporation is marked on both glass and perspex by visible emission of target material . At low power density this takes the form of a white powder ejected with a low energy turbulent flow , while as the power density is elevated the emission material luminosity and ejection velocity both increase . Fig 7.13 indicates that material may be removed to a depth of up to

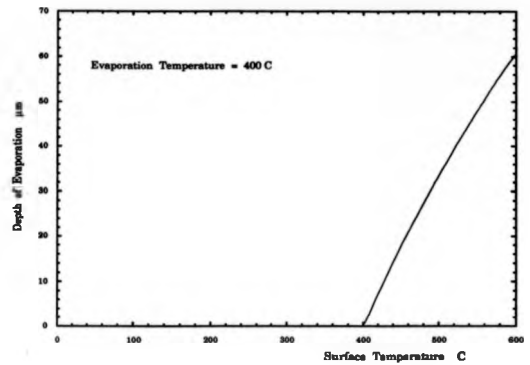

Fig 7.13 The depth to which evaporation occurs as a function of increasing surface temperature.

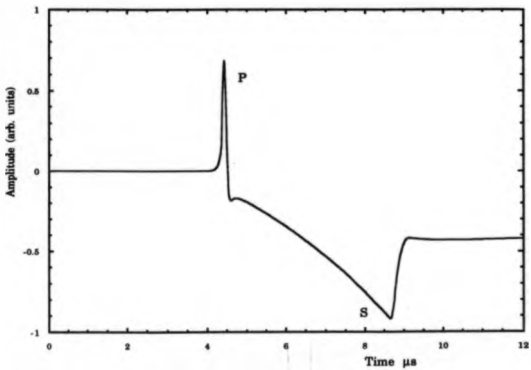

Fig 7.14 Superposition of evaporative and extended thermoelastic source waveforms with equal weighting.

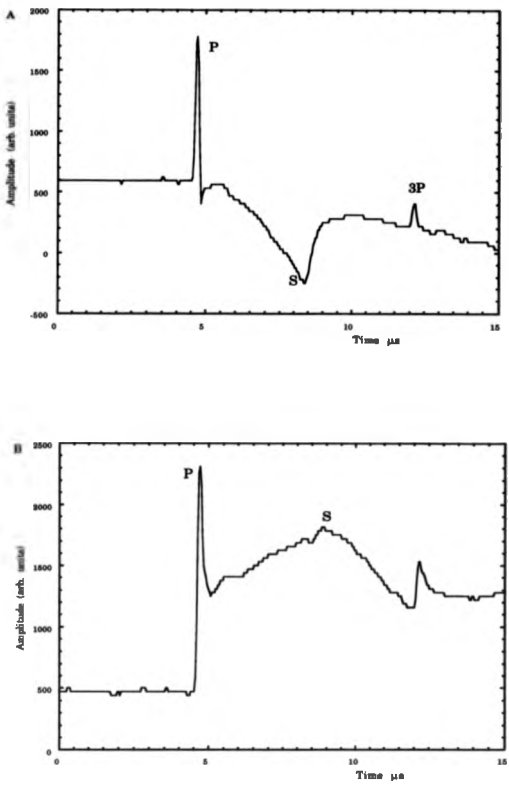

Fig 7.15 a & b Mixed thermoelastic and evaporative waves recorded on Perspex .

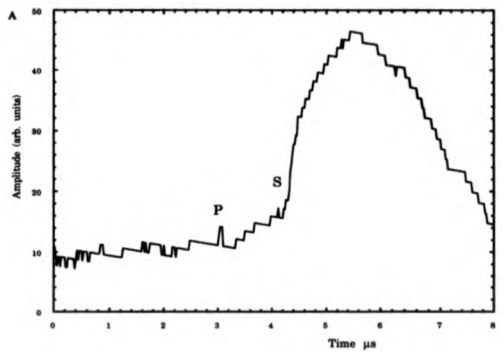

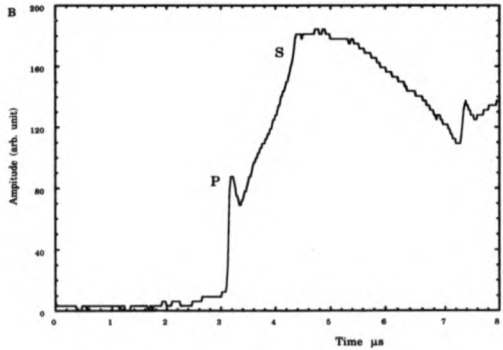

Fig 7.16 a & b Mixed thermoelastic and evaporative waves recorded on glass

~50μm . This figure does not however account for the degree of shielding of the surface offered by the ejected material which as it is luminous must absorb the incident radiation . The loss of target material was measured over a range of incident power densities to verify the degree to which shielding of the surface takes place due to the presence of a vapour or plasma .

As the amount of mass loss per shot is low , of the order 10^{-5} grams , small ~$1cm^2$ square samples of perspex were irradiated twenty times at constant power density to produce a degree of mass loss measurable with a low associated error . The resultant sample damage produces , over a number of shots , a non-uniform target area which becomes increasingly conical and thus the area presented to the incident beam is increased , possibly effecting the exact radiation-target interaction . To avoid this the target was repositioned after each shot to produce a constant source . Fig 7.17 shows the mass loss per shot over a range of power densities , with a $1mm^2$ source size . At maximum incident energy , producing a well defined L D W , the action of the radiation is to produce a large mass loss , a value which is decreased as the laser energy is attenuated within the range required to generate a L D W . A rapid increase in the amount of material evaporated occurs at ~50% transmission , due to the onset of a L P source . This increase follows the increased penetration of radiation within the plasma and as such evaporation occurs throughout the laser pulse duration . Subsequent attenuation results in an almost linear decrease in the amount of material ablated for sources ranging from L P through to visible vapour emission and low energy non-visible material blow-off . The inset graph shows the mass loss per shot per joule , which highlights the increased degree of material evaporation as the shielding of the plasma above the sample is reduced , shown only to be significant within the L D W regime .

Scanning electron microscope pictures of the irradiated area reveal the difference in laser matter interaction under the action of a strong evaporative

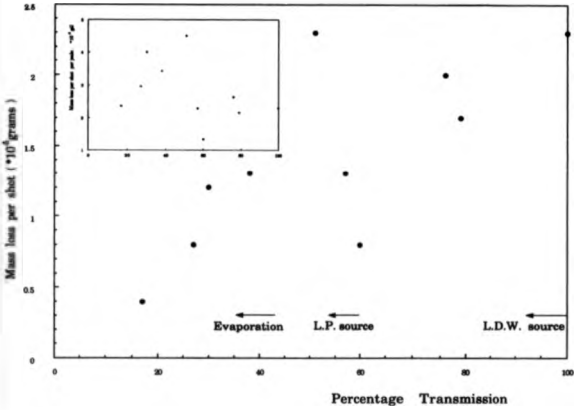

Fig 7.17 Variation in mass of perspex lost upon irratiation as a function of increasing incident energy .

source as opposed to a dense plasma source . Fig 7.18 shows the effect of the non-plasma interaction , which produces a large degree of heat damage to the surface . This results in charring and restructuring of the surface material under the action of rapid heating and subsequent cooling . This interaction contrasts strongly to the action of a dense plasma which shields the surface after a time duration of ~30ns , short in comparison with the laser pulse duration . The resulting surface damage , presented in Fig 7.19 , shows little of the gross surface distortion produced by evaporation . The top picture shows that in the central region of the irradiated area the perspex surface is relatively smooth , as is shown in detail in the bottom photograph , while at the edges of the beam does one see signs of excess heating which indicates that the plasma electron density in this region is sufficiently low that penetration of the incident radiation still occurs . Therefore the high power density almost instantly removes a layer of material from the surface which is sufficiently highly ionized that a plasma develops above the surface , thus screening the sample from further damage .

This is verified by the order of magnitude calculations presented below giving the required flux to heat the evaporated material to a point where visible emission occurs . Consider the ejected material to be at a temperature T , then the energy ,E , associated with this temperature is given by equipartition of energy as

$$E = \frac{3}{2} k_B T \qquad 7.8$$

where k_B is Boltzmann's constant , and the factor of three originates from the number of degrees of freedom of the vapour particles . Due to the low incident photon energy , ε , associated with 10.6 μm radiation this elevation of temperature must occur from a multiphoton interaction , where the energy balance is simply $E < n\varepsilon$, (eq. 3.3) , where n is the required number of photons required to produce such a temperature elevation . The flux , F,

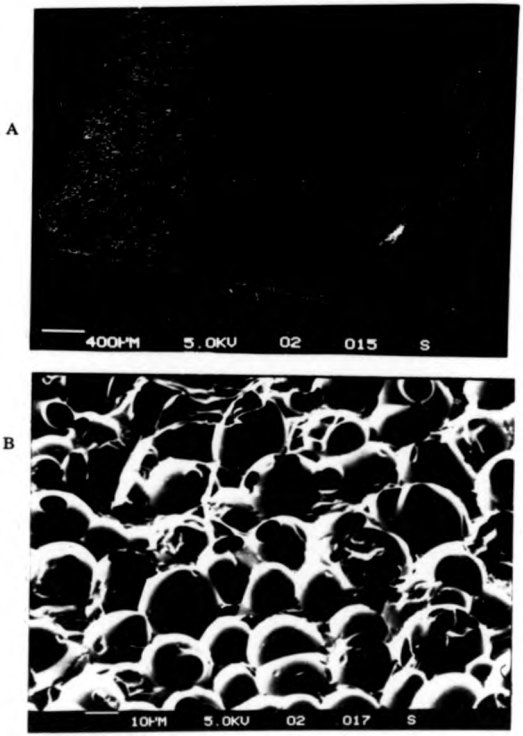

Fig 7.18 a & b S.E.M. photographs showing the effect of evaporation on Perspex due to high power 10.6µm radiation .

A

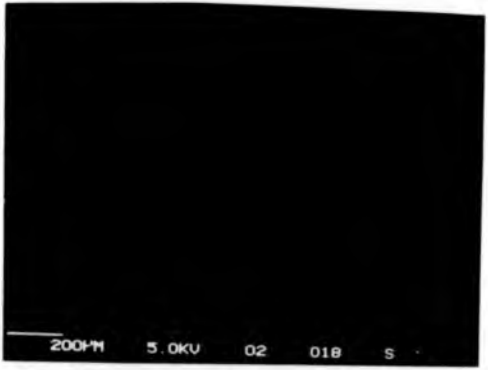

B

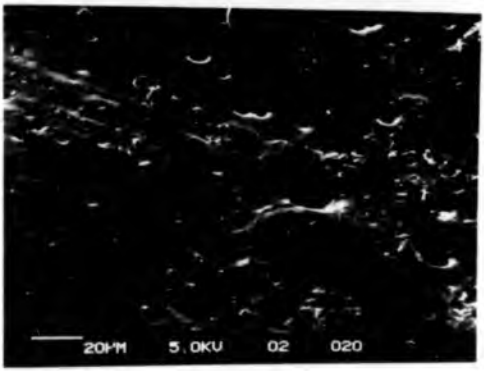

Fig 7.19 a & b S.E.M. photographs showing the effect of a L.D.W. plasma source on Perspex .

required to produce such a multiphoton process is therefore expressed in the standard form as $F = \frac{n}{\tau A_A}$ where A_A is the area associated with a vapour atom and τ is the time in which the process must occur , governed by Heisenburg's uncertainty principle giving $\tau \geq h/4\pi E$, giving the flux required for the process as

$$F = \frac{4\pi E^2}{h\epsilon A_A} \qquad 7.9$$

The temperature of the gas may be estimated from the central wavelength , λ_{max} , of the vapour . Using Wein's Law , based on Planck's black body radiation theory , the wavelength of the vapour may be related by

$$\lambda_{max} T = \frac{hc}{2.8k_B} \qquad 7.10$$

The use of this theory gives an approximate order of magnitude for the vapour temperature , but is far from an exact method as the emitted light corresponds to discrete excitation levels and not from a continuum . The area of the irradiated molecules may be estimated to an order of magnitude . If the evaporated molecules are composed of approximately 100 atoms , a figure which will be discussed later , then their cross section is of the order 10^{-14} cm^{-2} , a value which may increase due to the thermal excitation of the molecule . Substitution of the approximate molecular cross section and the temperature , estimated at ~500 C , into eq.7.9 gives an estimation of the required flux to be $\sim 5*10^{28}$ $s^{-1}cm^{-1}$ for the laser beam area of 0.04 cm^{-2} , the minimum area attainable before breakdown occurs . Therefore a considerable proportion of the beam is able to pass through the vapour and onto the sample where continued evaporation occurs .

The mass loss determined experimentally , (Fig 7.17) , gives an average $\sim 1.5*10^{-5}$ g per shot . For perspex , with a density of 1170±12 kgm^{-3} and an irradiated area of 10^{-6} m^2 this yields a depth to which material is removed of ~13μm , a depth considerably larger that the typical ~1μm depth produced on

metals by a high power Nd:YAG laser . It is interesting to consider the possible bulk damage , other than the evaporation , which may be generated by the large laser pulse energy and power interacting with the irradiated solid . Perspex is a very long chain molecule having an estimated molecular mass of $\sim(1.5 - 3)*10^6$ amu . As perspex comprises mainly of carbon , hydrogen and oxygen atoms , a mean atomic mass of ~12 amu may be used to give the molecular number of $\sim10^5$ atoms . Therefore if typical bond lengths of ~2.5Å are assumed this gives a molecular volume of the order $10^{-24}m^3$. In one shot the radiation energy is distributed throughout a volume of $\sim2.5*10^{-9}$ m^3 assuming a spot size of 2mm square and an absorption depth of 600μm , approximately three times the optical absorption depth . For the sake of these order of magnitude calculations a uniform irradiation model is assumed which neglects the Beer's law decay and any radiation absorption within the plasma the second approximation shown to be valid in the work above . The volume estimated previously corresponds to $\sim10^{18}$ molecules irradiated . The heat of depolimerization of perspex is 56kJ/mol , being the energy required to break one bond in each of N_A molecules , corresponding to an energy of $\sim10^{-19}$ J required per molecule . Therefore the number of bonds in the irradiated volume may be calculated using the total input energy , which for the CO_2 laser is 1J , giving $\sim10^6$ bonds broken per molecule corresponding to the complete dissociation of the perspex molecule . This level of dissociation contrasts strongly with the 13μm depth to which material damage was measured to occur . Thermal diffusion of heat away from the irradiated volume as determined by the thermal skin depth , $\delta_T = \sqrt{4\kappa T}$ with $\kappa=5*10^{-7}m^2s^{-1}$ typical for a non-metal produces diffusion to ~0.5μm away from the heat source which is small in comparison with the optical penetration depth thus not accounting for any major redistribution of heat .

The heating of the solid may change the optical and thermal properties of the material sufficiently rapidly that shielding of the deeper regions of the

perspex occurs thus isolating the bulk from continued damage . Despite possible shielding mechanisms one must conclude that a large number of bonds are broken to depths well in excess of the depth to which evaporation occured . This may result in the change of the physical characteristics of the material , such as weakening , although no optical modification of the perspex resulted . Similar calculations for glass , with typical bond strengths of the order 300kJ/mol , suggest that the degree of bond breaking is significantly reduced and the input of energy results only in heating .

7.4 Plasma Breakdown Results

For incident power densities $\geq 5*10^7$ Wcm^{-2} , on both perspex and glass , plasma breakdown occurs at the target surface , as for the case of metals . It is interesting to note that this corresponds to the same power density required to generate breakdown above an aluminium target despite the fact that perspex and glass have work functions much lower than metals . This increase over the theoretically predicted value of $\sim 10^7$ Wcm^{-2} may be accounted for by the distribution of heat within the non-metals and the absence of the large reflected component of the beam .

Once breakdown is initiated both L P and L D W sources are generated dependent on the power density . Fig 7.20 shows streak camera measurements of the plasma recorded above a perspex sample and also includes the motion of the material vapour . These measurements show both the evaporative source and particularly the L P to persist at the sample surface for up to 300ns and 500ns respectively . The L D W source moves rapidly away from the surface within a time of 70ns .

As the plasma delivers a large surface force , an out-of-plane sensitive EMAT was used to measure the surface motion . The expected surface motion is shown in Fig 7.21 a&b , where a, corresponds to the time differential of

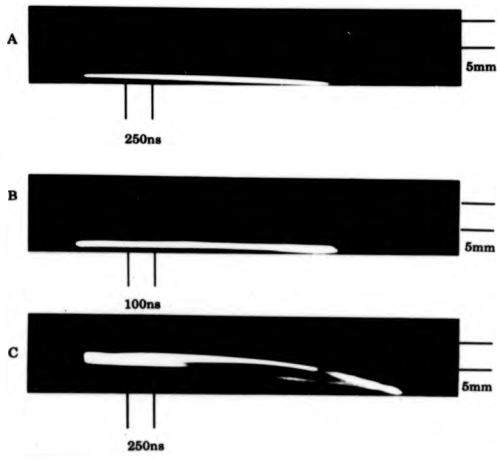

Fig 7.20 a , b & c Streak camera measurements showing evaporative and plasma luminosity time histories .

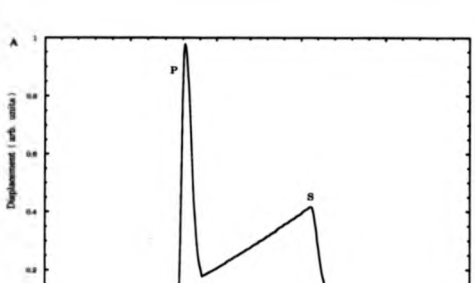

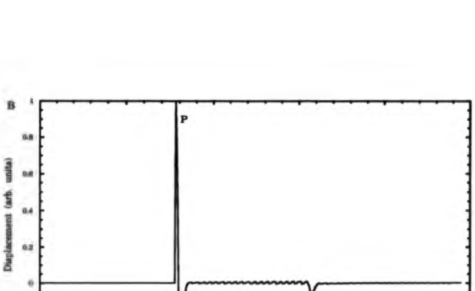

Fig 7.21 a & b First and second time derivatives of Knopoff's solution .

Knopoff's solution and b, is the second derivative corresponding to a velocity sensor detecting an impulsive source type . Fig 7.22a&b show the experimentally measured bulk waves generated in glass by both L P and L D W sources respectively . The distinction between the two waveforms is clear with the L P source producing an essentially monopolar longitudinal arrival and a shear wave observed simply as a step , while the L D W produces a well defined bipolar longitudinal wave and a monopolar shear arrival . The higher power density of the L D W trace shows an increased risetime from 40ns to 50ns , once again indicating increased penetration within the sample . This trend is repeated in the perspex measurements shown in Fig 7.23a&b , where the L P produces a 75ns risetime compared to 110ns generated by the L D W and the form of the waveforms again agree closely with theory . The origin of the surface modulations observed before the longitudinal wave in Fig 7.23b were observed to be proportional in amplitude to the incident power density . However the arrival time suggests that if it is ultrasonic in nature that it travelled 5mm less than the longitudinal surface arrival , although its shape does not follow any of the above theory . The 10.6 μm radiation is not responsible for the pulse due to the strong absorption of the beam and timing measurements show that it is not produced from the plasma light emission .

7.5 Discussion & Conclusion

The strong coupling of laser radiation to non-metallic materials via infrared absorption leads to large amplitude ultrasonic transients being readily generated . The generation mechanism falls into three regimes although they are not independent of one another . For incident power densities $\leq 10^7$ Wcm^{-2} a thermoelastic generation mechanism is produced the main feature of which are the optical penetration within the sample and the coupling of source depth to power density . Between $\sim(1\text{-}5)*10^7$ Wcm^{-2} the

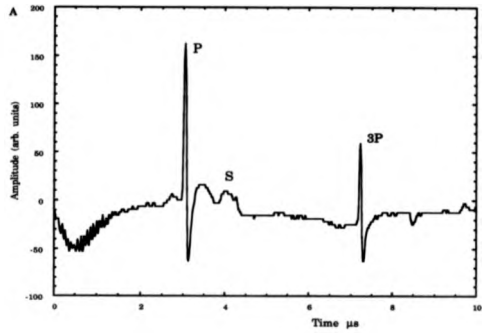

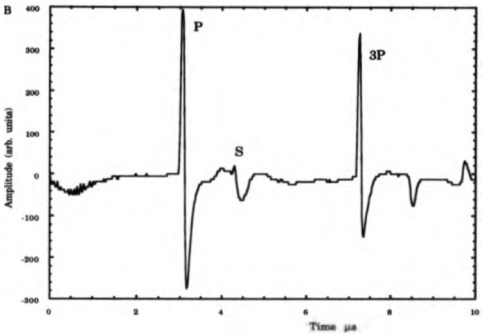

Fig 7.22 a& b Epicentral waves recorded on glass under the action of LP and LDW plasma sources respectively.

thermoelastic regime becomes modified by the presence of normal surface forces originating from the evaporation of the irradiated material . The proportion of thermoelastic to evaporative source strengths obviously decreases with increasing power density , although the effect of the thermoelastic interaction was shown to persist even at the highest power densities and to modify the resultant waveform . Above these power densities L P and L D W plasma sources are produced .

The theory presented for the effect of the extended thermoelastic source describes closely the experimentally observed on-epicentre waveforms .This approach is however rather qualitative in its description of a two dimensional , wide / extended source , and the proposed convolution techniques breakdown as the source dimensions increase for the reasons discussed in chapter 5 when the point source Green's function varies considerably across the source .

The range of successfully inspected materials is wide having been employed on a range of plastics and composites . Generation of ultrasound in a pull-trusion composite , producing low surface damage , produced transients of sufficient amplitude as to be detected with a 5MHz centred , wideband , Panametrics PZT probe stood off the sample surface by an air gap of up to 15mm [8] . The use of a Nd:YAG laser to generate ultrasound in such composites resulted in a large charring of the sample surface .

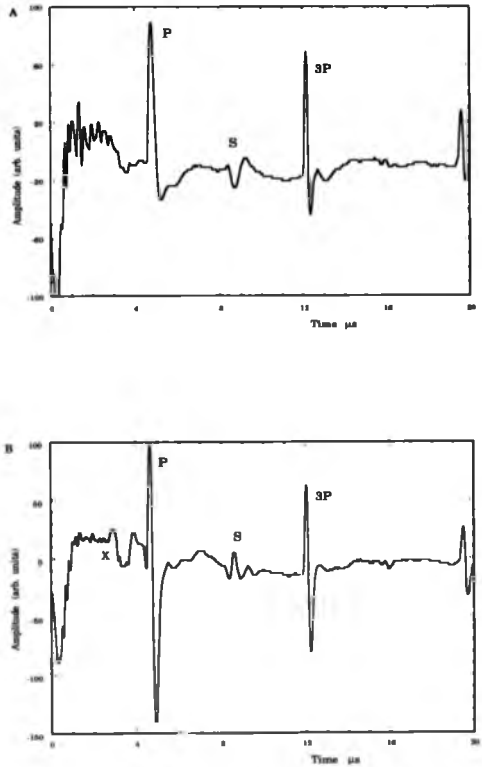

Fig 7.23 a & b Epicentral waves recorded on Perspex under the action of LP and LDW sources respectively .

References Chapter 7

[1]C. Chang & W. Sachse , J.A.S.A. vol77 pp1335-1341 (1985)
[2]L.R.F. Rose , J.A.S.A. vol75 no3 pp723-732 (1984)
[3]R.J. Conant & K.L. Telschow in "Review of Progress in QNDE" (D.O. Thompson and D.E. Chimenti eds.) (1989)
[4]K. Aki & P.G. Richards , "Quantitative Seismology" (Freeman) (1980)
[5]D.A. Hutchins in Physical Acoustics , edited by W.P. Mason and R.N. Thurston (Academic Press) vol 18 pp21-123 (1988)
[6]Properties of Perspex given by I.C.I.
[7]R.J. Dewhurst , D.A. Hutchins , S.B. Palmer & C.B. Scruby , J. Appl. Phys vol 53 pp4064-4071 (1982)
[8]J. Lowrey , 3rd Year Experimental Report , Engineering Department , Warwick University (1990)

Chapter 8

Laser Probe Detection of Ultrasound

8.1 Introduction .

The remote detection of ultrasound using both interferometers and EMATs ,has been previously discussed in chapter 2 . The interferometer has the excellent advantage of being an absolute surface displacement detector , enabling theoretical models of surface motion to be compared to experimentally generated ultrasonic transients . However the requirement of critical alignment of sample to detector and the restriction of having highly polished sample surfaces makes the interferometer very much a laboratory based tool .The EMATs are however vastly superior to interferometric detection with respect to their ease of use , in that an angular tilt of several degrees to the sample surface has little or no effect on the detected signal . The limitation in their use comes from the relatively small working stand-off distances of up to about 7mm . The separation of detector and sample is governed predominantly by the geometrical spreading of the vector potential and the decay in magnetic field strength as a function of distance from the pole pieces .

Other means of non-contacting detection have previously been examined , such as capacitance probes [1] , which require sample smoothness of the order 1μm and a proximity to the sample surface of about 50μm dependent on probe bias voltage . Laser beam deflection techniques such as Knife edge detectors have also been widely employed , to-date however their use has been mainly restricted to the detection of CW ultrasonic surface waves [2] and transient Lamb wave detection [3] . As will be discussed more fully later , laser probe detection offers large flexibility in its geometry , and being an optical technique is suited to comparatively large sample - detector distances .

This chapter examines the limitation of laser probe detector resolution and sensitivity for two types of detector . This is done by the examination of

ultrasonic Lamb , Rayleigh and bulk transient waves . The study will include the examination of both opaque and transparent materials and the advantages offered by such detection means .

8.2 Method of Knife Edge Detection .

The traditional and most basic form of these detectors relies on laser radiation being directed at a material carrying ultrasonic transients , as shown in Fig 8.1. The beam is focused to a spot at the sample to increase the resolution of the device by decreasing the area of detection . The reflected light is directed towards a photodiode . Placed just in front of the photodiode is an opaque object or "knife edge" which obscures approximately half of the photodiodes area and half of the reflected light . A focusing lens may be used to reduce the solid angle of the reflected light to that of the photodiode . Deflection of the laser beam , caused by the interaction with the ultrasonic wave , produces a change of light intensity allowed passed the knife edge onto the photodiode . This fluctuation enables the ultrasonic signal to be detected .Such a probe is very insensitive to outward surface displacement . For a beam incident at an angle α to the normal from the sample , a surface displacement , δ , will cause the beam to by translated by an amount $2\delta\sin\alpha$. Hence for a surface displacement of the order 10nm , a beam incident at an angle of 45^{o} will be displaced by only 17 nm , producing no significant variation in light intensity at the detector . However the effect of surface tilt produces sufficient rotation of the reflected beam to enable light intensity fluctuations to be measured by the photodetector .

Consider the incident probe beam to be at a point P on the surface . An ultrasonic wave travelling across the point P will produce an outward displacement ,δ_1 , at a point just before P , say x and an outward displacement

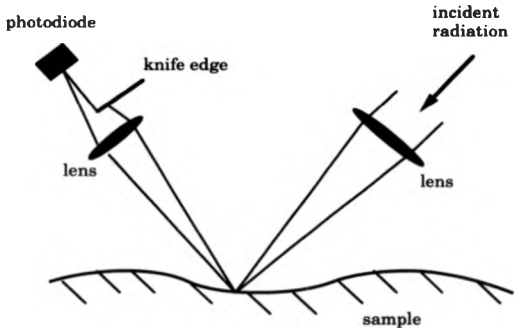

Fig 8.1 Optical knife edge probe for the detection of surface angular tilt .

δ_2 , at a point x+Δx . Therefore the local surface gradient in the region of P is naturally expressed a

$$g = \frac{\delta_1 - \delta_2}{\Delta x} \sim \frac{dU_z}{dx} \qquad 8.1$$

Thus for the outward displacement produced by the ultrasonic transients , U_z, of the order 10nm and dx corresponding to the spot size of the focused probe laser (diffraction limited of the order 0.01mm) , g the gradient has a value $\sim 1 \cdot 10^{-4}$. From standard geometrical optics , if the plane of a reflector is rotated by some angle then the new angle between an incident beam and a reflected beam will change by twice the angular change made by the reflector .Thus the angular change in the reflected beam θ , may be given by $\theta = 2\tan^{-1}(g)$ which as g is small this can be approximated to $\theta = 2g$. Hence the arc subtended at a photodiode placed at a distance R from the sample surface is simply given by Rθ , where θ is expressed in radians . For R=25 cm , a typical distance used throughout these experiments , the arc subtended at the detector would be of the order 25μm . This value is therefore two orders of magnitude greater than beam displacements produced by outward surface motion and therefore the local surface tilt is the predominant signal source . The change in light intensity at the detector may be calculated if the laser beam profile is sufficiently well known . For a uniform deflection of the probe beam across its width , it is important that its width is smaller than the wavelength of the ultrasound being detected . The width of 0.01mm determined above corresponds to an upper frequency limit for Rayleigh wave detection of $\sim 3 \cdot 10^2$MHz , a figure well in excess of the frequencies generated in this work .

8.2.1 Experimental Arrangement.

Two modified knife edge detector arrangements were used in an attempt to maximize the signal sensitivity and responsivity of the laser probe detector . Firstly , high speed photodiodes are essential , if ultrasonic transients of

frequencies up to ~20MHz are to be observed . The risetime of the photodiodes used in this work were minimized to a point where significant signal was still developed at the detector output . A pulsed , fast , forward biased LED was used as a light source having a risetime of ~1ns , a value well below the risetime of the ultrasound generated in this study . The response time of the photodiodes is limited by the time constant set up by the diode capacitance and load resistance . Lowering the load resistance lowers the RC time constant , but also lowers the signal output amplitude . A risetime of 7ns was found to give a sufficiently large signal amplitude risetime product for this work . Secondly a high quantum efficiency is required to give a significant output for low amplitude light variations . Thirdly , suitable pre-amplifiers , with large bandwidth and high signal to noise are required to enhance the signal from the photodiode . A consequence of this need for individually matched amplifiers to each photodiode is that a direct comparison between the two design sensitivities is difficult to make due to varying amplifier gain-frequecy characteristics , as shown in Fig 2.5 and signal to noise values .

8.2.2 Design One

The traditional design of knife edge detector was modified by placing a short focal length cylindrical lens in the path of the reflected beam and removing the knife edge placed before the detector , as shown in Fig 8.2a. This type of detection offers the advantage that more selective sampling of the probe beam can be made increasing the devices sensitivity while decreasing the noise level . Assuming the probe laser to have a circular , Gaussian profile ,then the light transmitted by the cylindrical lens has a planar Gaussian profile . A photodiode with a small active area is placed at the focus of the cylindrical lens as a detector , two types were used in this study BPX65 or a "Sweetspot" diode with a built in 40MHz pre -amp with or without an optical fibre . The position of the detector with respect to the peak of the Gaussian

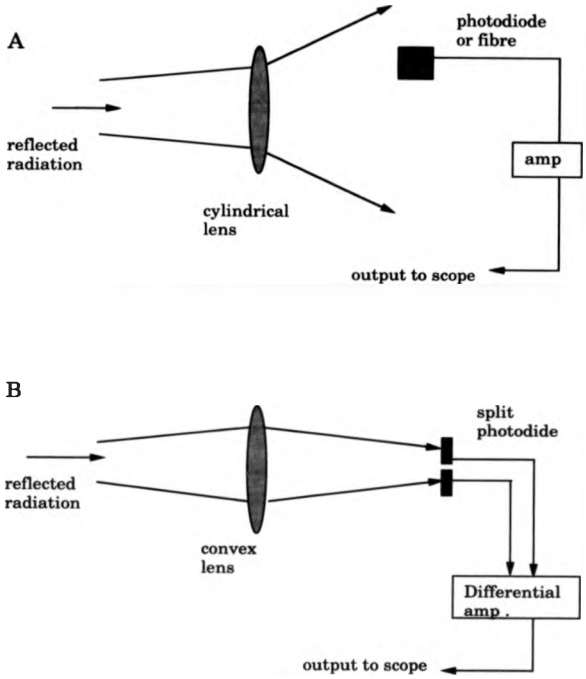

Fig 8.2 Modified detection systems for the laser probe detector
A: Single photodiode detector placed at the focus of the cylindrical lens
B: Split photodiode placed at the focus of a convex lens .

beam is an important point to consider and as will be shown , maximum signal is obtained by placing the detector at the position where the light intensity gradient is a maximum .

The sensitivity of such a device to an angular deflection ,θ , of the sample surface may be calculated simply by considering geometric optics . Assume initially a point detection spot and point photodiode for simplicity . The passage of the ultrasonic wave across the path of a probe beam produces the deflection of the beam which in turn alters the intensity at the photodiode , being expressed by

$$I_{sig} = I_m\left(\exp\left(-\frac{x^2}{\alpha^2}\right) - \exp\left(-\frac{(x+2R\theta)^2}{\alpha^2}\right)\right) \qquad 8.2$$

where Im is the peak beam power , α the Gaussian radius of the reflected probe beam , x the position from the centre of the beam of the detector and 2Rθ is the deflection of the beam . This analysis uses a one dimensional Gaussian beam profile , which as the detector is at the focus of the cylindrical lens is a valid assumption . If we assume a small beam deflection , eq. 8.2 may be rewritten on the expansion of the quadratic and the exponential functions , keeping first order terms , as

$$I_{sig} = I_m\left(\frac{4Rx\theta}{\alpha^2}\right)\exp\left(-\frac{x^2}{\alpha^2}\right) \qquad 8.3$$

Rearranging eq 8.3 gives the angular calibration of the technique , which is different from that derived for the conventional knife edge detector shown in Fig 8.1 [4] ,and maybe given as

$$\theta = \frac{\alpha^2}{4Rx}\frac{I_{sig}}{I_o} \qquad 8.4$$

where $I_o = I_m\exp(-x^2/\alpha^2)$. The Gaussian radius may be determined using the respective matrices [5] for the various optical stages of the beam . For an initial

focusing lens of focal length , f_1 , and a cylindrical lens of focal length , f_2 , α may be given as

$$\alpha = \frac{wf_2/R}{f_1\left(\frac{f_2}{f_1} - 1\right)} \qquad 8.5$$

where w is the source radiation Gaussian radius . Using the expression for the diffraction limited spot size ,D , where $D=1.22f_1\lambda_p/w$ [6] , λ_p being the wavelength of the incident light substituting into eq 8.4 gives the final calibration for the instrument as

$$\theta = \frac{(1.22)^2\lambda_p^2}{4\pi D^2}(R - f_2)^2\frac{I_{sig}}{I_o} \qquad 8.6$$

This expression is more complex than that derived by Monchalin [4] who assumed a simplified square beam profile . From eq 8.3 the sensitivity and the minimum detectable signal may be calculated . The sensitivity of the device may be determined using a finite detector width of 1mm , modelled by a steep sided Tukey function instead of the point detector and with a Gaussian width of 0.6mm determined from a fine resolution beam profile scan across the cylindrically focused beam . Fig 8.3a shows the theoretical sensitivity to be a maximum when the detector is placed at the maximum intensity gradient of the reflected probe beam . Fig 8.3b shows the experimentally determined sensitivity using a constant laser generated source and measured by scanning the photodetector across the 1-D Gaussian profile while recording the measured longitudinal amplitude . The two graphs show excellent agreement although the variation in the experimental peak amplitudes for the two sides of the beam is unaccounted for .

The minimum detectable signal may be calculated by setting the signal to noise ratio equal to unity . The noise is predominated by shot noise from the photons incident on the photodetector , giving a signal current , i_{sig}, to noise current ,i_n, of [7]

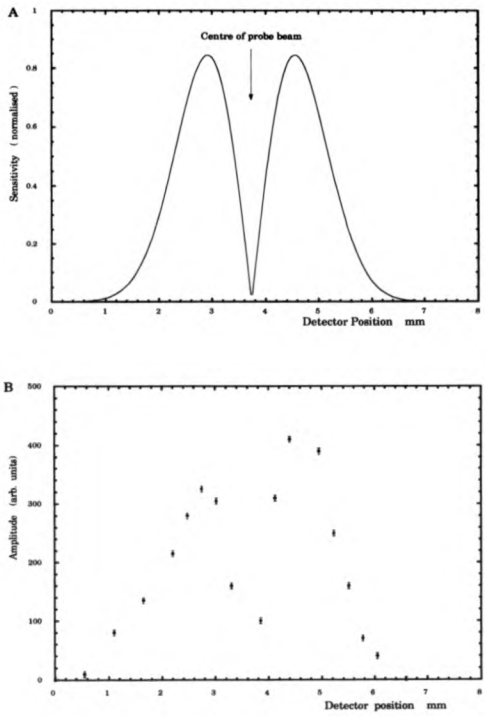

Fig 8.3 a , b Theoretical and experimental sensitivities for the single element detector with a 1mm diameter photodiode .

$$\frac{i_{sig}}{i_n} = I_{sig}\sqrt{\frac{\eta}{2BhvI_o}} \qquad 8.7$$

where B is the detector bandwidth , η the quantum efficiency and ν the frequency of incident light . This gives upon substitution and rearrangement the minimum detectable displacement U_{min} , where $U=\lambda\theta/2\pi$, λ being the acoustic wavelength , giving

$$U_{min} = \frac{\lambda a^2}{8Rx\pi}\left(\frac{2Bh\nu}{\eta I_o}\right)^{1/2} \qquad 8.8$$

For a 40MHz bandwidth detector and taking I_o~0.2mW (approximately one fifth of the beam power) , η=0.6 and $l=3\cdot10^{-4}$m gives a minimum detectable displacement of ~1pm , approximately an order of magnitude improvement on the traditional knife edge design .This enhancement is predominantly due to the fact that the detector samples a relatively small portion of the probe beam , leading to a large reduction in the background shot noise current compared with the traditional design where the photodetector samples upwards of a half of the probe beam radiation . The minimum detectable displacement is directly proportional to the acoustic wavelength , thus as the ultrasonic frequency is increased the surface tilt and hence the probe deflection is increased therefore reducing the minimum detectable displacement .

8.2.3 Design Two .

The second design of laser probe detector replaces the single element photodiode with a quadrant photodiode , type RS 652-027. For simplicity the elements were joined to form just two separate active areas . However the four elements used in a more complex configuration would provide the ability to sense motion in any direction which is not the case for single and double element detectors . The quadrant photodiode is placed symmetrically about the peak of the reflected beam , as shown in Fig 8.2b . Due to the size of the total

active diameter , (3mm) , the center of each element is close to one Gaussian radius of the laser beam and as will be shown yields a high sensitivity .

A fluctuation in the beam position , in the plane perpendicular to the separation direction of the two active regions , will produce increased light intensity on one half of the split photodiode while the other half of the detector will see a comparable decrease in light intensity . Fig 8.4 a&b shows the output of the individual elements produced by the passage of a Lamb wave across a thin plate , the two waveforms being π out of phase as expected . Inverting the output of one half of the photodiode and adding the two produces a signal of twice the amplitude and gives a signal to noise enhancement of 1.4 , shown in Fig 8.4c. .Thus the outputs from each half of the photodiode are fed into the inverting and non-inverting inputs of a high speed differential amplifier , of sufficient bandwidth to retain the signal frequency , to produce the overall output signal . D.C measurements of the individual photodiode outputs allow the detector to be correctly positioned at the centre of the reflected laser beam , hence improving the overall signal .

As before a measure of the light intensity variations observed on each half of the detector can be calculated . For good quality surfaces the reflected light may fall directly onto the double detector , while on poorer surfaces a focusing lens may be used to increase the signal to noise ratio . An analysis for this detector type similar to that carried out for design one gives the sensitivity of the device and the linearity of the signal output . If the photodiodes are initially balanced , having equal amounts of light falling on each , the output , Isig , is zero . The deflection of the beam by an amount , Ro , due to the acoustic surface perturbation causes different light intensity to fall onto each photodiode , giving the signal $I_{sig} = I_1 - I_2$ where I_1 and I_2 are the two detector outputs given as

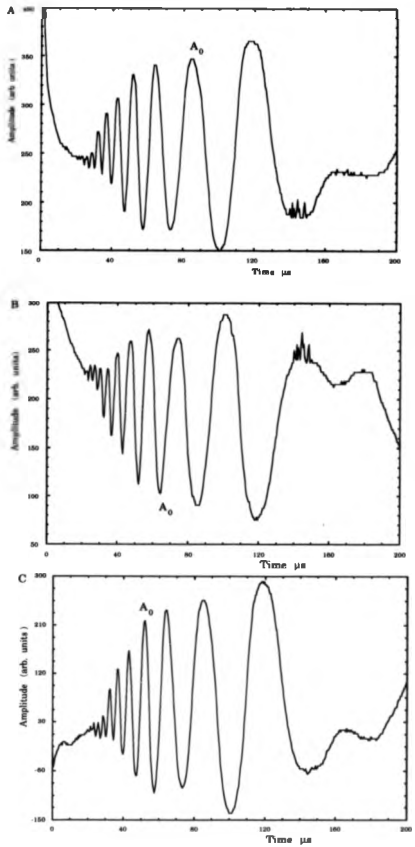

Fig 8.4 a , b & c : a & b show the output signals from the individual detector elements and c , the subtraction of the two signals

$$I_1 = \frac{X}{\alpha^2\pi}\int_0^{\pi}\int_d^{\infty} \exp\left(-\frac{(r-Ro)^2}{\alpha^2}\right)(r-Ro)\, dr\, d\theta \qquad 8.9a$$

and similarly

$$I_2 = \frac{X}{\alpha^2\pi}\int_0^{\pi}\int_{-d}^{-\infty} \exp\left(-\frac{(r+Ro)^2}{\alpha^2}\right)(r+Ro)\, dr\, d\theta \qquad 8.9b$$

where d is the half separation of the two detector elements , r the radial position within the Gaussian beam profile and X the laser power . Integrating and expanding the exponentials gives the output signal as

$$I_{sig} = \frac{X}{2}\exp\left(-\frac{(d^2+R_o^2)}{\alpha^2}\right)\sinh\left(\frac{2dRo}{\alpha^2}\right) \qquad 8.10$$

where the Gaussian radius may be determined as for design one using the relevant optical matrices . Fig 8.5a shows Isig as a function of reflected probe beam deflection amplitude , Ro , for two values of the Gaussian radius . The graphs show the pay-off between output signal amplitude against the region of linear behavior . Fig 8.5b shows the effect of increasing the photodiode separation , which enhances the region of linear response as the two detectors sample light more predominantly in the wings of the Gaussian beam . Therefore the detector may be tailored to the individual characteristics of the specific case under inspection . The small displacement calibration , equivalent to eq8.4 for the single detector design , may be given as

$$\theta = \frac{(1.22)^2 r\lambda_p^2}{2dD^2}\,\frac{I_{sig}}{I_o} \qquad 8.11$$

where $I_o = X\exp(-d^2/\alpha^2)$, an expression which is again different from Monchalin's solution and that derived for the previous design showing the requirement to characterize individual designs if any attempt at calibration is to be made . The signal to noise of this device , obtained using the same procedure as for case one , gave a minimum detectable displacement of ~1pm

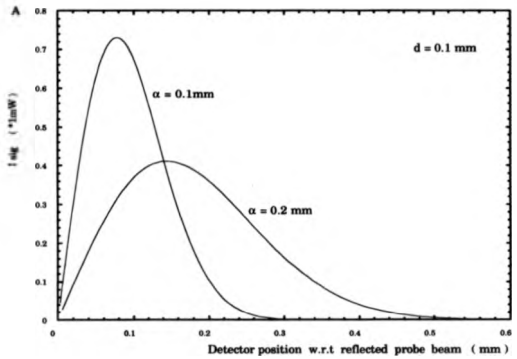

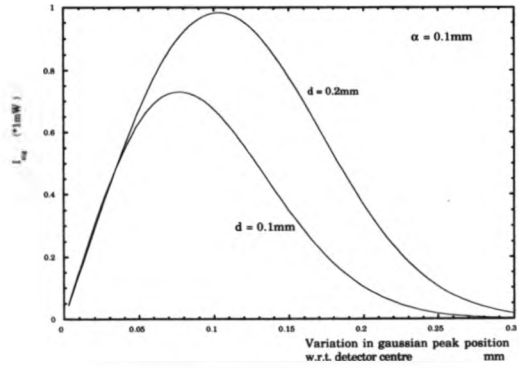

Fig 8.5 a & b Variation in detector output with respect to Gaussian beam radius and detector element separation respectively .

for a similar wavelength ultrasonic wave . Further amplification will introduce noise into the overall device thus increasing the minimum detectable signal .

8.3 Measurement of Surface and Bulk Ultrasonic Waves

As the use of knife edge detectors has been well documented for the detection of Lamb waves [2] this will not be discussed separately in this section , but will be dealt with in the context of thickness measurements of thin , transparent , polymer films . The inspection of surface and bulk waves employing both Nd:YAG and CO_2 laser generation on metals is used to characterise further the sensitivity , resolution and bandwidth of the devices .

8.3.1 Rayleigh Wave Measurements.

A focused , 200mJ Nd:YAG laser line source of length ~10mm was used to generate large amplitude Rayleigh waves . The use of a line source enhanced the wave amplitude , in the direction of the detector by at least an order of magnitude over that produced by a point source [8] . As the spectral range of the detector encompasses 1.06μm , the firing of the laser causes the photodiode to initially saturate , as it receivers scattered light from the sample and hence loses sensitivity for some time , up to ~2μs , determined by the photodiodes construction . To avoid this the Nd:YAG laser light is shielded from the detector to minimize this saturation . To reduce the effect of bulk transients on the ultrasonic waveform , which might perturb the Rayleigh arrival's structure , the back wall of the sample had grooves machined in it at intervals of ~5mm spacing , to randomly scatter longitudinal and shear waves . The sample had a slot of 2.5 mm depth machined across its length to act as a partial reflector of the Rayleigh waves . The interaction of the Rayleigh wave with the slot will produce a double pulse due to a mode converted shear -

Rayleigh wave originating from the tip of the slot [9] , the ability to detect the presence of this small feature giving a good test of the resolution and sensitivity of the detector .

Fig 8.6 a,b,c shows single shot measurements of surface waves recorded with the single and double element detectors and an out-of-plane sensitive EMAT as a comparative method of detection . Firstly one notes the lack of bulk waves detected by both knife edge devices . Despite the modulations in the back wall of the sample the EMAT has still detected bulk waves , which are however much reduced in amplitude to those detected on a parallel sided sample . This lack of bulk waves indicates either a lack of sensitivity or resolution of the knife edge device or the planar nature of the ultrasonic wave leading to reduced surface tilt . A comparison of peak to peak amplitudes of surface to bulk waves suggests that they have sufficient amplitude to be distinguished from the noise level , thus indicating a fundamental lack of detector resolution . The detection of the mode converted shear to Rayleigh wave , being of low amplitude with respect to the reflected Rayleigh wave is beyond the detection capability of the knife edge detectors .

Inspection of the successive EMAT detected Rayleigh waves shows them to be in phase with each other , which is not the case for the laser probe detected waves . Interferometric studies of Rayleigh waves reflected from 90° corners and from slots of various depths , which act essentially as partially reflecting corners , shows no phase change of the Rayleigh waves on reflection and the effect is therefore a feature of the wave - beam interaction .

Time-of-flight measurements on the Rayleigh waves indicates the history of successive arrivals . R1 corresponds to a direct wave having no interaction with a corner or slot , R2 corresponds to the partial reflection from the slot and thirdly R3 from a wave reflected off the corner of the sample . Subsequent arrivals are simply multiples of R2 and R3 . A wave travelling left to right will be the mirror image of a wave travelling right to left . Thus the surface

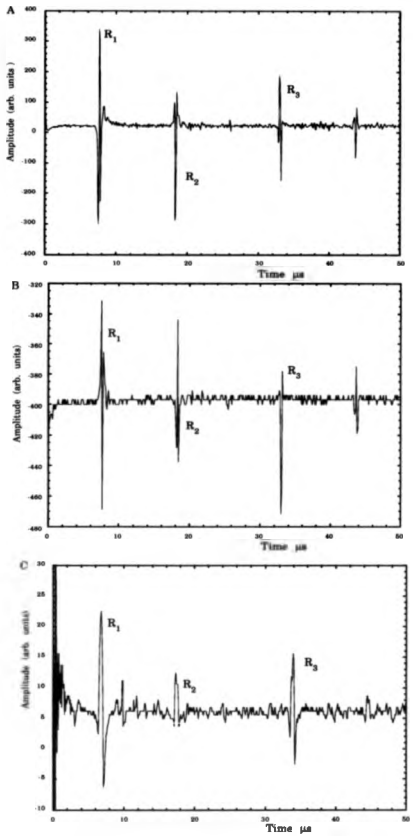

Fig 8.6 Rayleigh waves measured by :-
A: Single Element detector
B: Double Element detector
C: Longtudinal sensitive EMAT

gradient at any point on the wave will be opposite for the two cases , consequently the direction of probe beam deflections is similarly reversed . The relative directions of R1 and R3 as opposed to R2 are reversed which leads to the phase change of π between them . This gives a useful piece of additional information in that the relative directions of one waveform with respect to another may help determine their origin when a less obvious geometry is examined .

To determine the detectors resolution limits high resolution measurements of the Rayleigh waves were taken using the above three detectors . Figs 8.7 b,c show results for the single photodiode and EMAT detectors respectfully . The ultrasonic pulse shape of the optical detectors is similar to the shape of the waveform recorded using the EMAT . As has been previously discussed the EMAT is a velocity sensor , while the optical detectors are sensitive to surface angle . The impulsive , normal source generates a surface wave being the first time differential of Pekeris's solution , given in Fig 4.2 , which will be differentiated again by the action of the EMAT . The knife edge detectors will differentiate this wave with respect to position as it moves across the probe beam , thus the two outputs are equivalent , the theoretical prediction being shown in Fig 8.7a .

Comparison of the pulse widths and risetimes gives information on the bandwidth of the various detection systems and their effective detection widths . The EMAT with a coil width of 1mm , which also has some field broadening which enlarges the effective detection width [10] , gives a Rayleigh wave pulse width of 760 ns , measured from the two positive waveform peaks . The single photodiode detector gave a corresponding peak separation of 136 ns . The ultimate frequency content of the Rayleigh wave will be determined by the sources temporal and spatial extents and the detector width .The detected waveform is then the convolution of these three limiting responses with the impulse response .Since the ultrasound was generated by a 10ns risetime

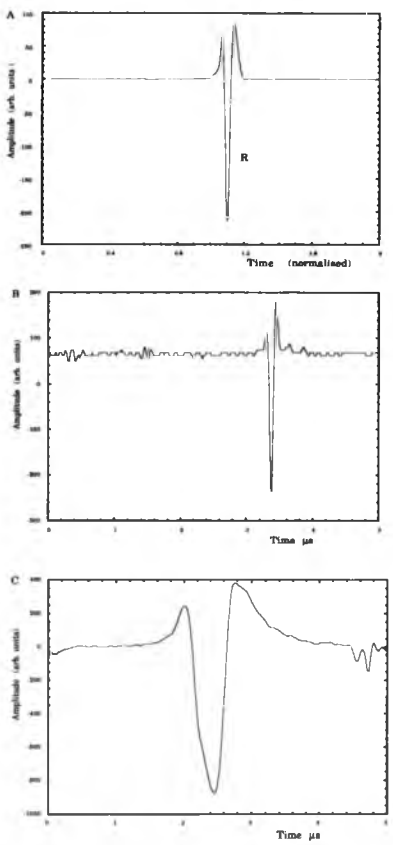

Fig 8.7 a,b,c
A: Theory based on Pekeris's model
B: Detected by single element detector
C: Longitudinal sensetive EMAT detected

laser with a source width of ~0.1mm the broadening of the pulse detected by the EMAT is predominantly caused by the finite coil width , while that detected by the optical detector is limited by the widths of both the source and receiver , as the focusing optics for the Nd:YAG laser and the HeNe probe laser are very similar . The temporal width of the optically detected Rayleigh wave suggests that the convolved detector and source widths gives an overall width of ~0.4mm and hence the laser probe detection width as ~0.2mm . The Rayleigh wave risetime recorded optically was 40ns giving a detector bandwidth of 8 MHz , a figure once more lowered by the spatial and temporal extent of source and receiver .

8.3.2 Bulk Wave Measurements

The ability to detect bulk transients indicates a much greater test for the knife edge detector . As considered previously the duration of the ultrasonic pulse is governed by the spatial and temporal parameters of the source and receiver . The width of the ultrasonic waveform , due to the temporal extent of the laser pulse will remain unchanged by the geometry of source and receiver provided the source type remains unchanged . The spatial extent of the source Δs , and receiver Δr , have a varying effect on the pulse duration dependent on the source - receiver separation and the angle ,θ , by which the two are offset. Considering a simple ray model approach the time delay , Δt , between the first and last arrivals is given as :-

$$\Delta t = \frac{(\Delta s + \Delta r)\sin(\theta)}{v} \qquad 8.12$$

where v is the relevant ultrasonic velocity . For angles greater than 45° $\Delta t \sim (\Delta s + \Delta r)/v$, while as the angle decreases towards zero the time separation tends to zero , leaving only temporal effects . Therefore the apparent frequency content for an on epicentre longitudinal wave is at least a factor of two greater

than that of a surface wave , using the source and receiver dimensions discussed above .

Both plasma and modified surface ultrasonic sources were used to generate acoustic transients in 10 mm thick samples of aluminium , stainless steel and copper . Measurements were taken at intervals of 2.5mm , from epicentre to 12.5 mm off - epicentre corresponding to $\theta \sim 50^{o}$, an angle greater than the critical angle , such that the Head wave will be resolvable from the shear wave . Fig 8.8 shows optically detected waveforms for angles of 26^{o} , 45^{o} and 51^{o} off-epicentre , recorded under the action of a surface modified Nd:YAG laser source . All three waveforms show large signal to noise ratios with the longitudinal , P, and shear ,S , arrivals being clearly defined . These waveforms may be compared to the differential of the outward displacing bulk waves calculated using Bresse's model as shown in Fig 8.9 , giving the corresponding theoretical waves to those in Fig 8.8 , convolved with a source function having a 30ns risetime . The form of the corresponding waves agrees closely with one another . The longitudinal arrivals are predominantly monopolar with a small negative component , while the shear waves are bipolar . The splitting of the Head wave in the 51^{o} waveform is observed and compares favourably to the theoretical predictions having the correct form , relative amplitude and polarity . No measurable on-epicentre signal was obtained as the ultrasonic arrival produces no surface tilting only outward displacement . Results obtained by the split photodetector showed the device to have a reduced sensitivity by a factor of approximately three , while however maintaining the same wave structure and frequency content as recorded by the single element device .

The graph shown in Fig 6.18 gives the peak to peak amplitude of longitudinal ultrasonic arrivals recorded on the 10 mm thick Al sample for positions on and off epicenter using an out of plane sensitive EMAT with fixed amplification . Results for both Nd:YAG and CO_2 laser sources with and

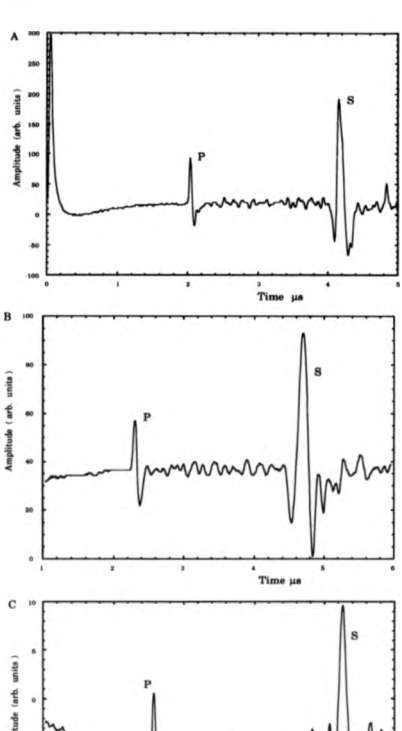

Fig 8.8 a , b & c Single element device waveforms , generated using a Nd:YAG laser , detected at angles of 26° , 45° & 51° degrees off-epicentre .

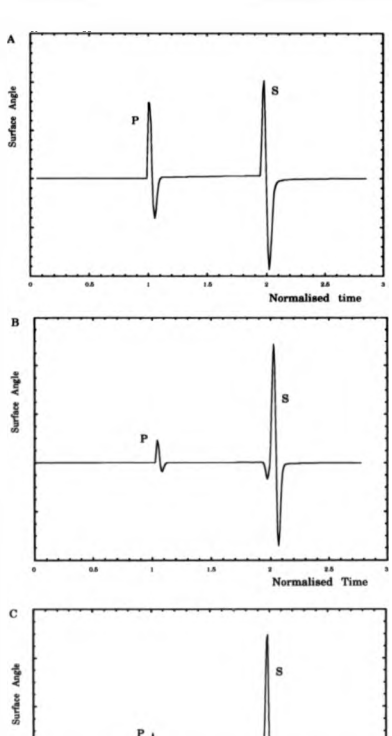

Fig 8.9 a , b & c Theoretical surface angle waveforms , calculated using Bresse's wide source analysis , for 26° , 45 °and 51° off-epicentre

without surface modification are presented , showing the large variation in acoustic amplitude produced for the four types of source . No corresponding enhancement of the detected signal amplitude is observed optically , with the measured amplitudes being lower or comparable to those generated with the 30mJ , Nd:YAG laser . Fig 8.10 gives the corresponding CO_2 generated waveforms to those presented in Fig 8.8 . The structure of which again agree with the theoretical waveforms shown in Fig 8.9 although the Head wave arrival on the 51° waveform is unresolvable from the shear wave , due to the large spatial extent and longer risetime of this laser source .

The loss of signal amplitude may be due to the wider ultrasonic source (3 - 4 mm) produced by the CO_2 laser as compared to that generated by Nd:YAG laser . The wider source will produce a wavefront which will tend towards a planar wave as the source size increases , resulting in a reduction in the surface angular tilt . To examine further the effects of source size a pulsed , 5MHz , PZT transducer of radius 7.5 mm was used to produce ultrasonic transients , generating an approximately planar ultrasonic wavefront within the 10mm thick sample used in this study . The amplitude of the ultrasonic pulse , measured using an EMAT gave an on-epicentre longitudinal amplitude comparable to that of the modified Nd:YAG source . The knife edge detector was unable to detect any ultrasonic signal over a range of positions off-epicentre , despite averaging to enhance the signal to noise by an order of magnitude . The parallel sided sample was replaced by a wedge shaped sample , such that the planar wavefront produced by the PZT probe impinged on the detection surface at an angle and hence producing a surface angular tilt . Under these conditions the knife edge detector was able to detect the ultrasonic signal .The ability to detect this signal for non-parallel generation and detection surfaces adds weight to the suggestion that the reduced ultrasonic amplitude obtained using CO_2 generation is due to the more uniform wavefront leading to reduced angular tilt at the surface .

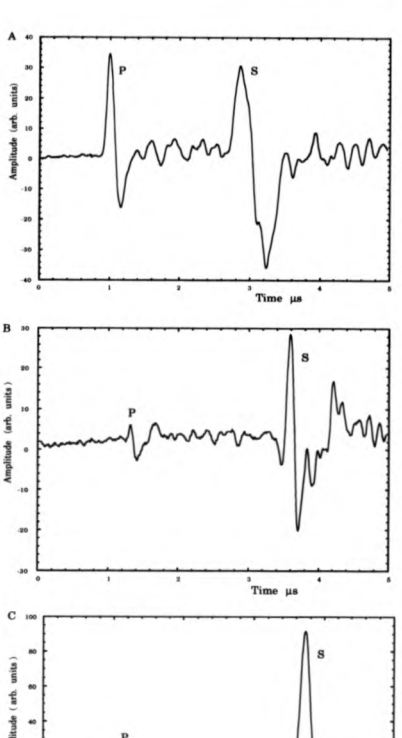

Fig 8.10 a , b & c Single element detector waveforms , generated with the CO_2 laser , detected at 26° , 45° and 51°off-epicentre .

The bulk waves signals recorded by both detectors under the action of the two generating lasers show repeatable features or oscillations which begin after the arrival of the initial longitudinal wave , as seen in Figs 8.8 & 8.10 . The pre-longitudinal signal shows the true noise level of the detection system . The post-longitudinal signals were found to be sample position sensitive , such that probing different bulk regions revealed a distinct change in the form of the oscillations although their frequency and amplitude remained approximately constant . These fluctuations are not due to intensity fluctuations in the reflected probe beam structure , as a fine resolution scan of the beam revealed no major fluctuations in the Gaussian beam profile . Even if such intensity variations existed the large amplitude longitudinal and shear arrivals would be most severely distorted and zero surface deflection would lead to zero beam displacement and hence no signal . This is seen not to be the case .

The use of a variety of materials , including copper which is a strong scatterer of ultrasound , showed no variation in the relative wave-arrival amplitudes to the amplitude of the oscillations . In conclusion the exact nature of these features is unknown although their origin must be ultrasonic and not optical and the most likely source being that of microstructural scattering [11] which due to its random nature arrives at the sample surface with random phase and causes localised surface tilting .

8.4 Thickness Measurements of Thin Polymer Films

This section examines the combination of laser probe detection and CO_2 generation in non-metals as employed to measure the thickness of thin polymer films and produce the basis on which the non-destructive testing of such films may be undertaken .

Fig 8.4 shows the typical Lamb wave structure which is comprised of a highly dispersive antisymmetric flexural wave , (Ao) . The faster symmetric

longitudinal wave is not detected by the laser probe detector as its motion is predominantly in-plane . Lamb waves are generated in materials who's thickness is small in comparison with the ultrasonic wavelengths propagating within them and thus for a typical laser pulse risetime of 10ns materials of thickness below ~100μm will support such waves . McKie [12] studied such waves generated in metallic foils , using a modified Michelson interferometer and employed a technique of spectral analysis of the waves to determine the plate thickness . EMATs have been used to measure Lamb waves in metallic plates , their ability to detect in-plane motion enabling the detection of the symmetric wave , a feature which is essential for the accurate determination of the plate thickness . Both interferometric and EMAT measurements fail to give an adequate measure of Lamb waves on transparent , non-metallic media . To facilitate the detection of such waves the geometry of the laser probe detector is used in a transmission manner rather than the normal reflection mode . The mechanism on which beam deflection occurs , originates from both the flexing of the film and the acousto-optic interaction .

8.4.1 Motion in Lamb Waves

As stated above , the antisymmetric wave is an out-of-plane motion while the symmetric wave is a predominantly in-plane longitudinal wave . Victorov [13] obtained solutions for a single frequency , time varying source , in terms of the in and out-of-plane motion of the symmetric and antisymmetric waves . The ratio , R_s , of the in to out-of-plane motion within the symmetric motion at the surface of the plate is given by

$$R_s = \frac{1}{d\sqrt{K_{so}^2 - K_l^2}} \qquad 8.14$$

where K_{so} is the wavenumber of the symmetric wave and K_l is the longitudinal wavenumber given by

$$K_l = \omega\sqrt{\frac{\rho}{(\lambda+2\mu)}} \qquad 8.15$$

Similarly the ratio of the antisymmetric wave , R_A ,of the in and out of plane motion is simply given at the film surface as

$$R_A = dK_A \qquad 8.16$$

where K_A is the antisymmetric wavenumber . Typical values for the symmetric and antisymmetric wavenumbers obtained from waveforms recorded on polymer materials , give $R_s \sim 10^3$ and $R_A \sim 10^{-2}$,thus there is a very large distinction between the in and out of plane motion associated with the two waves . It is important in the analysis of the waveforms obtained that there is almost no mixing in the origins of the signals for the two waves , in that the antisymmetric wave produces beam deflection via surface flexing while the acousto-optic interaction is responsible for the beam deflection associated with the symmetric waves .

8.4.2 Acousto-optic Interaction

An acoustic wave will produce a spatial variation in the density of a crystalline or homogenious material , these variations producing perturbations in the refractive index of the material . The elasto-optical interaction is characterised by the relation

$$\Delta\left(\frac{1}{n^2}\right)_{ij} = \sum_{k,l} P_{ijkl}\, e_{kl} \qquad 8.17$$

where e_{kl} is the Cartesian strain component , $(1/n^2)_{ij}$ is the coefficient of the optical index ellipsoid and P_{ijkl} the elasto-optic constant . For an isotropic

material , such as those studied in this work the subscripts describing the crystallographic directions may be dropped .

The interaction of a light field with a spatially varying refractive index may fall into two main categories . Firstly if the light field width is large compared to the acoustic wavelength , the index variations act as a diffraction grating [14] , producing transmitted light separated into distinct orders . Secondly for the light field width small in comparison with the acoustic wavelength the index variations act as a gradient deflector [15] . This type of probe therefore falls into the second class with the transient ultrasonic wave serving as a time varying refractive index gradient .

The effect of such a gradient on the path of a light beam may be determined geometrically , as carried out by Beiser [16] . Consider a light field wavefront passing perpendicularly through a refractive index gradient , as shown in Fig 8.11 . The beam at point P_1 sees a refractive index of n , while that at P_2 sees an index of $n+\delta n$. Thus in a time , t , the two points will travel distances D_1 and D_2 respectively where

$$D_1 = \frac{ct}{n} \quad \& \quad D_2 = \frac{ct}{n+\delta n} \qquad 8.18a\&b$$

The differing distances travelled rotate the wavefront through an angle , α , given by $\alpha=(D_1-D_2)/\delta x$, which for a material thickness , d , gives the beam deflection angle as

$$\alpha = \frac{d}{n}\frac{dn}{dx} \qquad 8.19$$

This relationship gives the possibility of determining the elasto-optic properties of the material . It also indicates that the angle of deflection is directly proportional to the gradient of the refractive index , which from eq. 8.17 is directly proportional to the spatial derivative of the stress field . An upper limit to the allowable deflection angle occurs because the beam is bent into regions of

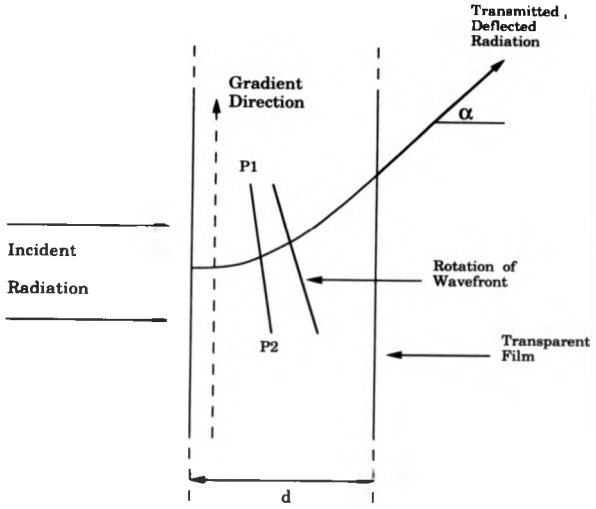

Fig 8.11 The rotation of an incident radiation wavefront under action of a refractive index gradient .

decreasing gradient and is subsequently bent back towards the the high index region . This effect may only perturb the detection of very high frequency waves and was not observed in the course of this work . The deflection of the beam is only sensitive to stress fields in the direction perpendicular to the direction of the light propagation . Therefore in the inspection of Lamb waves the acousto-optic interaction will only be sensitive to the in-plane motion of the symmetrical waves and the out-of-plane motion is not be sensed in this way , rather by the deflection of the film .

8.4.3 Experimental Arrangement

The experimental arrangement used in this study is shown in Fig 8.12 . The CO_2 laser , used with the reduced nitrogen gas mix to avoid any material damage , is focused to a line source via a 30cm focal length cylindrical lens . The degree of radiation absorption by the film may be measured with the photon drag detector , with typical absorptions upwards of 20% being measured on the films studied , a figure sufficient to generate a thermoelastic source .

The traditional geometry of the laser probe detector was changed to become linear [17] . This arrangement offers the advantage that ~86% of the available beam energy is used in probing the sample . The output of the photodiode is amplified by a wideband 60dB gain amplifier and captured in the usual manner . To obtain the highest resolution acousto-optic interaction the probe beam was placed perpendicularly to the film to ensure the minimum area of interaction , although the thin nature of the films means that this requirement may be relaxed without significant loss of signal resolution . The thickness determination was carried out in the manner outlined by McKie [10].

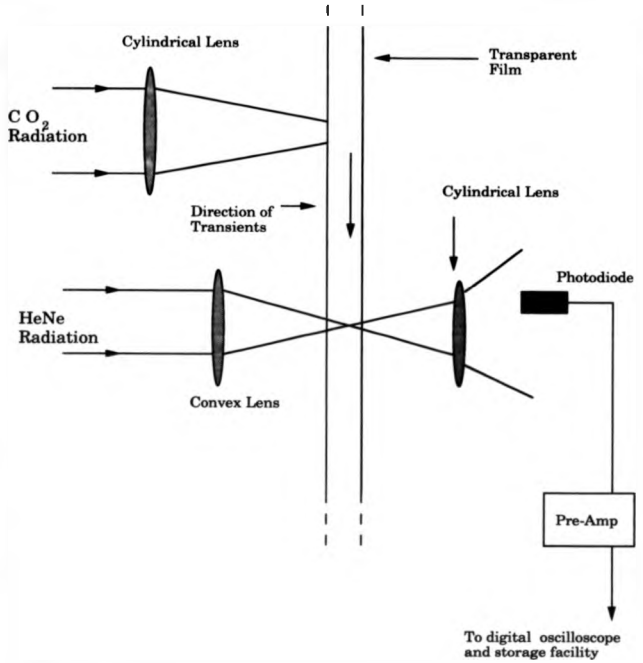

Fig 8.12 Experimental arrangement used in the generation and detection of Lamb waves on transparent , thin films .

8.4.4 Results & Discussion

Melinex films , [18] , ranging in thickness from 125μm down to 15μm were examined in this manner , the waveform detected on the 125 μm film (Fig 8.13) , clearly shows the zeroth order symmetric , S_0 , and antisymmetric , A_0 , arrivals . Fig 8.14 a&b show the corresponding waveforms recorded on 50μm and 15 μm sheets , again showing the S_0 and A_0 arrivals . However the structure of the antisymmetric wave is modified , having an amplitude envelope which does not increase continuously with time , but shows significant amplitude variations . Neglecting this effect and calculating the thickness in the usual manner yields the results presented in table 8.1 , which also shows the results recorded by McKie . McKie's results show agreement between the mechanically measured thickness and the Lamb wave results to become closer as the film thickness decreases . This trend is not observed for the results of the polymer films where in fact the deviation increases with decreasing thickness .

This effect may be analysed in terms of the thermoelastic source produced by the focused CO_2 radiation . Using the analysis for the wide thermoelastic source , presented in chapter 6 , the near top-hat beam profile will give rise to two source contributions separated by the width of the beam , the detected wave being the superposition of these two sources . Fig 8.15a shows an approximate solution to an impulsive line source based on the analysis given by Achenbach [5.1] , showing the highly dispersive nature of the antisymmetric wave , with the amplitude envelope growing steadily in time [19] . Fig 8.15b shows the resultant theoretical waveform produced by a 2.0mm radius source . The waveform shows many of the features observed in the experimental waveforms of Fig 8.14 , such as the non-uniform amplitude increase and the "beating" type effect resulting from the addition of the two dispersive waves . This work has recently been supported by a study undertaken by J.B. Spicer [20] who modelled a Gaussian beam profile , using an integral transform

Metals :-

Measured Thickness	Lamb Wave Technique
425.	300
102	89.5
80	72
49	44
27	26.5

Non - Metals :-

Measured Thickness	Lamb Wave Technique
123±0.5	121.5 ± 0.5
108±0.5	96 ± 5
50±0.5	63 ± 4
15±0.5	20 ± 3

Table 8.1 Comparison of thickness measurements using micrometer and Lamb wave techniques on metal and non-metal foils . [Metal results after McKie]

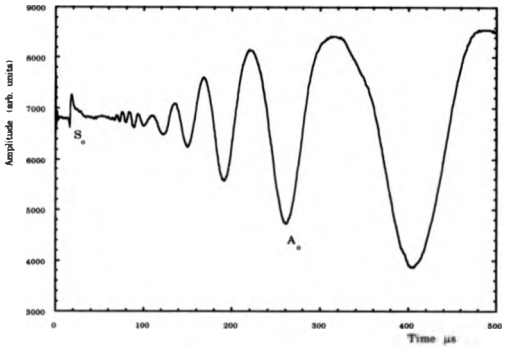

Fig 8.13 Lamb wave recorded on a 125 μm thick transparent film , showing both the symmetric and anti-symmetric waves .

approach and showed that the effect was to perturb the waveform in a slightly more subtle fashion , leading to only slight visible waveform alterations , but resulting in an incorrect thickness value being obtained .

The results obtained using this method may therefore be improved upon by decreasing the source width . An attempt in aperturing the radiation failed to generate waves of sufficient amplitude for detection , a more suitable method being to use a more powerful lens to reduce the beam dimensions .

8.5 Conclusion

This work shows the knife edge detector to be a highly sensitive means of detecting both surface and bulk waves . Theoretically it should be able to detect displacements of a few picometers and the bandwidth of the device ranges up to ~20MHz . The knife edge detector , being a surface angular tilt sensor is highly sensitive to the ultrasonic wavefront curvature resulting in its inability to detect large amplitude planar surface displacements such as generated with a PZT transducer . The calibration of the device shows that new designs must be treated individually if any attempt is to be made at absolute surface displacement measurement . When working with broadband transients such calibration is almost totally meaningless due to the strong wavelength dependency on the degree of beam deflection .

The study of Lamb waves in thin polymer films is a novel combination of generation and detection , providing a means of testing materials which could not previously be inspected remotely using ultrasound . The wide thermoelastic source effects on the detected Lamb waves give an extreme demonstration of the effects of finite source sizes complementing the previous work on bulk and surface waves .

The flexibility in design means that the knife edge probe may be easily modified to detect on complex geometries and provides the potential to form a

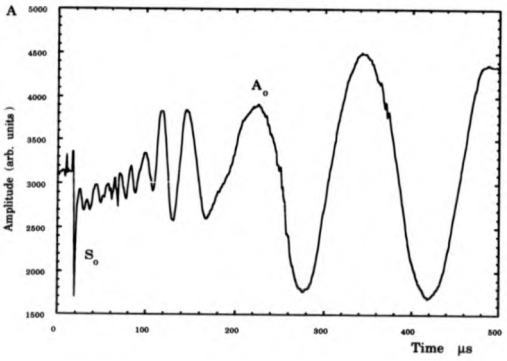

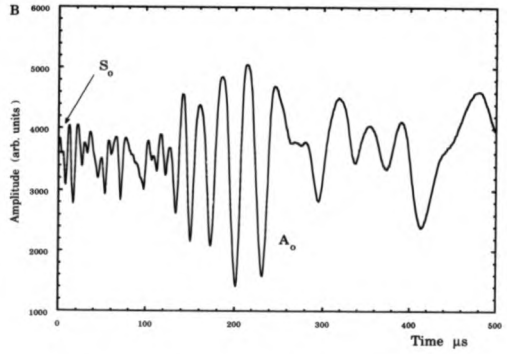

Fig 8.14 a & b Lamb waves recorded on 50um and 15μm thick films . The waves show the distortions produced by the wide thermoelastic source .

double probe device for the accurate determination of velocities . The obvious extension of the split photodiode to a quadrant device also gives the potential to measure the orthogonal components in an ultrasonic wave simultaneously from the relative output of the two sensors .

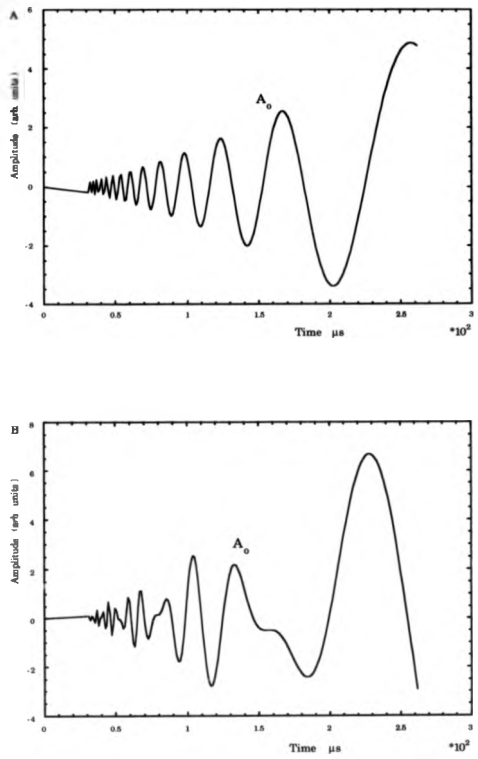

Fig 8.15 a Lamb wave calculation produced from a point source
b Lamb wave derived from the superposition of wave components from a 4mm wide source.

References Chapter 8

[1]A. Aindow , J. A. Cooper , R. J. Dewhurst & S. B. Palmer , J. Phys. E. Sci. Instrum. vol20 (1987)

[2]G.I. Stegeman , IEEE Trans SU-23 no1 pp33-61 (1976)

[3]H. Sontag & A.C. Tam , Appl. Phys. Lett. vol46 no8 (1985)

[4]J.P. Monchalin , IEEE Trans UFFC-33 no5 pp485-499 (1986)

[5]A. Yariv , "Introduction to Optoelectronics" (Holt , Rinehart & Wilson New York second edition , 1980)

[6]E. Hect & A. Zajac "Optics" (Addison Wesley Publishing , Amsterdam , sixth edition , 1980)

[7]J. Wilson & J.F.B. Hawkes , "Optoelectronics ; An introduction " (Prentice-Hall International series in Optoelectronics Ed P.J. Dean 1983)

[8]A.M.Aindow , R.J. Dewhurst & S.B. Palmer , Opt. Comm vol42 no116 (1982)

[9]J. A. Cooper , PhD Thesis , chapter 9 , Hull University

[10]C. Edwards & S.B. Palmer , Nondestr. Test. Eval vol 5 pp203-212 (1990)

[11]C. B. Scruby , R. J. Dewhurst , D. A. Hutchins & S. B. Palmer in "Research Techniques in NDT" (Edited by R.S.Sharpe , Academic Press , London) vol 15 p281 (1982)

[12]A.D.W. McKie , chapter 7 Ph.D Thesis University of Hull (1987)

[13]I.A. Victorov , "Rayleigh and Lamb Waves " (Plenum Press , New York 1967)

[14]R.W. Damon, W.T. Maloney & D.H. McMahon vol 7 chapter 5 of Physical Acoustics (Edited H.P. Mason & R.N. Thurston) Academic Press (1970)

[15]J. Kolb & A.P. Locker , J.A.S.A. vol26 pp249-251 (1954)

[16]L. Beiser , IEEE vol QE-3 no 11 pp560-567 (1967)

[17]M.W. Sigrist , J. Appl. Phys. vol60 no7 pp83-121 (1986)

[18] Melinex Films supplied by ICI

[19]C. Edwards , Private Communications

[20]J.B. Spicer , J.B. Deaton , A.D.W. McKie & W. Wagner in Proc. Review of Progress in Quantitative NDE (1990)

Chapter 9

Conclusion and Future Work

9.1 Conclusion

The work carried out in this thesis represents the characterisation of the CO_2 laser as a means of generating ultrasound in solids . As such , it's aims were to describe the thermoelastic and evaporative interactions which were previously known to generate ultrasound and more importantly to accurately model the gas plasma as a means of ultrasonic generation . The bulk of this work encompasses the properties of the various interaction processes such that direct comparison with traditional laser generation may be made .

Previous work involving the interaction of CO_2 laser , 10.6μm , radiation with solids has been characterised using high speed , streak photography to observe the plasma motion together with ballistic pendulums and pressure sensors to detect the impulses and peak pressures generated by the plasma . The interaction details offered by such techniques give a relatively low degree of information concerning the time history of the shock wave - sample interaction . Analysis of these observations and measurements have been carried out using spherical and cylindrical shock wave analysis which provided an order of magnitude agreement with experimental observations .

The work presented in chapter 4 aims to complement and extend the understanding of the interaction gleaned from previous reports . This chapter verifies that a prerequisite for gas breakdown is the presence of thermally uncoupled regions of target material from which thermal electrons may be generated . From interferometer and EMAT ultrasonic measurements , accurate determination of the delivered impulses and the required plasma breakdown thresholds have been made . The ability to record the time history of the ultrasonic pulse was shown to be of particular importance in the inspection of the pulse reflections observed within the plasma . No trace of such gas

dynamics is possible from the inspection of streak camera measurements or ballistic pendulums which will only detect the initial interaction characteristics . As an ultrasonic source , the CO_2 laser was shown to generate surface displacements of up to ~15nm within the Laser Plasmotron regime . This amplitude compares favourably with those the Nd:YAG laser produces , which with a focused , 200mJ laser pulse generates a displacement of ~10nm and in addition creates a significant damage pit .

The complex nature of the plasma development has been examined in terms of the source function generated in the two limiting plasma regimes of the Laser Plasmotron and the Laser Detonated Wave . Consideration of point , line , wide and expanding source types has shown the plasma to generate , within the limit of the available analysis and means of inspection , a static wide source ranging in diameter from 1 - 4 mm . The wide source analysis is complemented and extended by the inspection of the ultrasonic directivity patterns and the use of wide source models to calculate the energy distribution within the solid . The wide source directivity model is an extension of analyses derived using a top-hat , piston source profile and has been complemented by the mathematical extension to a non-uniform source function . This source function may be further extended to include a range of source profiles of varying width and form such that the middle ground between a Gaussian beam and top-hat source profiles may be filled .

The wide source analysis was continued in the study of the thermoelastic and evaporative source types . In terms of an efficient ultrasonic source the thermoelastic interaction is very weak , which coupled with it's wide source nature produces a rather structureless waveform of little use in terms of NDT . Conversely the evaporative source produces epicentral displacements of the order ~60nm , a factor of four increase over those generated by an efficient plasma source . However such a means of ultrasonic generation is rather impractical due to the limitations imposed by the application of an overlying

liquid who's depth must be critically controlled if repeatable amplitude measurements are to be made . Both the thermoelastic and evaporative sources provide an excellent means of investigating the effect of source widths , of up to 15mm , having either top-hat or Tukey profiles . The analysis of the waveforms gives excellent agreement with the theoretical models considered although deconvolution of the temporal and spatial profiles effects are difficult to perform accurately .

The continuing thread of non-point like source functions throughout this thesis is extended to encompass the effect of an optically penetrating thermoelastic source . The relatively simple , non-integral transform approach adopted in chapter 7 , has been shown to give pleasing agreement with experimentally observed waveforms . Unlike the point or wide source , the ultrasound produced from an optically penetrated material is shown to be dependent on the incident power density as demonstrated by the increased ultrasonic risetimes observed as a result of increased power density . The combination of the work encompassing ultrasonic generation in non-metals and the continued development and analysis of the laser probe detector offers a versatile means of inspecting an increased range of materials on which traditional non-contacting method of inspection may not be used .

9.2 Future Work

One of the main drawbacks of the laser used in this study is the low degree of flexibility offered in manipulation of the lasers temporal pulse profile . As opposed to a solid state laser the molecular laser pulse may be varied by means of the gas mixture , as discussed in chapter 4 and the gas flow rate through the laser . At present a systematic study into the effect of nitrogen content in the gas mixture is being undertaken , while keeping the front end pulse structure constant . The preliminary investigation into the effect of pulse

reflections within the plasma is therefore being extended in terms of the nitrogen tail duration which is the predominant factor in the creation of shock wave reflections within the plasma . The ultrasonic technique is ideally suited to the observation of such pulse reflections as the entire time history of the shock wave at the sample surface may be recorded giving an absolute measure of the interaction .

Variation of the laser gas mixture and flow rate may be used to shorten the front end pulse duration . At present the laser produces a 1J pulse with a 100ns F.W.H.M. duration . Increasing the carbon dioxide content at the expense of the nitrogen and carbon monoxide content coupled with a doubling of the gas flow rate will reduce the F.W.H.M. to ~40ns while maintaining the output energy [1] . The resulting enhanced power density will reduce the time required for a sufficient degree of thermionic emission to be produced , allowing a larger fraction of the laser energy to be used in the rapid creation of a gas plasma . The added benefits provided by the potential increase in generated ultrasonic frequency content may however be drastically offset by the rapid formation of a Laser Detonated Wave or even clean air breakdown ; both phenomena considerably reducing the ultrasonic generation efficiency . The advantage of increased power density may also be used to generate a more planar ultrasonic wave by the ability to generate a wider diameter plasma source .

A second possible technique which may increase the efficiency of the CO_2 laser source may be to pre-ionise the sample prior to irradiation and as such the energy lost in the inefficient target heating process is used efficiently in the creation of a plasma . This pre-ionisation may be created by an initial pulse of ultraviolet radiation to excite photoelectrons from within the sample or alternatively an electrode held at a high negative potential such that corona discharge occurs , may be placed close to the sample resulting in a sufficiently high electron density . The advantage of the first technique and possible

disadvantage of the second , is that the electrons generated are localised to the sample surface , an important point of consideration when preventing breakdown occuring away from the sample surface resulting in inefficient ultrasonic generation due to plasma shielding .

In the field of the laser probe detection the simplistic optical arrangement provides a sound basis on which dual or multiple beam inspection may be undertaken . This is an area of recent interest and has been shown as an accurate means of velocity and attenuation measurements [2,3] . Although the attenuation measurements derived from such a dual laser probe may be difficult to attain , with respect to the sensitivities of the devices , the velocity measurement may be accurately achieved within a single laser pulse , providing an excellent test for material properties such as anisotropy or even in the detection and sizing of bulk and surface defects .

References Chapter 9

[1]Lumonics Ltd Private Communications
[2]A.D.W. McKie , J.W. Wagner , J.B. Spencer & J.B. Deaton , presented at " Review of Progress in Quantitative NDE" , San Diego (1990)
[3]J. Huang & J.D. Achenbach , presented at " Review of Progress in Quantitative NDE" , San Diego (1990)

Publications arising from this work

C. Edwards , G. S. Taylor & S. B. Palmer , J. Phys. D vol 22 no 9 pp1266-1270 (1989)

G. S. Taylor , D. A. Hutchins , C. Edwards & S. B. Palmer vol 28 no 6 pp343-350 (1990)

G. Taylor , C. Edwards & S. B. Palmer , Nondestr. Test & Eval. vol5 no2 pp135-144 (1990)